

The complexity of Orion : an ALMA view^{*†}

I. Data and first results

L. Pagani¹, C. Favre^{2,3}, P. F. Goldsmith⁴, E. A. Bergin⁵, R. Snell⁶, and G. Melnick⁷

¹ LERMA & UMR8112 du CNRS, Observatoire de Paris, PSL Research University, CNRS, Sorbonne Universités, UPMC Univ. Paris 06, F- 75014 Paris, France

e-mail: laurent.pagani@obspm.fr

² Univ. Grenoble Alpes, CNRS, IPAG, F-38000 Grenoble, France

³ INAF-Osservatorio Astrofisico di Arcetri, Largo E. Fermi 5, I-50125, Florence, Italy

e-mail: cfavre@arcetri.astro.it

⁴ JPL, Pasadena, California, USA

e-mail: paul.f.goldsmith@jpl.nasa.gov

⁵ Department of Astronomy, University of Michigan, 311 West Hall, 1085 S. University Ave, Ann Arbor, MI 48109, USA

e-mail: ebergin@umich.edu

⁶ Department of Astronomy, University of Massachusetts, Amherst, MA, 01003, USA

e-mail: snell@astro.umass.edu

⁷ Harvard-Smithsonian Center for Astrophysics, Cambridge, Massachusetts, USA

e-mail: gmelnick@cfa.harvard.edu

Received 19/01/2017; accepted 22/05/2017

ABSTRACT

Aims. We wish to improve our understanding of the Orion central star formation region (Orion–KL) and disentangle its complexity.

Methods. We collected data with ALMA during cycle 2 in 16 GHz of total bandwidth spread between 215.1 and 252.0 GHz with a typical sensitivity of 5 mJy/beam (2.3 mJy/beam from 233.4 to 234.4 GHz) and a typical beam size of 1'7×1'0 (average position angle of 89°). We produced a continuum map and studied the emission lines in nine remarkable infrared spots in the region including the Hot Core and the Compact Ridge, plus the recently discovered Ethylene Glycol Peak.

Results. We present the data, and report the detection of several species not previously seen in Orion, including n- and i-propyl cyanide (C₃H₇CN), and the tentative detection of a number of other species including glycolaldehyde (CH₂(OH)CHO). The first detections of gGg' ethylene glycol (gGg' (CH₂OH)₂) and of acetic acid (CH₃COOH) in Orion are presented in a companion paper. We also report the possible detection of several vibrationally excited states of cyanoacetylene (HC₃N), and of its ¹³C isotopologues. We were not able to detect the ¹⁶O¹⁸O line predicted by our detection of O₂ with Herschel, due to blending with a nearby line of vibrationally excited ethyl cyanide. We do not confirm the tentative detection of hexatriynyl (C₆H) and cyanohexatriyne (HC₇N) reported previously, or of hydrogen peroxide (H₂O₂) emission.

We report a complex velocity structure only partially revealed before. Components as extreme as -7 and +19 km s⁻¹ are detected inside the hot region. Thanks to different opacities of various velocity components, in some cases we can position these components along the line of sight. We propose that the systematically redshifted and blueshifted wings of several species observed in the northern part of the region are linked to the explosion that occurred ~500 years ago. The compact ridge, noticeably farther south displays extremely narrow lines (~1 km s⁻¹) revealing a quiescent region that has not been affected by this explosion. This probably indicates that the compact ridge is either over 10,000 au in front of or behind the rest of the region.

Conclusions. Many lines remain unidentified, and only a detailed modeling of all known species, including vibrational states of isotopologues combined with the detailed spatial analysis offered by ALMA enriched with zero-spacing data, will allow new species to be detected.

Key words. ISM: abundances – ISM: clouds – ISM: structure – Astrochemistry – Molecular processes – ISM: individual objects : Orion

Send offprint requests to: L.Pagani

^{*}This paper makes use of the following ALMA data: ADS/JAO.ALMA#2013.1.00533.S. ALMA is a partnership of ESO (representing its member states), NSF (USA) and NINS (Japan), together with NRC (Canada), NSC and ASIAA (Taiwan), and KASI (Republic of Korea), in cooperation with the Republic of Chile. The Joint ALMA Observatory is operated by ESO, AUI/NRAO and NAOJ.

[†]The reduced ALMA data cubes as listed in Table 1 are available at the CDS via anonymous ftp to cdsarc.u-strasbg.fr (130.79.128.5) or via <http://cdsweb.u-strasbg.fr/cgi-bin/qcat?J/A+A/>

1. Introduction

The Orion region hosts two well-studied star forming sites, Orion A and Orion B. Orion A is subdivided into four clouds (Orion Molecular Cloud 1 – 4, OMC) and OMC1 holds the Kleinmann-Low Nebula (KL), often referred to as Orion–KL (but also numerous other names, as listed in SIMBAD¹). The Orion–KL nebula is the nearest massive star forming region (distance equal to 388 pc ± 5 pc, Kounkel et al. 2017, in replacement of the previous value of 414 pc ± 7 pc, Sandstrom et al. 2007;

¹<http://simbad.u-strasbg.fr/simbad/sim-id?Ident=Orion-KL>

Menten et al. 2007) and as such has attracted considerable attention and is the subject of thousands of publications. The core is complex with several remarkable sources, the Hot Core (HC), the Compact Ridge (CR), the Extended Ridge (ER), the Plateau, numerous methyl formate (MF) peaks (Favre et al. 2011), and other infrared/submillimeter peaks listed in many papers (e.g. Rieke et al. 1973; Robberto et al. 2005; Friedel & Weaver 2011), including three runaway objects: BN, I, and n (Gómez et al. 2005; Rodríguez et al. 2005, 2017). Among the studies aimed at identifying molecules in Orion, which is the reference source along with Sgr B2 in which to search for new species, many surveys have been conducted with single-dish telescopes from the ground (from some of the earliest works by Sutton et al. 1985; Blake et al. 1986 to recent observations with the IRAM-30m, Tercero et al. 2010, 2011; Cernicharo et al. 2016, etc. and with Herschel in a dedicated 1.2 THz bandwidth survey, Bergin et al. 2010; Crockett et al. 2014). With the sensitivity progress of the spectroradiometers, these surveys have reached the confusion limit ; almost all the recorded channels contain emission of some species, implying strong blending and difficulty determining the baseline level. The confusion limit is partly due to the impossibility for single-dish telescopes to spatially separate the contribution of the different sources in Orion that occur at different velocities, therefore increasing the overlap between lines. Naturally, interferometers have been used to separate the components, diminish the confusion, and help understand the ongoing evolution of the chemical and physical complex structure (e.g. Favre et al. 2011; Peng et al. 2012; Brouillet et al. 2013; Peng et al. 2015; Tercero et al. 2015; Peng et al. 2017).

After our detection of O_2 in Orion with Herschel (Goldsmith et al. 2011; Chen et al. 2014), and due to the difficulties of the interpretation, we decided to try to pinpoint the emission region by performing deep observations of the rarer $^{16}O^{18}O$ isotopologue with ALMA at 234 GHz. To increase the interest of these observations, we took advantage of the possibility to divide the run into five independent observing blocks to move the backend windows as much as possible to cover the maximum bandwidth. The choice of the window positions was a compromise between the technical limitations and the inclusion of species somewhat related to O_2 in their formation process, such as SO and NO, or those useful for diagnostic purposes of the source where O_2 would have been detected compared to the other sources of the region in order to understand the reason for a limited emission region.

In this paper, we present the data resulting from this survey and the first results we obtain. Further analysis, and in particular the first detection of acetic acid and of the gGg' conformer of ethylene glycol will be reported in a series of forthcoming papers (Favre et al. *subm.*, Pagani et al. *in prep.*). These are presently the most sensitive interferometer observations towards Orion-KL.

The paper is organized as follows. In Sect. 2, we present the observations and the data reduction. In Sect. 3, we present the data analysis (new species or new vibrationally excited transitions, refuted species from previous tentative detections, non-detected species), and in Sect. 4 we discuss the velocity components and present our considerations regarding the source structure. Conclusions are developed in Sect. 5.

2. Observations and data processing

The observations were performed on 29 December 2014 with 37 antennas for the first four scheduling blocks and on 30 December 2014 for the last block with 39 antennas. Two pointing directions were observed, the same as those used in the Herschel observa-

tions (Goldsmith et al. 2011; Chen et al. 2014), namely the KL region, RA_{J2000}: 05^h35^m14^s.160, Dec_{J2000}: -05°22'31".504 and the H_2 vibrational peak farther north, RA_{J2000}: 05^h35^m13^s.477, Dec_{J2000}: -05°22'08".50. In this paper, we only discuss the data from the first pointing (the Orion-KL region). The resolution was set to 488 kHz to get ~ 0.6 km s⁻¹ resolution to spectrally resolve the expected $^{16}O^{18}O$ linewidth of 1.5 – 2 km s⁻¹ (see Sect. 3.7.1). The resolution selection gives a bandwidth of 0.937 GHz per window. For each pointing, we split the observations into five observing blocks with different frequency setups, resulting in 16 different frequency bands (four windows per setup, one window always centered on $^{16}O^{18}O$ at 234 GHz, the other three moved around), covering approximately 16 GHz of total bandwidth between 215.15 and 252.04 GHz. The details of the frequency coverage are given in Table 1. Compared to the Cycle 0 Science Verification survey of Orion (SV0), we cover half of the SV0 frequency interval, but have coverage beyond the SV0 survey between 250 and 252 GHz, with the same frequency resolution, a slightly smaller beam (on average 1".7×1".0 compared to 2".×1".5, Tercero et al. 2015) and a much better sensitivity (SV0 sensitivity is in the range 10 – 30 mJy beam⁻¹, Hirota et al. 2012, compared to 2 – 8 mJy beam⁻¹ in the present study). The data were re-calibrated using the provided python script (script-forPI.py) in the Common Astronomy Software Applications (CASA) package V.4.2.2 (McMullin et al. 2007). The continuum was estimated in the UV tables and subtracted, velocity correction to LSR scale was performed, and the data (UV tables) were subsequently exported and converted to Gildas format for final processing (cleaning) using the MAPPING application². For each source, spectra were extracted in a CLASS² file, converted from Jy/beam to K (see Table 1) and corrected for primary beam coupling. The primary beam coupling runs from 99% for the source IRc7 to 71% for MF10. All velocities are expressed in the local standard of rest, (LSR).

3. Analysis

Because we currently lack the zero-spacing data to recover the extended emission of many species, we generally have not attempted to derive column densities and excitation temperatures of the species we discuss here. This will be done in a future work once these data are obtained and included in the data processing. However, we tried to fit the emission with the supposition of local thermodynamical equilibrium (LTE), for all species by adjusting their column density, excitation temperature, velocity and linewidth (except for methyl cyanide, CH₃CN, see Sect. 4.3). The fit was adjusted by eye to reasonably fit most of the lines of each species; this is considered a definitive determination of the line velocity and width, but not of the species column density and excitation temperature. This permits a determination of the number of velocity components necessary to fit the profiles. The LTE fit was performed using LINEDB and WEEDS sets of routines inside CLASS (Maret et al. 2011). The line catalogues are the Cologne Database for Molecular Spectroscopy (CDMS, Müller et al. 2001, 2005) and the Jet Propulsion Laboratory (JPL) catalogue (Pickett et al. 1998), with some complementary data provided by A. Belloche from the Belloche et al. (2013, hereafter B13) work to identify vibrationally excited states of vinyl and ethyl cyanides which we do not discuss in this paper but which were needed since a number of these transitions are very strong, up to 30 K.

²<http://www.iram.fr/IRAMFR/GILDAS/>

Table 1. Frequency bands and beam parameters.

Band (#)	Window (spw)	Block ^a (sg)	Frequency range ^b (MHz)		Beam shape (arcsec)	Pos. angle (degree)	Noise ^c (mJy/beam)	Conversion (K/Jy)	Noise ^c (mK)
1	3 ^d	1	215149.592	216086.673	1.8×1.1	86	7.0	13.3	93
2	2 ^d	1	216342.044	217279.136	1.8×1.1	84	3.7	13.1	48
3	3	2	217273.522	218210.619	2.2×1.0	102	3.6	11.7	42
4	2	2	218203.531	219140.628	2.2×1.0	102	4.6	11.6	53
5	3 ^d	3	219126.547	220063.614	1.9×1.0	95	4.5	13.3	60
6	2 ^d	3	219783.544	220720.641	1.8×1.0	95	5.1	14.0	71
7	1	1	229756.971	230694.089	1.4×0.8	80	4.0	20.6	82
8	1	2	230698.921	231636.062	2.1×0.9	102	3.9	12.1	47
9	1	5	232238.058	233175.172	1.6×1.0	80	3.5	14.1	49
10	0	1 – 5	233469.680	234421.910	1.6×0.8	90	2.3	17.5	40
11	1	3	235083.689	236020.787	1.7×0.9	95	5.1	14.4	73
12	1	4	236268.702	237205.799	1.6×0.9	87	3.8	15.2	58
13	3	5	244833.767	245770.865	1.6×0.9	79	4.6	14.1	65
14	2	5	245772.781	246709.895	1.6×0.9	79	4.6	14.0	64
15	2	4	250153.833	251090.932	1.5×0.9	88	8.0	14.4	115
16	3	4	251078.799	252015.916	1.3×0.8	86	8.4	18.6	156

Notes. ^(a) Observing block : all frequency windows with the same observing block number have been observed simultaneously ^(b) the frequency range is given for $V_{\text{LSR}} = 9 \text{ km s}^{-1}$. ^(c) Noise is not corrected for primary beam coupling and is therefore a lower limit to the actual noise in each source. Corrections run from 1% (IRc7) to 41% (MF10). ^(d) A last minute change of frequency introduced an error in setting the bands creating a hole from 216087 MHz to 216342 MHz and an overlap from 219784 to 220064 MHz. The reduced ALMA data cubes are available at the CDS via anonymous ftp to cdsarc.u-strasbg.fr (130.79.128.5) or via <http://cdsweb.u-strasbg.fr/cgi-bin/qcat?J/A+A/>

3.1. Continuum map

Owing to the density of lines, it is somewhat difficult to find enough channels free of emission to build a continuum map. We could find two reasonably clean frequency ranges in the 218 and 235 GHz bands (bands 4 and 11 resp.), each constituting a selection of channels across the 1 GHz bandpass, which gave similar results, confirming that the channels were not polluted by line emission. Figure 1 shows the resulting continuum emission map together with the positions of the ten sources we are studying in detail in this work along with the three runaway sources (BN, I, and n), and the methyl formate peak 6 (MF6). The continuum emission (at the HC position) has a peak value of $\sim 1.2 \text{ Jy/beam}$ after correcting for primary beam coupling, which corresponds to a brightness of $\sim 2.9 \times 10^4 \text{ MJy/sr}$.

3.2. Line emission

Several molecular components, that can be distinguished both spatially and spectroscopically, are associated with Orion–KL. The Hot Core, Compact Ridge, Extended Ridge and Plateau have been described in a number of papers (e.g. Mangum et al. 1990; Lerate et al. 2008; Friedel & Weaver 2011). A sketch illustrating the position of these components in the plane of sky is given by Irvine et al. (1987). In addition, interferometric studies of complex organic molecules have revealed the presence of other molecular clumps within Orion–KL (see e.g. Friedel & Snyder 2008; Favre et al. 2011; Favre et al. 2011; Friedel & Widicus Weaver 2012; Brouillet et al. 2013; Peng et al. 2013). Table 2 lists the main physical parameters of the molecular components. We have extracted spectra for ten sources labeled in Fig. 1, converted them to an antenna (main beam) temperature scale using the conversion factor listed in Table 1, corrected them for beam coupling by measuring the primary beam coupling at the source position (Fig. 1), and removed any residual continuum offset (typically 0.2 – 0.5 K, maximum 2 K). Hereafter, bands will be called by their number, for example band 1 for the 215150 to 216087 MHz band, which was spectral window #3 in

the first group of observations (= spw3/sg1, see Table 1). Nine sources are infrared compact sources and sometimes methyl formate (MF) sources (Favre et al. 2011). One source, not known as an infrared peak or a MF peak but situated between the MF2 and MF6 peaks has been named the Ethylene Glycol Peak (hereafter Et. Glycol in the figures or EGP in the text), following the discovery of a Gg’ ethylene glycol ($(\text{CH}_2\text{OH})_2$) in this location (Brouillet et al. 2015). We did not analyze MF6 because a quick inspection showed that apart from the SiO maser centered on source I and overlapping with HC, there is little difference in the main line shapes and ratios between MF6 and HC.

We have examined our data for the presence of over 130 candidate species (where a species corresponds to one entry in the JPL (Pickett et al. 1998) or CDMS (Müller et al. 2005) catalogues, which differentiate vibrationally excited states, isotopologues, isomers and conformers, representing ~ 60 different species and ~ 70 if we differentiate the isomers and conformers). Of the ~ 130 candidates, ~ 90 species are securely identified, 11 species are tentatively detected, and ~ 35 species already known in other sources are not detected (the list of species is presented in Table B.1). Two species, the dioxygen ^{18}O isotopologue ($^{16}\text{O}^{18}\text{O}$) and hydroxylamine (NH_2OH), have been actively searched for in the interstellar medium, but have still not been detected.

Figure 2 displays the ensemble of the collected spectra for all ten sources in band 1, while Fig. 3 displays the same data expanding the vertical axis to show emission below 5 K to highlight the weaker lines. All 16 bands are presented in Appendix A, Fig. A.1a – p, and Fig. A.2a – p. The same data plus the combination of the fits to individual species is subsequently displayed in the same appendix in order to give an idea of the unknown lines that remain (Figs. A.3a – p and A.4a – p). It is interesting to see that due to the absence of beam dilution for all sources, a large number of lines are stronger than 5 K, unlike in reported surveys from the 30 m and other single-dish telescopes (e.g. Tercero et al. 2010). Depending on the source, 13 to 29% of the channels are above 5 K, and this is only a lower limit since the intensity of lines that are produced by spatially

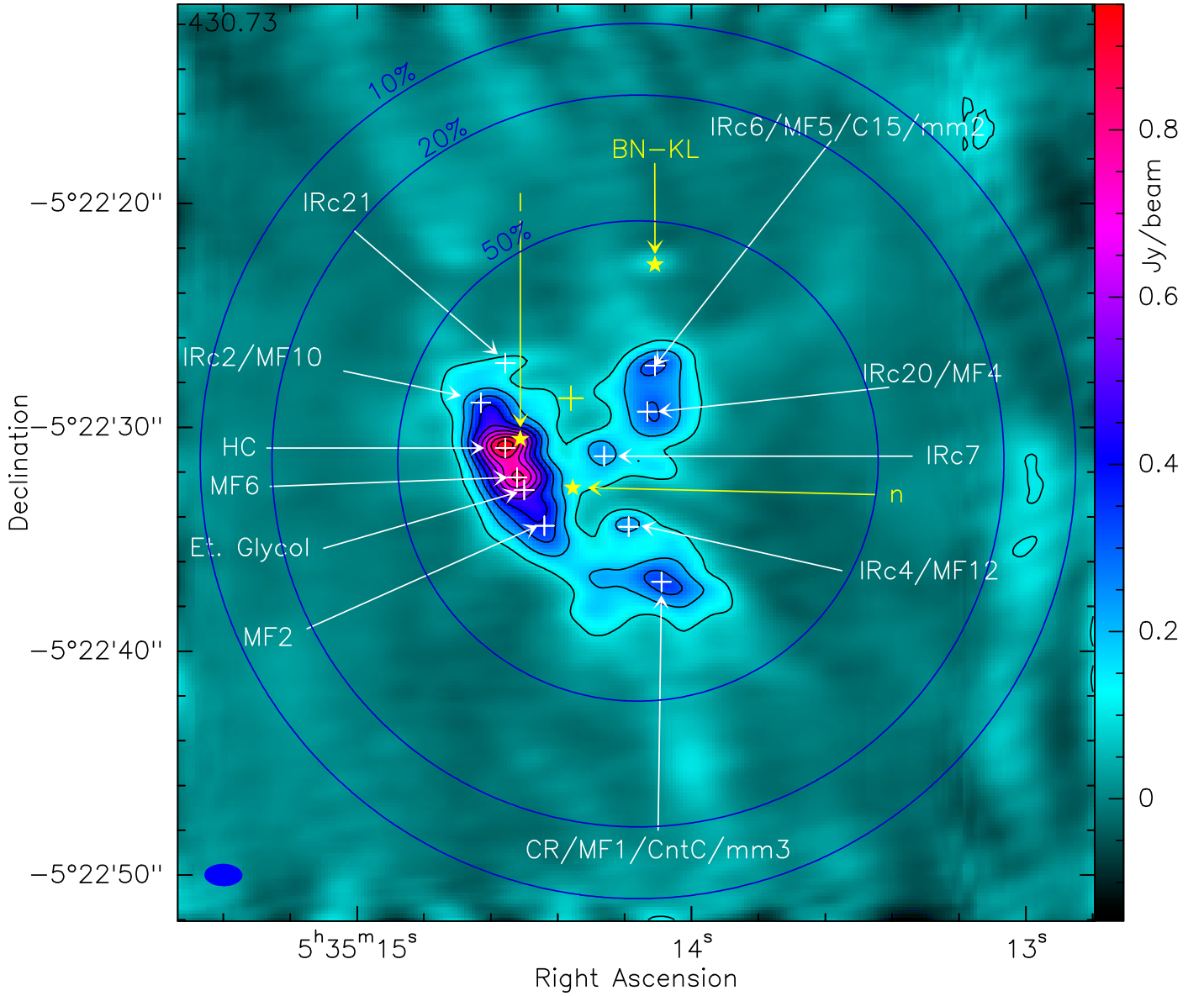


Fig. 1. Continuum flux image of Orion – KL at ~ 1.3 mm, from an assemblage of channels free of line emission. The contours are every 100 mJy/beam (uncorrected for primary beam coupling). The ten sources analyzed in detail in this work are indicated and labeled (other labels of the same sources can be found in SIMBAD/CDS): HC = hot core, CR = compact ridge, MFxx from Favre et al. (2011), Cxx from Friedel & Weaver (2011), IRcxx from Rieke et al. (1973); Shuping et al. (2004), mmxx from Feng et al. (2015) and references therein. The yellow cross indicates the center of explosion from which the BN, I, and n sources (marked by yellow stars) are moving away (Gómez et al. 2005). The blue circles mark the primary beam coupling efficiency (though the size changes by $\pm 8\%$ with frequency, decreasing with increasing frequency, we keep the same median case for all the figures). The primary beam coupling correction is not applied in the present and following figures.

extended emission is reduced by the lack of zero-spacing data. For the strongest lines this is clearly seen in their distorted line shape, including strongly negative channels (see, e.g., the SO line at 215220.653 MHz in Fig. 2) and what it would be from an estimated fit (Fig. A.3a).

3.3. Detection of new species and new vibrationally excited states in Orion

We report the first detection in Orion of gGg' ethylene glycol conformer ($(\text{CH}_2\text{OH})_2$) and of acetic acid (CH_3COOH), which will be presented elsewhere (Favre et al. *subm.*). We have also detected for the first time in Orion, n- and i-propyl cyanide conformers ($\text{C}_3\text{H}_7\text{CN}$). A few cyanoacetylene (HC_3N) vibrationally excited transitions are also (probably) detected here for the first

time, both for the main isotopologue and for the three singly ^{13}C substituted isotopologues (some of them have been reported in Esplugues et al. 2013 and a contemporary paper published after the submission of the present paper also presents a study of some of these vibrationally excited states, Peng et al. 2017). Except for the gGg' ethylene glycol conformer, only detected towards IRAS16293 A/B (Jørgensen et al. 2016), all the species we present here have been seen in some other massive star forming regions, especially in Sgr B2 (B13 discuss all of these detections concerned with Sgr B2 though some predate that work).

3.3.1. Propyl cyanide $\text{C}_3\text{H}_7\text{CN}$

Both n- and i-propyl cyanide conformers are detected (spectroscopic data are provided by Demaison & Dreizler 1982;

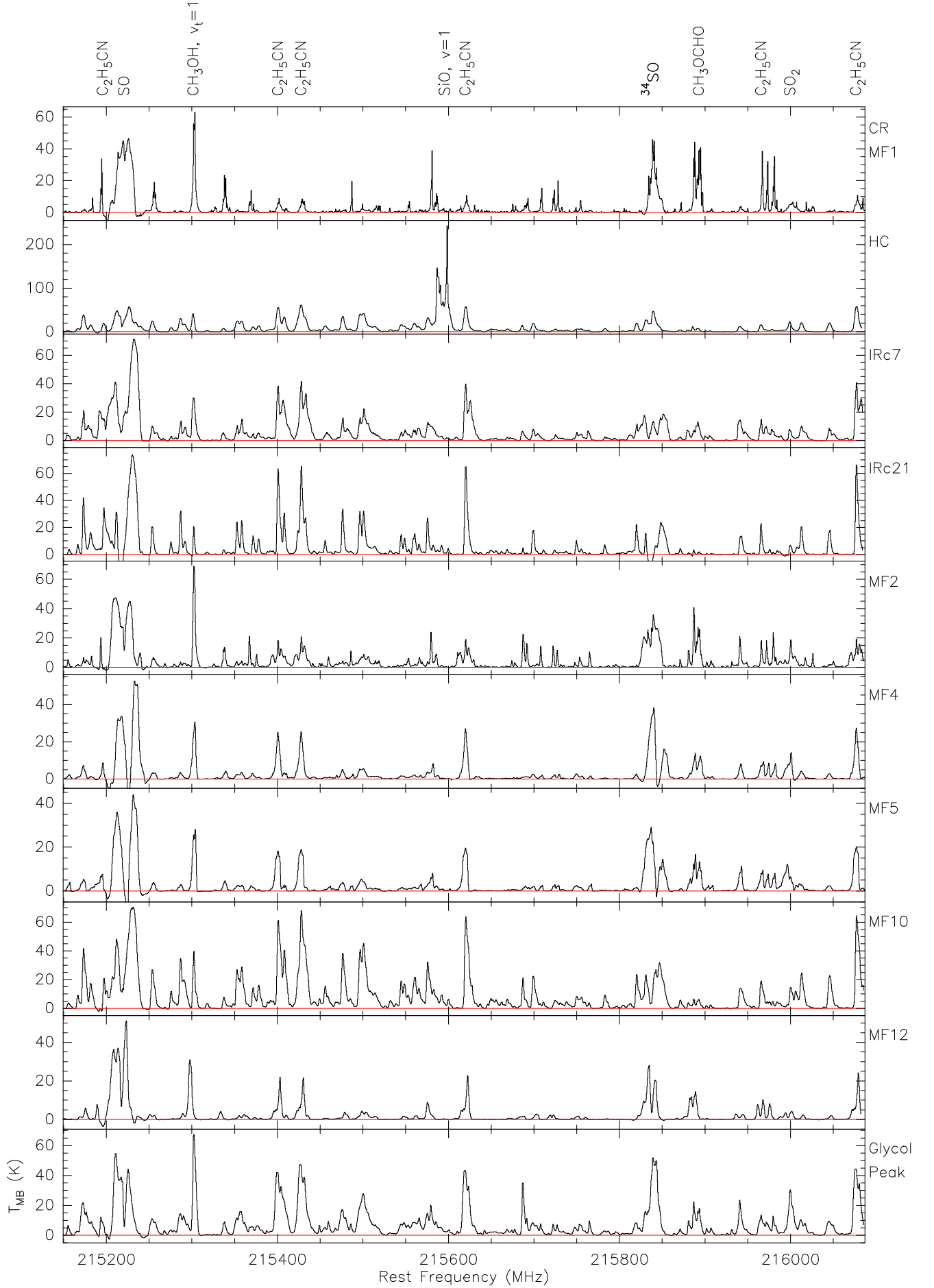


Fig. 2. Spectra from the band 1 setup for all ten sources. The red line indicates the 0 K (continuum-removed) level.

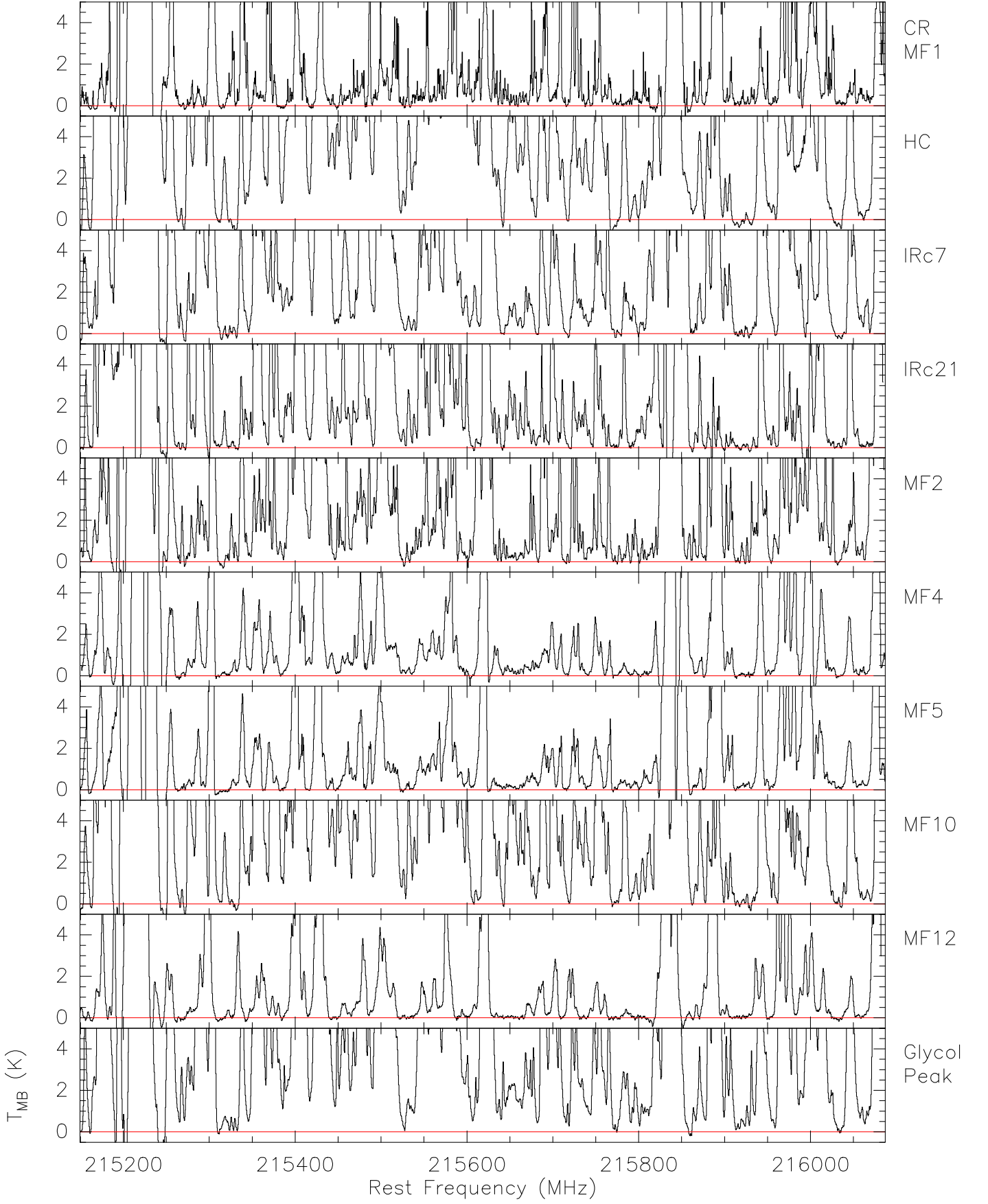


Fig. 3. Spectra from the band 1 setup for all ten sources with a fixed maximum temperature scale of 5 K to highlight the weaker lines. The red line indicates the 0 K (continuum-removed) level.

Table 2. Orion–KL molecular components.

Component	RA _{J2000} 05 ^h 35 ^m ..	Dec _{J2000} -05°22'..	size (arcsec)	v _{LSR} (km s ⁻¹)	Δv (km s ⁻¹)	T _{Kin} (K)	n(H ₂) (cm ⁻³)	N(H ₂) (cm ⁻²)
Extended Ridge	14:6	21:5	~180	8 – 10	2.5 – 5	40 – 60	~1 × 10 ⁵	7.1 × 10 ²²
Plateau	14:516	30:59	20 – 30	5 – 10	20	95 – 150	1 – 10 × 10 ⁶	1.8 × 10 ²³
Hot Core	14:6	31:0	5 – 10	4 – 6	5 – 15	150 – 400	1 – 10 × 10 ⁷	3.1 – 10 × 10 ²³
Hot Core (peak)							7.3 × 10 ⁸	5.4 × 10 ²⁴
Compact Ridge/MF1	14:09	36:9	5 – 15	7 – 9	1 – 2	80 – 150	1 – 10 × 10 ⁶	3.9 × 10 ²³
Compact Ridge (peak)							6.8 × 10 ⁸	5.0 × 10 ²⁴
IRc7	14:26	31:29	~2	-2 – 8	2.5 – 5	~160	–	–
IRc21	14:557	27:13	~2	~6	2.5	~160	–	–
MF2	14:44	34:4	~2	3 – 17	2.5 – 6	100 – 150	4.2 × 10 ⁸	3.1 × 10 ²⁴
MF4/IRc20	14:132	29:3	~2	7 – 14	2 – 8	~100	2.2 × 10 ⁸	1.6 × 10 ²⁴
MF5/IRc6	14:158	27:83	~2	6.5 – 13	2.5 – 6	~100	2.2 × 10 ⁸	1.6 × 10 ²⁴
MF10/IRc2	14:63	28:9	~2	-3 – 7	3 – 5	150 – 200	–	–
MF12/IRc4	14:188	34:44	~2	0 – 11	2 – 5	100 – 150	–	–
EGP	14:47	33:17	~2	-7 – 12	3 – 6	100 – 140	–	–

Notes. For further details see Irvine et al. (1987), Blake et al. (1987), and Favre et al. (2011). Extended Ridge and Plateau are quoted for completeness but not discussed in this paper, their positions are simply given as those of Orion KL and Source I, respectively. All other source positions and sizes are from this paper or from Favre et al. (2011) except EGP = Ethylene Glycol peak from Brouillet et al. (2015). Peak densities and column densities for the HC and the CR and for some of the MF peaks are measured in a 1.8''×0.8'' beam (Favre et al. 2011) but should be considered cautiously. Our positions of IRc7 and IRc21 are closer to the positions of C23 and C13 sources of Friedel & Weaver (2011) than to the IRc positions of Shuping et al. (2004) while they are probably the same objects, respectively.

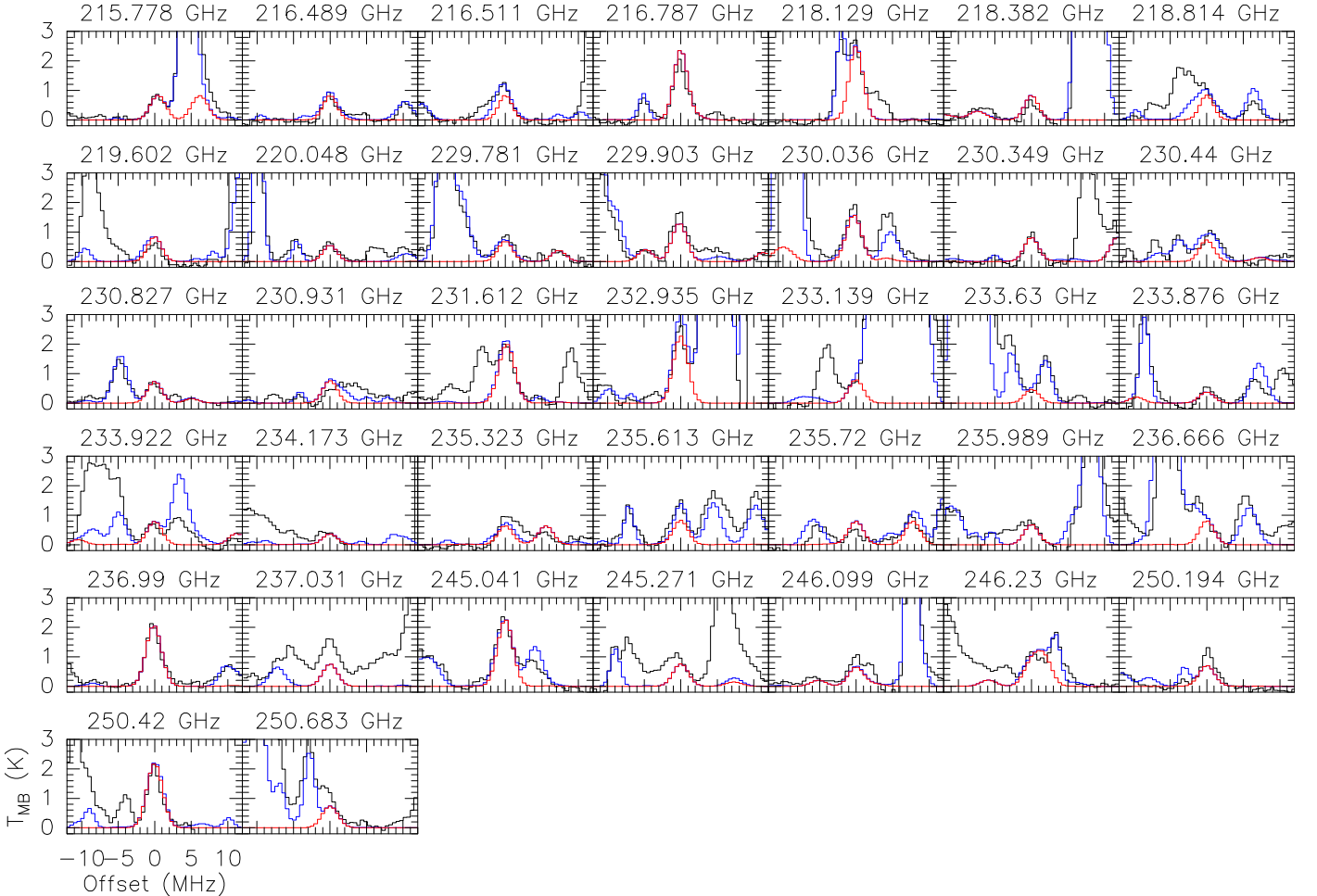


Fig. 4a. Detection of n-C₃H₇CN propyl cyanide isomer towards IRC21 (see map Fig. 1). In this and the following figures, the most intense lines are displayed (i.e. lines typically stronger than ~5 σ . Weaker lines are hardly or not at all detectable and have no impact on the results, nor do lines blended with much stronger lines of other species). The data are in black and the fit is in red. The summation of the fit of all the species we have identified is displayed in blue.

Vormann & Dreizler 1988; Włodarczak et al. 1988 for the n isomer and by Müller et al. 2011 for the i isomer). We mainly detect them towards IRC7, IRC21, MF2, and MF10, with a tentative detection of the n conformer towards EGP (Figs. 4a and b). Since the spatial extent of these two species is limited, we can estimate a first-order LTE column density for a given temperature. Towards the IRC21 peak, we find a column density of

In the case of such relatively rare species, blending with other species in different portions of the region is unavoidable, and therefore an intensity map of the species emission would be misleading. Figure 5 shows the integrated line intensity contour map of the seemingly isolated 236.990 GHz transition (Fig. 4a) superimposed on the continuum map of the region. While $\text{C}_3\text{H}_7\text{CN}$ seems to clearly peak on MF2, the real peak is towards IRc21. The MF2 peak presents a mixture of an unidentified line with propyl cyanide at that frequency. The second strongest peak, towards CR/MF1 is purely coincidental and does not represent this species, as the unsuccessful fit attempt shows (Fig. 6). This problem is general and great care should be taken when examining intensity maps of species in Orion. Identification of a species based on a single component in one of the studied sources, even if the species is clearly identified somewhere else in the region, must therefore remain very tentative.

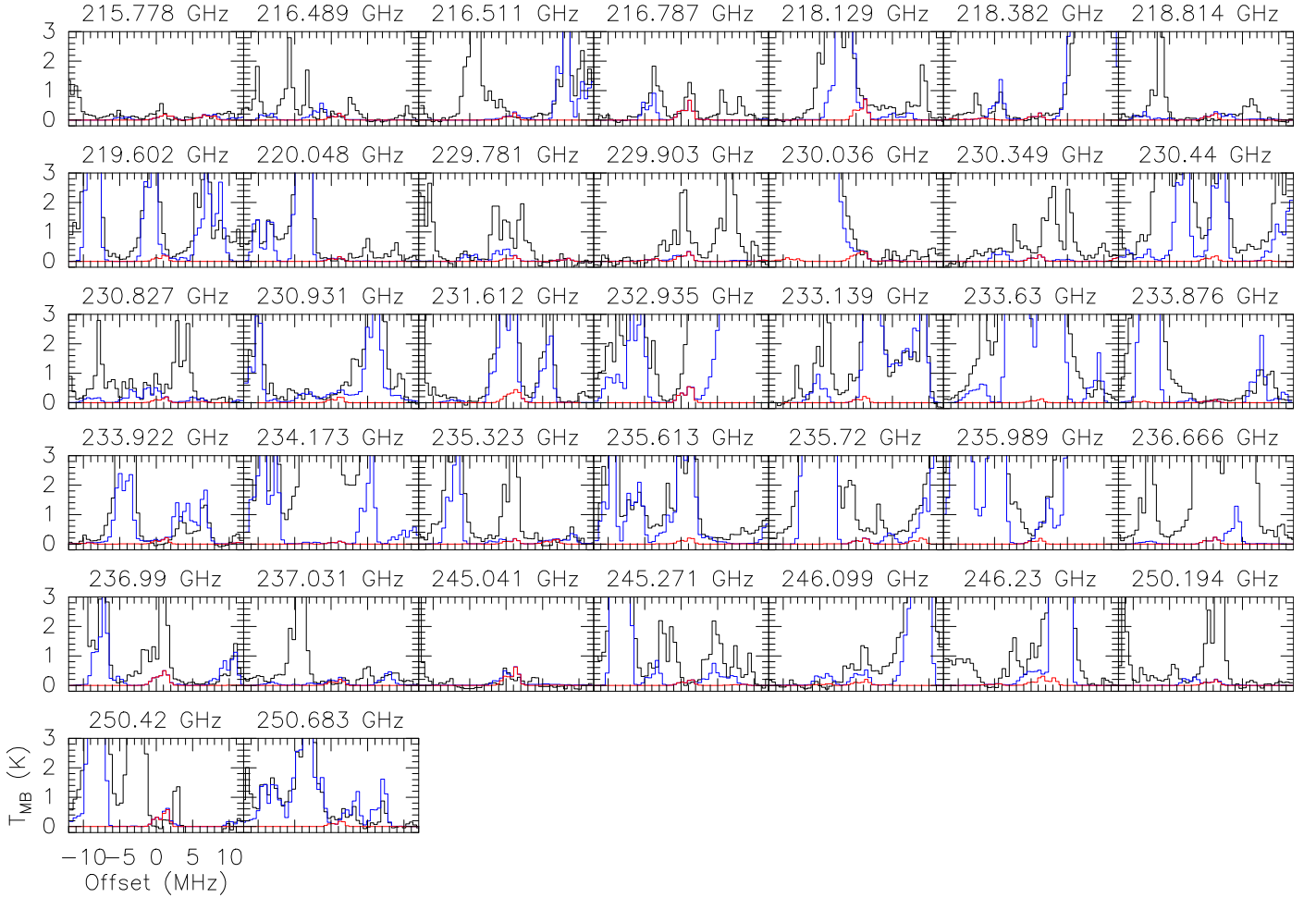


Fig. 6. CR/MF1 display of expected $n\text{-C}_3\text{H}_7\text{CN}$ components. Despite the coincidental emission peak towards CR/MF1 in Fig. 5 that is visible in the 236.99 GHz window, $n\text{-C}_3\text{H}_7\text{CN}$ is not detected in this source at a similar level to that seen in IRc21 (Fig. 4a). Color-coding and T_{MB} scale as in Fig. 4a.

3.3.2. Vibrationally excited HC_3N and ^{13}C singly substituted cyanoacetylene isotopologues

After the early work by Goldsmith et al. (1982, 1983), who detected the first two vibrationally excited states of cyanoacetylene (HC_3N , $v_7 = 1, 2$), there were a few further attempts to identify higher excitation levels in this source, and finally the large work of Esplugues et al. (2013), which combines IRAM 30 m and Herschel HIFI data, reported numerous excited states (up to $v_6=v_7=1$). It can also be noted that vibrationally excited states of numerous other species are now known (e.g. Daly et al. 2013; López et al. 2014). Turner (1991) invokes the HC_3N $v_6 = 1$ transition in his analysis of a 3 mm NRAO survey, but all the transitions are always mixed with $v_7 = 1$ lines and are not detected separately. Since the $v_7 = 1$ lines are much stronger, the actual identification of the $v_6 = 1$ mode was not secure. de Vicente et al. (2002) report the detection of $v_5 = 1$, $v_6 = 1$, and $v_7 = 1$. They claim to have detected all these excited states, but show no data for $v_6 = 1$. Simultaneously with and independently from this work, Peng et al. (2017) published a study based on the SV0 data on part of the vibrationally excited states we report here. We note that in their study they present the $v_5 = 1$ and $v_7 = 3$ data separately, while the CDMS present them together, which is the recommended way to proceed since the states are coupled (Fermi coupling, H.S.P. Müller, private communication).

We have detected several vibrationally excited states of HC_3N throughout the region and also the three ^{13}C singly substituted isotopologues, H^{13}CCCN , HC^{13}CCN , and HCC^{13}CN . Spectroscopic data are taken from Thorwirth et al. (2000), which is the most recent published measurement for HC_3N , and from Thorwirth et al. (2001) for the ^{13}C isotopologues. The highest energy vibrationally excited state we can report with confidence is the $v_6=v_7=1$ state, at $E_{\text{up}} \approx 1170$ K and the emission is located near the HC. These are the same states as reported by Esplugues et al. (2013) from their single-dish survey. The next states, in the range 1400 - 1600 K, ($v_7=4/v_7=v_5=1$, $v_4=1$, and $v_6=2$) are possibly seen but not securely detected³ (Fig. 7). Other excited states are reported from Sgr B2 observations in B13 but were not found in our data. Since the vibrationally excited modes are probably pumped by IR radiation, we did not try to evaluate the column density for any of these states since their temperature is not physically related to the local gas temperature. Furthermore, their excitation temperature within each vibrational state involves transitions with upper levels too close in energy to allow a secure rotational diagram analysis to be performed. As previously noted by several authors (e.g. Feng et al. 2015; Peng et al. 2017), these excited modes are mostly situated in the northern part of the region (Fig. 8). Indeed, though the $v_7 = 1$ and 2 states are detected

³For an energy level diagram of the vibrational states of HC_3N , see Yamada & Creswell (1986)

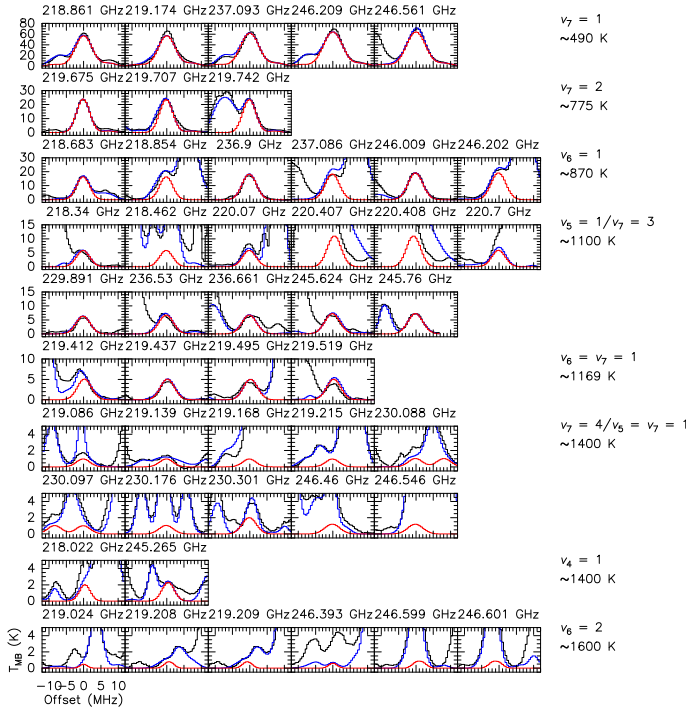


Fig. 7. Cyanoacetylene (HC_3N) vibrationally excited transitions towards the HC. The fits help to trace the components, but have limited physical significance because their temperature is not constrained. The $v_7 = 1$ line at 218.861 or 237.093 GHz displays a shoulder due to the $v_6 = 1$ at 218.854 and 237.086 GHz, respectively). Color-coding as in Fig. 4a.

even towards the CR in the southern part of the region, the higher states are only detected farther north. The excited state emission is mostly concentrated in an arc around the explosion center (Fig. 8). If they are related, it would be via collisional excitation rather than infrared pumping but all species emitting in the same arc do not seem to show the same high excitation level. We discuss the possible impact of the 500-year-old explosion in Sect. 4.4 and in a future paper on the different behavior of cyanide- and oxygen-bearing complex organic molecules in Orion-KL (Pagani et al. in prep.).

We have also detected the ^{13}C singly substituted cyanoacetylene isotopologues in the vibrational states $v_7 = 1$ & 2. The next vibrational level ($v_6 = 1$) is most probably present, but all lines are weak and often blended (the H^{13}CCCN $v_6 = 1$ vibrational state has no transitions in our bands). Towards IRC21 (named HC-North in Peng et al. 2017), the lines are stronger and less blended than towards HC and give better results (Fig. 9).

3.4. Tentative detection of new species in Orion

A number of species, already known in the interstellar medium but not detected in Orion to the best of our knowledge, have been tentatively detected in this survey. Caution should be exercised, however. As we discuss in Sect. 3.5.1, even the detection of three lines of a species is not a clear proof of its presence, independent of their signal-to-noise ratios. We therefore report these tentative detections for the sake of completeness. The addition of zero-spacing data in the future will possibly allow a better cleaning of the spectra and we hope that some of these detections

will be secured. All the basic information for these species can be found at the CDMS webpage “Molecules in Space”⁴.

3.4.1. Methylamine CH_3NH_2

Methylamine was detected early on towards Sgr B2 (Kaifu et al. 1974; Fourikis et al. 1974). The same papers report its detection in Orion, but Johansson et al. (1984) proved these detections to be incorrect⁵. To the best of our knowledge, this species has not been reported in Orion since these early works. The line remains difficult to identify, but towards the Hot Core, a tentative detection can be reported thanks to several lines fitting the expected emission (Fig. 10, spectroscopic data are provided by Motiyenko et al. 2014). Possible detections are also found towards IRC7, MF2, MF5, and MF10. Towards the HC, for $T_{\text{ex}} = 280$ K, we find a column density of $1 \times 10^{16} \text{ cm}^{-2}$.

3.4.2. Cyanamide NH_2CN

This species has been tentatively detected by López et al. (2014). Our detection confirms their work (still tentatively), but the signal seems to come primarily from the EGP rather than from the HC (which López et al. 2014 could not distinguish in their single-dish data), 2'' farther north, and at a velocity of 8 km s^{-1} instead of 5 (Fig. 11). Towards the EGP, the fit indicates a column density of $1.1 \times 10^{14} \text{ cm}^{-2}$ for $T_{\text{ex}} = 140$ K. Spectroscopic data are provided by Johnson et al. (1976); Moruzzi et al. (1998).

3.4.3. Glycolaldehyde $\text{CH}_2(\text{OH})\text{CHO}$

Of the three $\text{C}_2\text{H}_4\text{O}_2$ isomers, glycolaldehyde, acetic acid, and methyl formate, only the last is widely spread in molecular clouds and already known in Orion. Our detection of glycolaldehyde is somewhat uncertain because many lines are blended and we conservatively declare the detection to be tentative (Fig. 12). Though the fitting parameters are equivalent towards the Glycol Peak and MF2, the blending is slightly less severe towards MF2, which we display here. Spectroscopic data are provided by Butler et al. (2001).

3.4.4. ^{13}C doubly substituted cyanoacetylene isotopologues

The ^{13}C doubly substituted cyanoacetylene isotopologues have still only been tentatively detected in CRL618 (Pardo & Cernicharo 2007) and Sgr B2 (Belloche et al. 2016). Again, in Orion, the three ^{13}C doubly substituted cyanoacetylene isotopologues are possibly detected towards IRC21 in the fundamental vibrational state (Fig. 13). The abundance ratio, in the ground vibrational state, between singly (averaged over the three isotopologues) and doubly substituted isotopologues is ~ 45 , but because of blending, this value is likely underestimated but consistent with previous reports (Pardo & Cernicharo 2007; Belloche et al. 2016). Spectroscopic data are provided by Thorwirth et al. (2001).

3.4.5. ^{13}C substituted Iminomethylum, $\text{H}^{13}\text{CNH}^+$

To the best of our knowledge, iminomethylum (HCNH^+) has not yet been reported in Orion. This cation has no transition in

⁴<http://www.astro.uni-koeln.de/cdms/molecules>

⁵This information has been taken from the CDMS webpage on methylamine: <http://www.astro.uni-koeln.de/site/vorhersagen/molecules/ism/MeNH2.html>

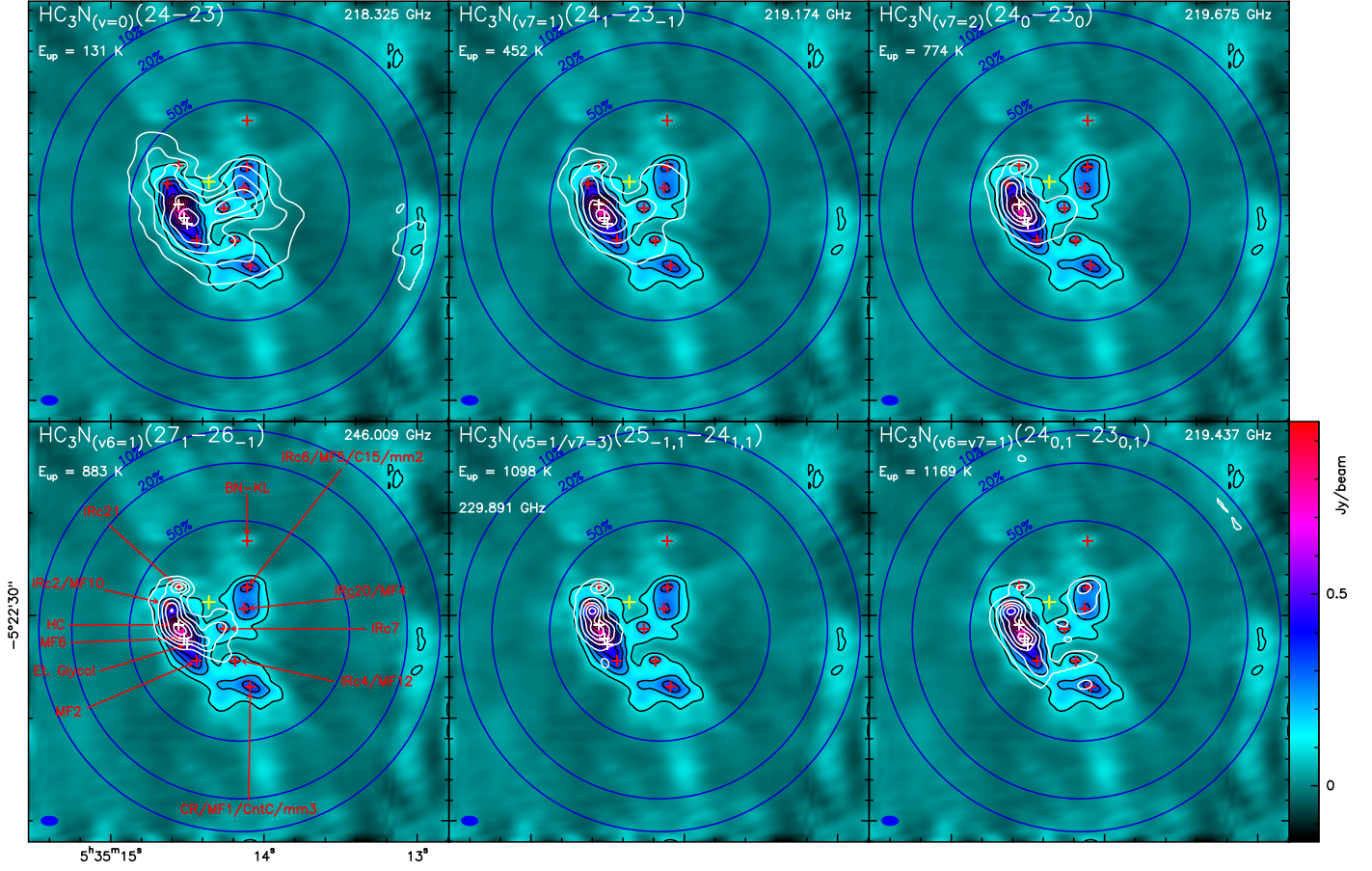


Fig. 8. Integrated line intensity of cyanoacetylene vibrational modes (from $v = 0$ to $v_6 = v_7 = 1$ (white contours) superimposed on the continuum image of the region. In the $v_6 = v_7 = 1$ image, contours towards CR/MF1, MF2, MF4, MF5, and MF12 are not related to HC_3N .

our frequency coverage. Its ($J:3 - 2$) line, where J is the rotational quantum number (representing the total angular momentum excluding nuclear spin), is at 222.329 GHz. Its presence must be verified in the reduced SV0 data as soon as they become available. The ^{13}C substituted isotopologue, $\text{H}^{13}\text{CNH}^+$ is observed in a single transition within the frequency range covered, and is identified towards all sources, being the strongest towards CR/MF1 (Fig. 14). With only one line observed, it can at best be a tentative detection, since the density of unknown lines above 10 K is $\sim 3.8 \text{ GHz}^{-1}$ towards CR/MF1. It is only ~ 3 K in MF2 and is weak everywhere else (0.5 – 1.0 K). If confirmed, the higher abundance of iminomethylum in the richest source in oxygen-carrier complex organic molecules (hereafter O-COMs) is an interesting chemical problem, which is beyond the scope of this paper. Spectroscopy data are provided by Amano & Tanaka (1986).

3.4.6. Propanal $\text{CH}_3\text{CH}_2\text{CHO}$, propenal CH_2CHCHO , and propynal CHCCHO

The three aldehydes derived from propane, propene and propyne have never been observed in Orion. Their large number of transitions and weak emission due to a relatively low abundance in this source make them difficult to detect, especially when the zero-spacing data is missing, producing negative features that can erase weak signals at the limit of sensitivity of the observations. We possibly detect propanal (spectroscopic data are provided by Hardy et al. 1982; Demaison et al. 1987) and propenal (spectroscopic data are provided by Daly et al. 2015) towards

IRc21 (Figs. 15 and 16) and very tentatively propynal (spectroscopic data are provided by Winnewisser 1973; McKellar et al. 2008; Barros et al. 2015) towards the EGP (Fig. 17). Concerning propenal, three or possibly four very weak lines at the 3–5 σ level are not seen out of the strongest 23 lines we report (all remaining lines not presented here are too weak to be detectable in our data). We consider that these non-detections are not significant. Propynal is not seen towards the same source because all propynal lines are weak and blended except the possible pair we present here. The 217.437 propynal transition is somewhat displaced compared to the observed peak and therefore possibly not real. The frequency displacement (1.5 MHz) is larger than the uncertainty on the transition frequency (59 kHz) even when combined with the $0.2 - 0.3 \text{ km s}^{-1}$ fluctuation we often encounter in the fitting process. Since we present only two lines for this species, this must remain a highly tentative identification.

3.5. Non-confirmation of species in Orion

In two recent papers (Feng et al. 2015; Liseau & Larsson 2015) a tentative detection of three species has been reported. We do not confirm these detections, as discussed below.

3.5.1. Hexatriynyl C_6H

Feng et al. (2015) report the tentative detection of hexatriynyl, C_6H , a precursor of the C_6H^- anion. They indicate that the only unblended line in their survey appears at 230.109 GHz towards

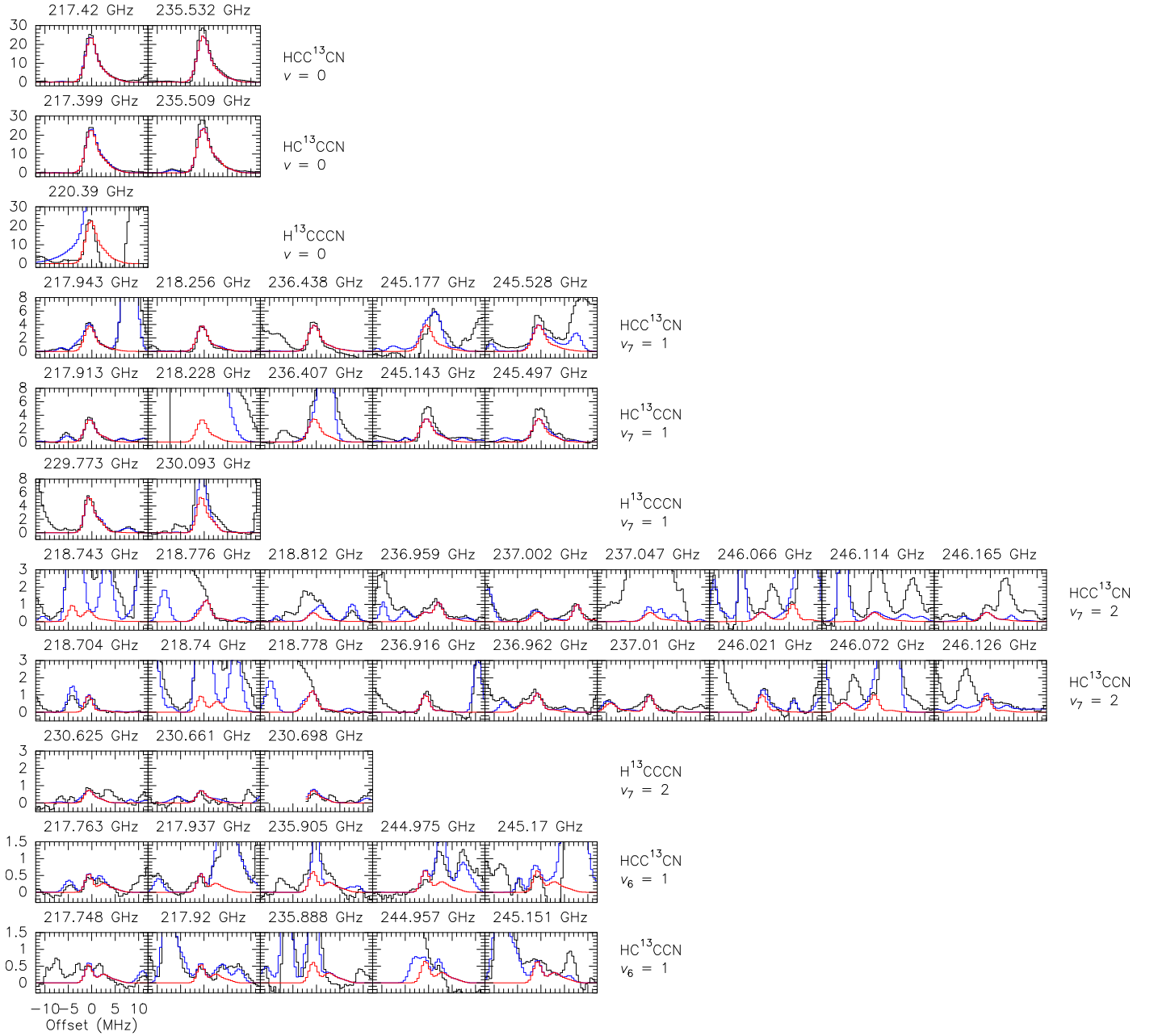


Fig. 9. Singly ^{13}C substituted cyanoacetylene isotopologue lines in fundamental and first vibrationally excited modes towards IRC21. The $\text{H}^{13}\text{CCCN } v_6 = 1$ mode has no transition in our bands. Color-coding as in Fig. 4a.

their SMA1 source, $0''.5$ away from MF6 westward, though their Fig. A2 shows equally unblended lines at 220.355 and 220.487 GHz, which they fit. We find that the 230.109 GHz line is partly explained by a vibrationally excited vinyl cyanide component ($\text{C}_2\text{H}_3\text{CN}, v_{11} = 1$) at 230.106 GHz, which only contributes to half of the observed line in width.

Though C_6H emission could still be present (but blended with vinyl cyanide on one side and some unknown species on the other side) in this frequency window, 7 of the 21 other predicted lines (spectroscopic data are provided by Linnartz et al. 1999) falling in our survey range are not detected at all, a few others are already explained by more common species, and a few more are severely blended (Fig. 18). To better identify the possible contributors, we have also checked the C_6H emission in the direction of the nearby HC (1''.1 northeast of SMA1), see Fig. 19. There is less confusion in this direction than towards

SMA1 and even more lines appear to be in disagreement. The handful of lines that could be partly explained by the C_6H emission (at 217.7, 232.9, 235.8, and 250.8 GHz) are always much weaker than the prediction we make in order to fit the 231.1 GHz line. Other lines are readily explained without C_6H . In particular, the 219.086 GHz line is due to a combination of vibrationally excited vinyl cyanide ($\text{C}_2\text{H}_3\text{CN}, v_{15} = 1$) and vibrationally excited cyanoacetylene ($\text{HC}_3\text{N}, v_7=4/v_7=v_5=1$) lines at 219.085 and 219.086 GHz, respectively; the 220.355 GHz line is due to an acetone (CH_3COCH_3) transition at the same frequency; and the 220.487 GHz line is due to a ^{13}C substituted methyl cyanide ($\text{CH}_3^{13}\text{CN}$) transition at 220.486 GHz. Since all C_6H lines have comparable Einstein coefficients and since their E_{up} levels fall in a relatively narrow and high range of temperatures (415 – 550 K), it seems difficult to explain the 230.109 GHz feature as C_6H while avoiding having other lines appear at some of the

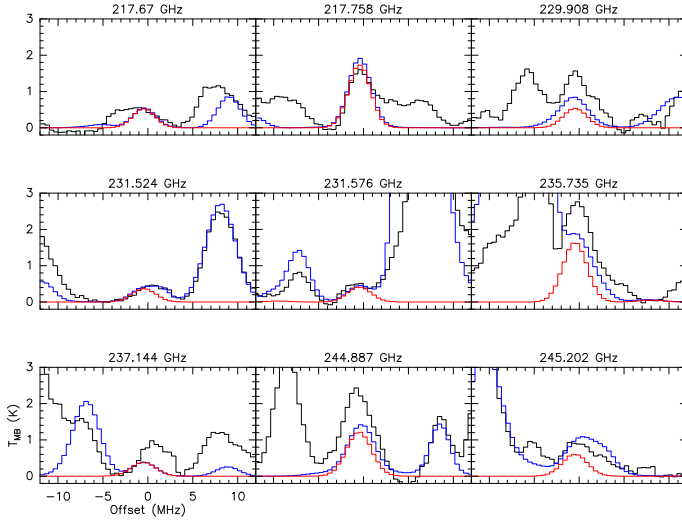


Fig. 10. Methilamine (CH_3NH_2) emission towards the Hot Core. Color-coding as in Fig. 4a.

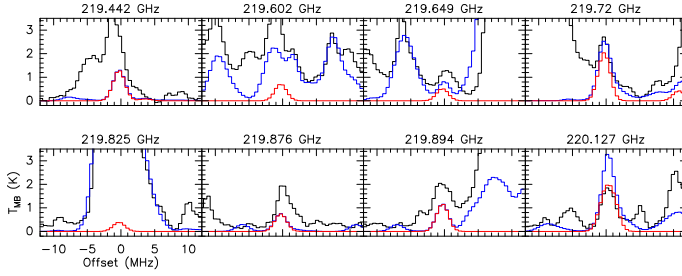


Fig. 11. Cyanamide (NH_2CN) detection towards the EGP. Color-coding as in Fig. 4a.

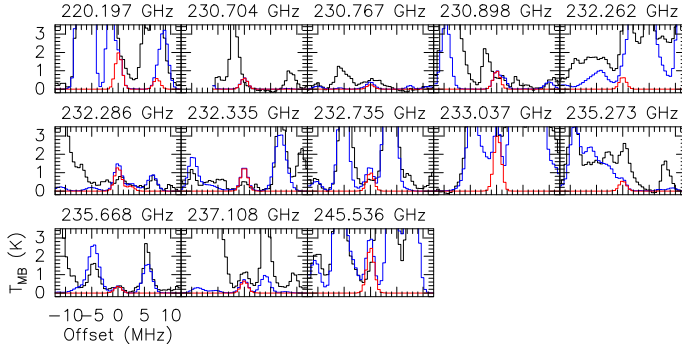


Fig. 12. Tentative detection of glycolaldehyde ($\text{CH}_2(\text{OH})\text{CHO}$) towards MF2. Color coding as in Fig. 4a.

other frequencies. We therefore do not confirm the detection of C_6H .

3.5.2. Cyanoheptatriyne HC_7N

Feng et al. (2015) also report the tentative detection of cyanoheptatriyne, HC_7N , north of the HC. From their Fig. 5, the peak is approximately $2''$ due north of HC. This is close to IRc2/MF10, but $1''$ to the west. Though the reported lines have an $E_{\text{up}} \geq 1000$ K, which would limit their detectability to the hottest region in Orion-KL (namely the HC), it should be noted that the vibrationally excited cyanoacetylene lines with equivalent E_{up} of ~ 1000 K are equally strong from the HC to IRc2/MF10.

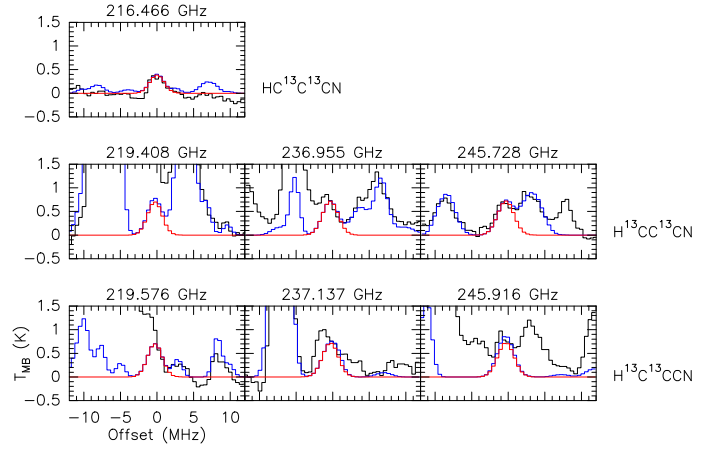


Fig. 13. Tentative detection of the ^{13}C doubly substituted cyanoacetylene isotopologue lines towards IRc21. Color-coding as in Fig. 4a.

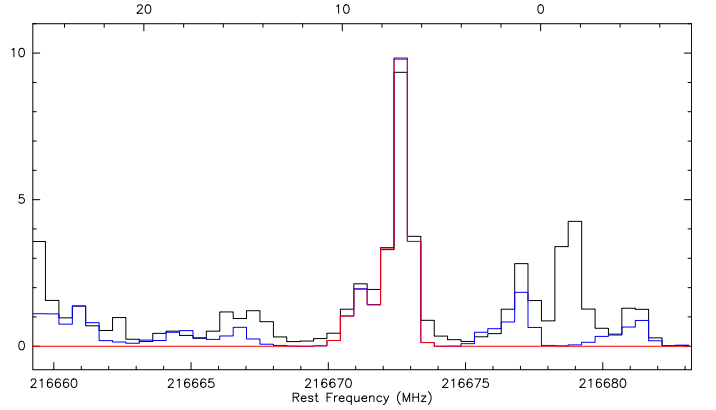


Fig. 14. Possible $\text{H}^{13}\text{CNH}^+$ line towards CR/MF1. The line is present at both LSR velocities (axis above figure) for this source.

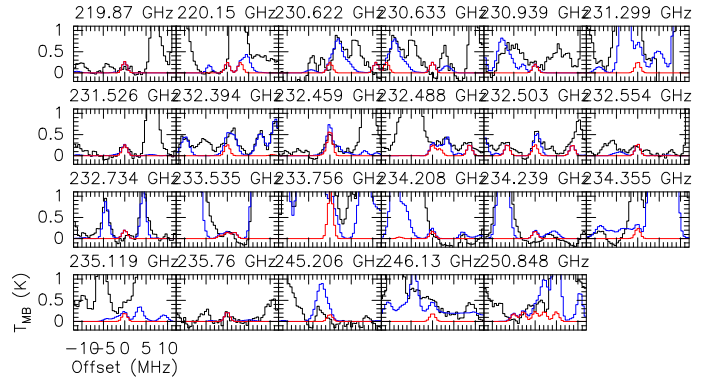


Fig. 15. Tentative detection of propanal towards IRc21. Color coding as in Fig. 4a.

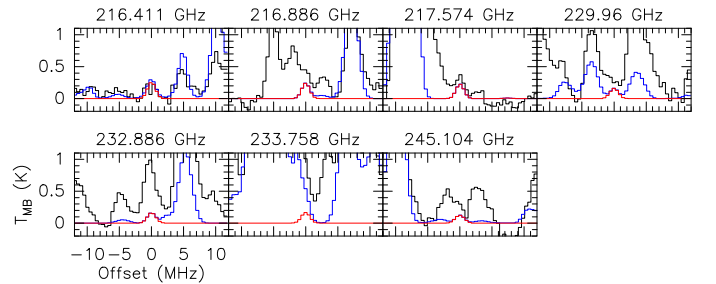


Fig. 16. Tentative detection of propanal towards IRc21. Color coding as in Fig. 4a.

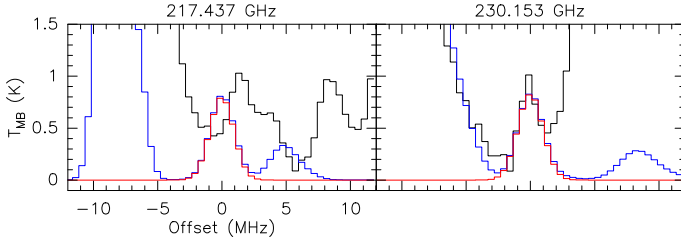


Fig. 17. Highly tentative detection of propynal towards the EGP. Color coding as in Fig. 4a.

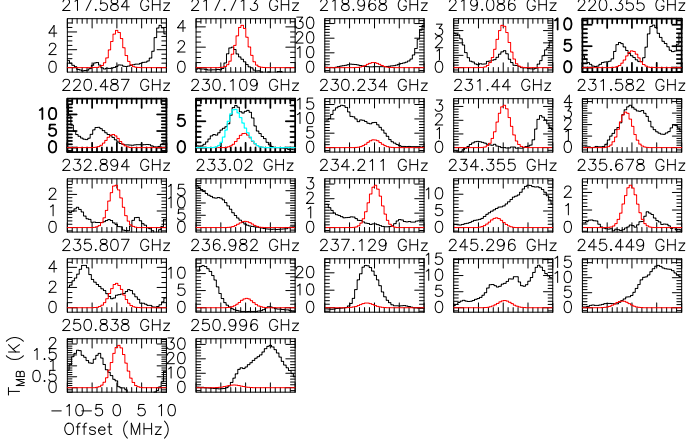


Fig. 18. Observations of hexatriynyl (C_6H) towards SMA1 following the Feng et al. (2015) tentative detection. The three lines presented by Feng et al. (2015) are marked by thick boxes. Data are in black, the C_6H model following the Feng et al. (2015) parameters in red, and its combination with vinyl cyanide at 230.108 GHz in cyan.

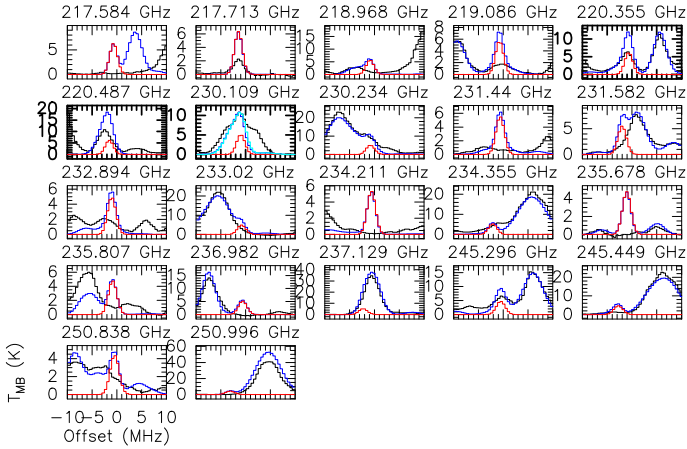


Fig. 19. Observations of hexatriynyl (C_6H) towards the HC. The three lines presented by Feng et al. (2015) are marked by thick boxes. Data are in black, C_6H modeling in red, and other species modeled in blue. The combination of C_6H and vinyl cyanide emission at 230.109 GHz is shown in cyan.

However, the emission area of HC_7N in their Fig. 5 is not strictly coincident with this region.

Two of the four transitions in their survey range are detected and are unblended. These are the $J:196 \rightarrow 195$ and $J:205 \rightarrow 204$ transitions at 220.967 and 231.102 GHz, respectively, but they do not detect the $J:195 \rightarrow 194$ and $J:204 \rightarrow 203$ transitions at 219.841 and 229.976 GHz. This species has been possibly detected by Turner (1991) at a very low level together with HC_5N , which we do not detect either (Sect. 3.7.4).

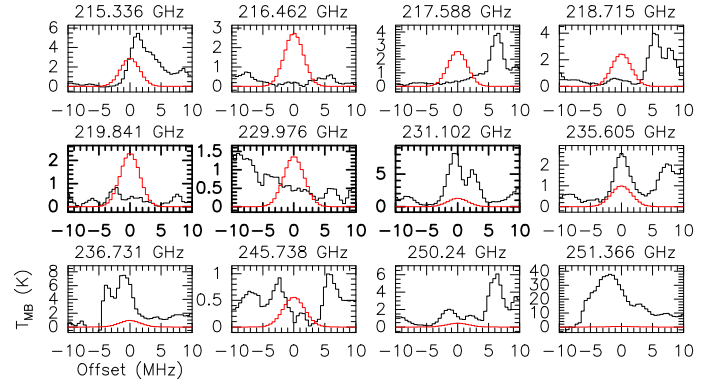


Fig. 20. Observations towards the HC_7N peak found by Feng et al. (2015) of the 12 cyanohexatriyne (HC_7N) transitions recorded in our survey. Three of the four lines presented by Feng et al. (2015) are marked by thick boxes (the last one is missing from our survey). Data are in black, HC_7N model following the Feng et al. (2015) parameters in red.

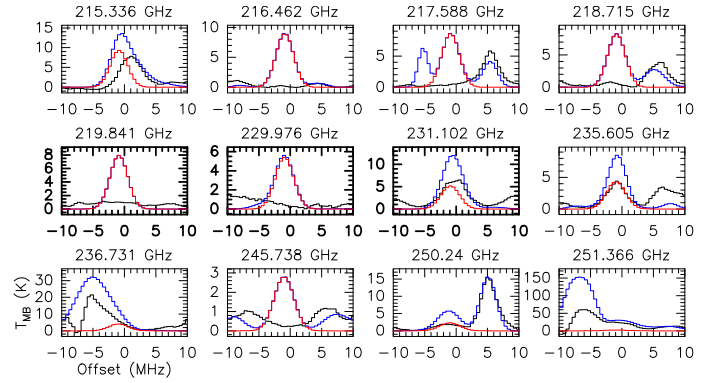


Fig. 21. Observations towards the HC of the 12 cyanohexatriyne (HC_7N) transitions recorded in our survey. Three of the four lines within the Feng et al. (2015) survey are marked by thick boxes. Data are in black, HC_7N model following the Feng et al. (2015) parameters in red, other species modeling in blue.

The $J:196 \rightarrow 195$ transition is outside our survey coverage, but we observed a total of 12 transitions (spectroscopic data are provided by Kirby et al. 1980; McCarthy et al. 2000; Bizzocchi & Degli Esposti 2004) including the three other transitions discussed by Feng et al. (2015). We adopt the Feng et al. (2015) parameters to compute the LTE line intensity ($T_{ex} = 155$ K, $N = 1 \times 10^{16} \text{ cm}^{-2}$, $\delta v = 5 \text{ km s}^{-1}$) and compare it to our data towards the emission peak of their map (Fig. 20). We do not find the same line shapes probably because our beam is much smaller and we are missing the zero-spacing data. Again, we have looked at the nearby HC region (Fig. 21) where we can run our full spectral model. Here we have increased the temperature to 200 K, which is probably the minimum temperature towards the HC, to better fit the observations, in particular the 231.1 and the 235.6 GHz lines. Six lines are completely absent and the other lines are already explained by other species. In particular, the 215.3 GHz line is due to vibrationally excited ethyl cyanide (C_2H_5CN , $v_{20} = 1$), the 231.1 GHz line is due to vibrationally excited vinyl cyanide (C_2H_3CN , $v_{11} = 1$), the 235.6 GHz line is due to acetone (CH_3COCH_3), and the 250.2 GHz line is due to a ^{13}C substituted ethyl cyanide ($C_2H_5^{13}CN$) transition. The detection of HC_7N is therefore not confirmed.

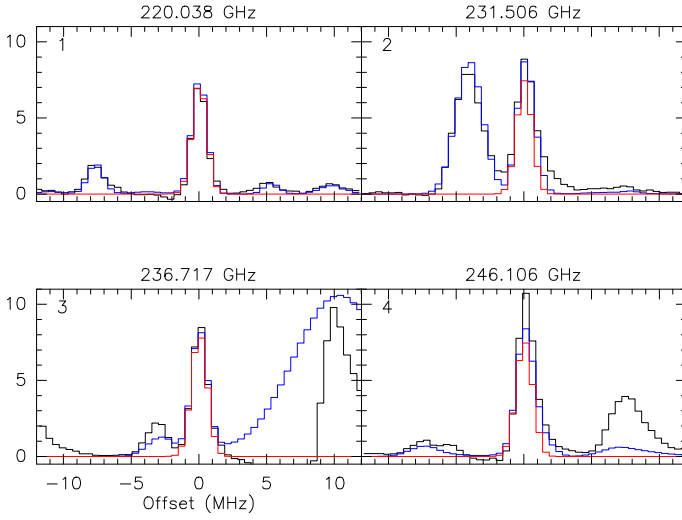


Fig. 22. Observations of formic acid (HCOOH) towards IRC21. Color-coding as in Fig. 4a.

3.5.3. Hydrogen peroxide H_2O_2

Liseau & Larsson (2015) suggested that hydrogen peroxide (H_2O_2) could be present in the region because of the presence of molecular oxygen, in a similar manner to their work in the ρ Oph region. However they consider this detection to be tentative. Their peak emission position at $\text{RA}_{\text{J2000}} 05^{\text{h}}35^{\text{m}}13^{\text{s}}.7$, $\text{Dec}_{\text{J2000}} -05^{\circ}22'27''$ is situated at $(-6''.8, +4''.5)$ from the center of our map, i.e., about $6''$ west of MF5. Apart from the very extended emission of species like CO, CH_3OH , SO, SO_2 , etc. there is no emission visible in this region with ALMA. However, the H_2O_2 line at 219.167 GHz is detected on the edge of a vibrationally excited cyanoacetylene line (HC_3N , $v_7 = 1$, mistakenly written $v_7 = 3$ in their Fig. 1). This can only come from the central part of the Orion – KL region (see Sect. 3.3.2 and Fig. 7), which means that the beam is large enough to detect at least the emission of the $v_7 = 1$ line from the MF4/5 region. It is therefore difficult to locate the exact origin of the small signal they detected. Without the zero-spacing data, we cannot study the extended part of the region, but as far as the core is concerned, the line is not detected in the central parts of the Orion–KL region. Our survey also included the $J_{K_a K_c}:6_{15} \rightarrow 5_{05}$ line at 251.915 GHz — where K_a (resp. K_c) is the projection of N onto the a (resp. c) inertial axis of the asymmetric top, and N is the rotational angular momentum quantum number, excluding electron and nuclear spin — and the $J_{K_a K_c}:4_{23} \rightarrow 5_{15}$ line at 235.956 GHz, which were also not detected (spectroscopic data are provided by Bergman et al. 2011, extracted from Pickett et al. 1998).

3.6. Confirmation of formic acid HCOOH in Orion

Feng et al. (2015) did not detect formic acid in their survey and concluded that the line is only present in extended emission since this species is known from single-dish surveys (e.g. Sutton et al. 1985). This is in contradiction with the observations of this species obtained with the Berkeley-Illinois-Maryland Association Array (BIMA) and reported by Liu et al. (2002). We confirm the detection of this species in several places (spectroscopic data are provided by Winnewisser et al. 2002), some of which were not seen in Liu et al. (2002), for example, IRC21 (Fig. 22). Figure 23 shows strong emission of limited extent centered on IRC21, and weak emission between MF4 and MF5

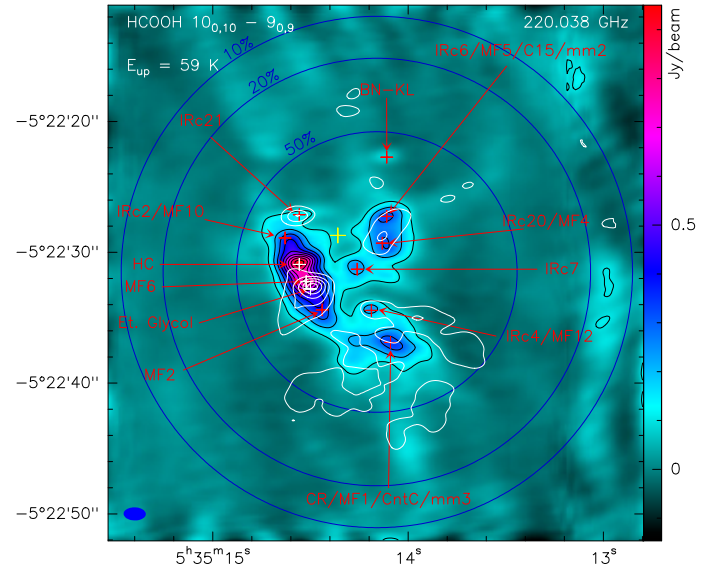


Fig. 23. Integrated intensity map of formic acid (HCOOH) emission at 220.038 GHz (white contours) superimposed on the continuum emission map. The main emission peaks are centered on IRC21 (compact emission) and on the EGP (Et. Glycol) with an extension outside of the region.

and between MF12 and CR/MF1. More extended emission centered on the EGP and expanding away from the explosion center seems to dominate the map. The emission being partly extended in the southern part of the Orion–KL region, the line profile towards the HC and other places seems to suffer from extended emission loss; therefore, the map should be used with caution since part of the flux is missing. The extended emission from the EGP, if real in its shape and extent, is remarkable because it points away from the explosion center. As we propose in Sect. 4.4, this could be linked to accelerated gas coming from the explosion and dragging material along from the dense and hot ridge.

3.7. Non-detection of species in Orion

There is in principle no interest in discussing lines that have not been detected in a source because this represents the vast majority of the molecules we know on Earth. But owing to the high sensitivity of this survey, one could have hoped to detect some of those species already known elsewhere in the interstellar medium, in comets, or mysteriously absent such as the first two we discuss now.

3.7.1. Dioxygen ^{18}O isotopologue $^{16}\text{O}^{18}\text{O}$

During a dedicated Key Program of the Herschel Space Observatory aimed at finding O_2 in the interstellar medium, after the numerous negative results from SWAS (Goldsmith et al. 2000) and Odin (Pagani et al. 2003) spacecrafts, counterbalanced by a single detection in ρ Ophiuchi (Larsson et al. 2007) with Odin, we detected O_2 towards Orion (Goldsmith et al. 2011) and confirmed the detection towards ρ Ophiuchi, (Liseau et al. 2012). However, the location of the emission in Orion is ill-defined and that made the interpretation of the observations difficult (Goldsmith et al. 2011; Chen et al. 2014; Melnick & Kaufman 2015). This is despite the rare velocity value of 11.3 km s^{-1} , which should have limited the probable emission region

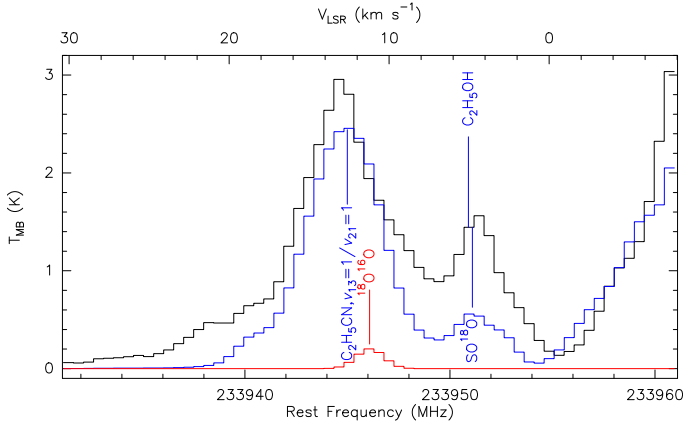


Fig. 24. $^{16}\text{O}^{18}\text{O}$ observations towards MF4. The expected line is traced in blue together with the data (black) and LTE modeling of other species (red). The parameters for these species have been adjusted from other components and do not exactly match the present lines because of the simplicity of the LTE model.

to a few spots at the same LSR velocity as traced by the NH_3 (6,6) inversion transition (Goddi et al. 2011). In the hope of better localizing the emission region, we observed with ALMA both the Orion–KL region and the H_2 vibrational peak farther north in coincidence with the Herschel pointings (Goldsmith et al. 2011; Chen et al. 2014) to try to detect the $^{16}\text{O}^{18}\text{O}$ $\text{N}_j: 2_1 \rightarrow 0_1$ transition at 233.946 GHz. This species has never been found despite numerous attempts (e.g. Goldsmith et al. 1985; Maréchal et al. 1997a; Liseau et al. 2010). From the Herschel observations of the main isotopologue, the line was expected to be very weak (10 mJy/beam in a $5''$ source) and only ALMA could reach the needed sensitivity (2 mJy/beam) in a reasonable amount of time (from Cycle 2 onwards, with at least 37 antennas used during the observations). From the Sutton et al. (1985) survey, the frequency region in the 234 GHz band seemed clear of any strong emission and the prospect of finding $^{16}\text{O}^{18}\text{O}$ looked reasonable.

$^{16}\text{O}^{18}\text{O}$ can be searched from the ground because the species is not homonuclear and therefore, in contrast to $^{16}\text{O}_2$, both even and odd rotational quantum numbers N are allowed, giving permitted transitions between levels which do not exist for $^{16}\text{O}_2$. These transitions occur at frequencies totally free of $^{16}\text{O}_2$ emission and are therefore unblocked by the atmosphere except in a narrow range (± 10 MHz) around the rest frequency of the line, which can usually be avoided as a consequence of the Fizeau-Doppler shift resulting from the Earth’s orbital velocity around the Sun. The line predicted to be the strongest in the interstellar medium is the $\text{N}_j: 2_1 \rightarrow 0_1$ at 234 GHz (Maréchal et al. 1997b) that has been actively searched for from 1985 up to the end of the 1990s when satellites equipped with heterodyne receivers started to look directly for the main species $^{16}\text{O}_2$, 250 times more abundant, but still without success (see Goldsmith et al. 2011, for a review). The discovery of $^{16}\text{O}_2$ in ρ Oph (Larsson et al. 2007) triggered a last, still unsuccessful attempt to find $^{16}\text{O}^{18}\text{O}$ in that source (Liseau et al. 2010). Owing to the relatively rare LSR velocity of the O_2 emission ($V_{\text{LSR}} = 11.3 \text{ km s}^{-1}$) in this source, we thought that the emitting region could only be one of the small regions in that velocity range revealed by NH_3 (6,6) emission (Goddi et al. 2011), namely the MF4/MF5 region, which is the main region emitting in the 11 km s^{-1} range. However, we unexpectedly found a pair of vibrationally excited lines of ethyl cyanide ($\text{C}_2\text{H}_5\text{CN}$, $v_{13}=1/v_{21}=1$) at 233.945 GHz emitting a signal strong enough to completely mask the weak signal that we were expecting ($\sim 150 - 200 \text{ mK}$, Fig. 24) from our $^{16}\text{O}_2$ de-

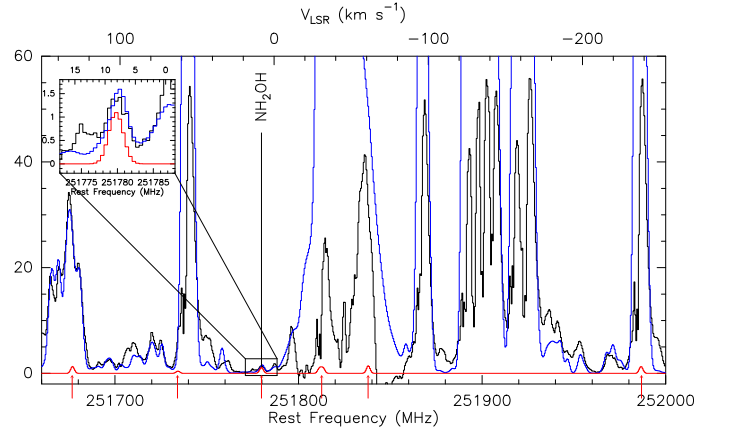


Fig. 25. Hydroxylamine (NH_2OH) line observation 0'9 west of the EGP. The six red arrows mark the positions of the nine NH_2OH lines (three lines are a combination of two transitions with very little or no spacing). The one possible detection is zoomed. Color-coding as in Fig. 4a.

tection (Goldsmith et al. 2011; Chen et al. 2014). Therefore, the expected presence of molecular oxygen in the Orion–KL region cannot be evaluated since the fitting of the ethyl cyanide line will never be secure enough to quantify any residual emission (this does not include the position farther to the north discussed in Chen et al. 2014 and Melnick & Kaufman 2015, which we postpone to a future paper).

3.7.2. Hydroxylamine NH_2OH

This species has never been identified in space, though it is predicted by chemical models (Pulliam et al. 2012; McGuire et al. 2015). In our bands, the only strong and likely observable lines are in the range 251.7 – 252.0 GHz ($J:5 \rightarrow 4$, $E_{\text{up}} = 36 - 164 \text{ K}$, spectroscopic data are provided by Tsunekawa 1972; Morino et al. 2000), a region which is densely packed with many strong methanol lines plus the $\text{SO } \text{N}_j:6_5 \rightarrow 5_4$ transition at 251.825 GHz, which all suffer from the absence of zero-spacing data, making their modeling impossible. Among the nine lines in this range, only one pair of lines is not blended with methanol, SO and ethyl cyanide strong emissions. These are the two $J_{K_a K_c}: 5_{33} \rightarrow 4_{32}$ and $J_{K_a K_c}: 5_{32} \rightarrow 4_{31}$ lines at 251.780 GHz with $E_{\text{up}} = 107.8 \text{ K}$. It is therefore impossible to search for this species, but we note that this line is possibly seen in one place in Orion–KL in order to focus some further searches at other frequencies at the same place. The spectrum shown in Fig. 25 was taken 0'9 west of the EGP, i.e., at $\text{RA}_{J2000} 05^{\text{h}}35^{\text{m}}14^{\text{s}}.44$, $\text{Dec}_{J2000} -05^{\circ}22'32''.8$.

3.7.3. Other species

We have searched without success for a number of species known in the interstellar medium but not yet identified in Orion, including propadienone ($\text{C}_3\text{H}_2\text{O}$), thiocyanic acid, (HSCN), isothiocyanic acid HNCS , cyanomethylene (HCCN), ketenyl (HCCO), cyanoamidogen (HNCN), cyanic acid (HOCN), cyanoformaldehyde HCOCN , protonated carbon dioxide (HOCO^+), hydroperoxyl (HO_2), cyclopropanediylidenyl ($\text{c-C}_3\text{H}$), propadienylidene ($\text{l-C}_3\text{H}_2$), cyclopropenone $\text{c-C}_3\text{H}_2\text{O}$, cyanopropyne ($\text{CH}_3\text{C}_3\text{N}$), N-protonated isocyanic acid (H_2NCO^+), methylene amidogen (H_2CN), methyl peroxide (CH_3OOH), deuterated diazenylium (N_2D^+), aminoacetonitrile ($\text{H}_2\text{NCH}_2\text{CN}$), and protonated cyanoacetylene (HC_3NH^+).

It is remarkable that despite the large abundance of isocyanic acid (HNCO) and of cyanoacetylene (HC_3N), their protonated forms are not detected, though for the former we have only one line that falls within our survey and it is often blended.

3.7.4. Extended emission

A few species have not been detected in our survey, while their detection seems firmly established in previous studies carried out with single dishes (Johansson et al. 1984; Madden et al. 1989; Turner 1991; Tercero et al. 2010). We believe that their non-detection is due to their extended, smoothly distributed emission.

This is the case of cyclopropenylidene ($\text{c-C}_3\text{H}_2$) reported by Madden et al. (1989) and Turner (1991). Turner (1991) explains that this species is emitted from a cold region that is not coming from Orion-KL but from an extended region surrounding it.

We do not detect thioxoethenylidene (CCS). Turner (1991) reports a fit with $T_{\text{rot}} = 19$ K. Though he does not comment on this result, it is possible to think that this low temperature argues again for extended emission, consistent with our non-detection. However Tercero et al. (2011) report the detection of both C_2S and thioxopropadienylidene (C_3S) with the IRAM 30 m as coming from the hot core. These cases should be resolved once existing single-dish data (zero-spacing) are added to our ALMA data.

Cyanobutadiyne (HC_5N) is reported by Johansson et al. (1984), Turner (1991), and Esplugues et al. (2013). Johansson et al. (1984) mentions that its emission is extended since they found weaker emission with their smaller beam, compared to what was found in earlier investigations. If extended, it might explain why lines of HC_5N were not detected in our survey, but the analysis of Esplugues et al. (2013) pin-points the emission to the outer hot core (though the position is not precisely defined in the paper) and to the CR. The column density of HC_5N for the CR fit ($3 \times 10^{12} \text{ cm}^{-2}$) is too low for this species to emit a detectable line in our data, while the column density for the HC fit ($7 \times 10^{13} \text{ cm}^{-2}$) is compatible with an emitted line of HC_5N for only one out of our six unblended HC_5N lines present in our survey (but not as large as 10 km s^{-1}). Its non-detection for the other lines is compatible with a column density seven times lower at the $\sim 3\sigma$ level.

3.7.5. Out of band species

Our survey was not continuous in frequency, and so a number of interesting species between 215 and 252 GHz were not observed. The interested reader is referred to the SV0 data to retrieve them: iminomethylum (HCNH^+), propyne (CH_3CCH), carbonyl sulfide isotopologues (OC^{33}S , OC^{34}S), ethynyl (CCH) and its ^{13}C substituted isotopologues (but CCD is observed though not detected), propynylidyne ($\text{l-C}_3\text{H}$), deuterated formyl (DCO^+), deuterated isocyanide (DNC), phosphorus nitride (PN), nitrogen sulfide (NS), the other ^{13}C substituted methyl cyanide isotopologue ($^{13}\text{CH}_3\text{CN}$), and fulminic acid (HCNO). Some species were present only in blends with stronger lines like the ^{13}C substituted thioformyl (H^{13}CS^+) cation.

4. Discussion: Velocity structure of the source

The velocity structure of Orion-KL is complex. The $\text{NH}_3(6,6)$ velocity map of Goddi et al. (2011) reveals (as do other studies) many velocity components, and in our survey some species have complex structure with numerous velocity components ranging

from -15 to 25 km s^{-1} , that are emitted from both the extended region and from the compact core. However, because of the lack of short spacings, there is some confusion regarding the velocity structure for the molecules with extended emission. Therefore, we focus on the emission from molecules that arise only from the small dense and hot components of the region where the lack of short spacings should not be a problem. Even these components show a complex velocity (Sect. 4.1). We also show that some velocity components on the same line of sight can be ordered (Sect. 4.3) and that the 500-year-old explosion could have an impact on the region around it that is observable in the line profiles (Sect. 4.4).

4.1. Kinematic complexity

The velocity structure of the region is extremely complex. Depending on the species, spectra toward different sources show up to four distinct components, sometimes with different species agreeing in velocity, and sometimes differing. This is obviously true for species like CO, SO, SO_2 , H_2CO , SiO, which have emission associated with each of the ten sources, but which also have emission on larger scales and part of this emission can be lost due to the interferometer filtering of extended emission. The net effect is that this can produce velocity components that are not real. We will not address these molecules further, but will address them later when we have added the zero-spacing data. This complex velocity structure is also present in molecules whose emission is limited to the hot spots; for example, vinyl and ethyl cyanides show the largest number of velocity components often not in coincidence with O-COMs like methanol and methyl formate. Figure 26 presents the line shape of three species (methanol, vinyl and ethyl cyanides) for all ten sources. The velocity components introduced in the model are traced by the vertical dashed lines. A few of them are introduced solely to reproduce the velocity wings, although we did not always undertake fitting these wings in detail (for example the wings of the cyanide species towards IRc7 and IRc21). A typical case is the CR/MF1 spot which needs two velocity components to fit the methanol line (and all the O-COMs) and four velocity components to fit the ethyl cyanide lines. The main velocity component goes from 0 to 11.2 km s^{-1} , with still important components beyond (down to -7 or up to $+19 \text{ km s}^{-1}$). The main cyanide velocity component sometimes has no corresponding emission in methanol (MF2, MF12, EGP). A first moment map of the emission of these species, like the $\text{NH}_3(6,6)$ map invoked earlier, would not render the complexity of this situation for sources like IRc7, MF2, the EGP, etc. Instead, we have produced a map where we indicate numerically the velocity of the various components (Fig. 27). Even these velocities are only indicative of a few species. The only relatively simple cases are IRc21 with a single component (but a strong blue wing) and the HC with two velocity components, one at 4.3 km s^{-1} at which all the cyanides emit, and a second one between 5.4 and 5.8 km s^{-1} that corresponds to the O-COMs. There are a few aberrant cases such as ethanol ($\text{C}_2\text{H}_5\text{OH}$) at $\sim 5 \text{ km s}^{-1}$, doubly deuterated formaldehyde (D_2CO) at 6.4 km s^{-1} , and vibrationally excited cyanoacetylene (HC_3N) $v_7 = 1$ components at -5.7 and 15.7 km s^{-1} and $v_7 = 2$ at -5.5 km s^{-1} in addition to the standard 4.3 km s^{-1} component. To make this picture consistent, a strongly perturbing event is required. We suggest that the kinematic structure of the molecules in this region is linked to the explosion which occurred 500 years ago (Pagani et al. in prep), an idea also proposed by Zapata et al. (2011).

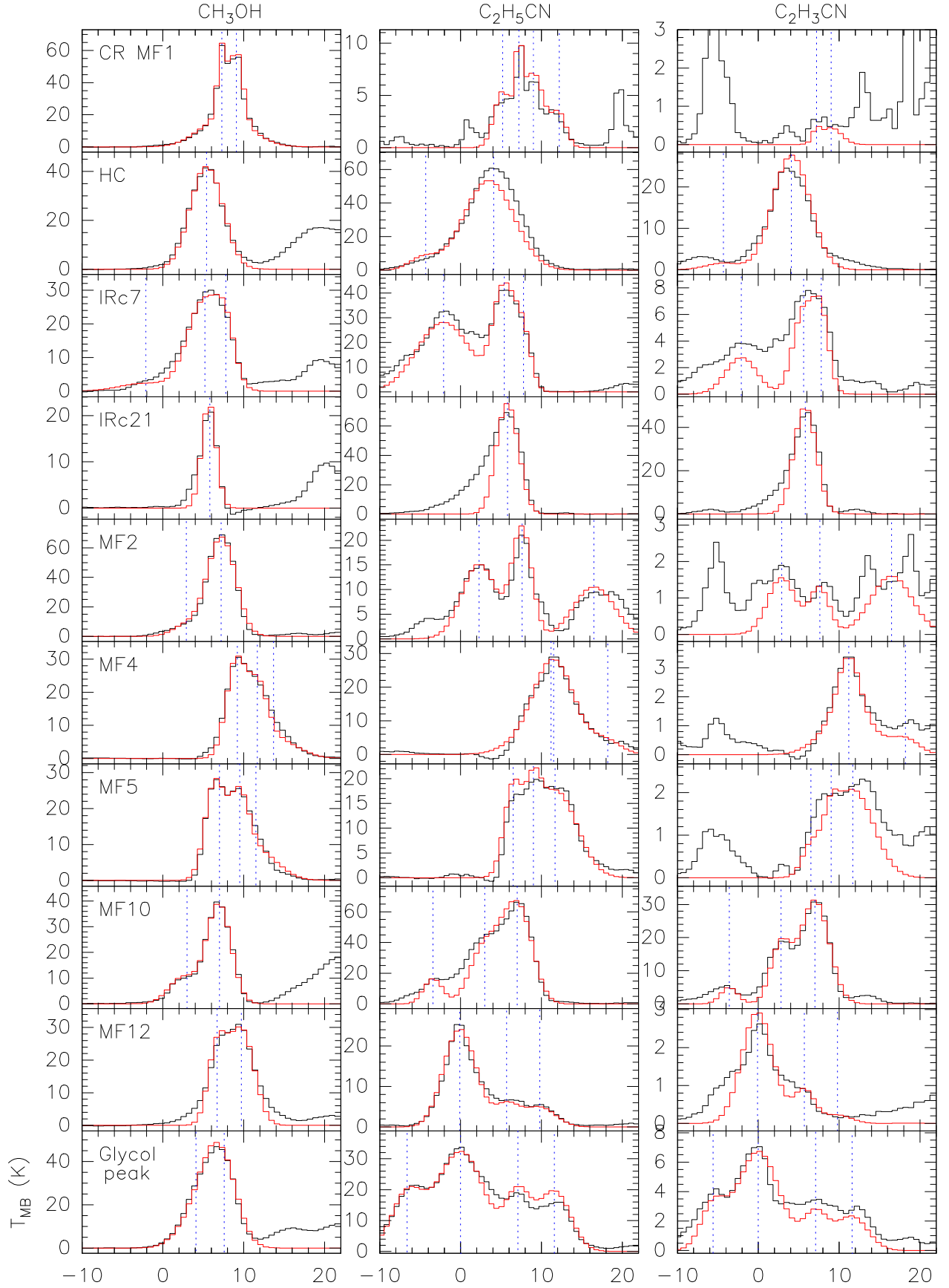


Fig. 26. Methanol (CH_3OH), vinyl cyanide ($\text{C}_2\text{H}_3\text{CN}$), and ethyl cyanide ($\text{C}_2\text{H}_5\text{CN}$) line profiles for the ten sources (see Fig. 1). The black line traces the data and the red line the LTE fit. The vertical dashed lines represent the velocity components introduced in the fit to match the observations.

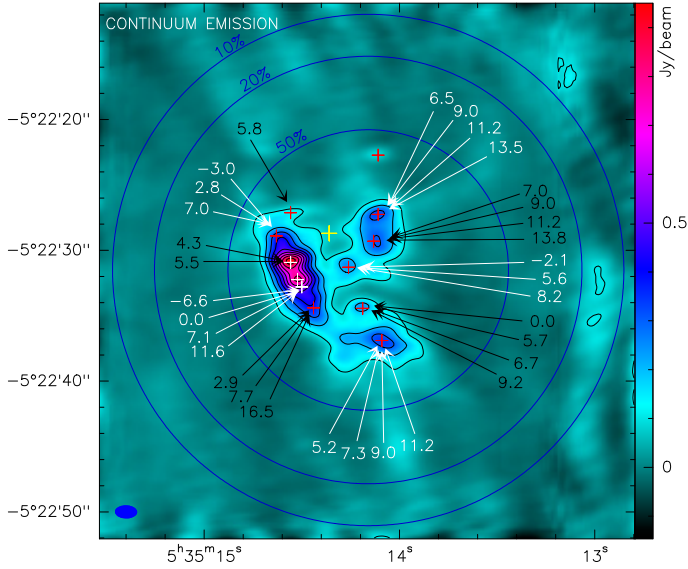


Fig. 27. Velocities of the main components towards the ten sources in our study superimposed on a copy of Fig. 1. The alternating white and black arrows and figures have no meaning and are only used to separate more clearly the list of velocities at each spot.

4.2. Chemical complexity

We also find differences between methanol and methyl formate, which are supposed to be chemically linked. The most striking case is towards MF4 (Fig. 28) where for any methanol line energy level, the line shape differs notably from the methyl formate line taken as a reference. This is therefore not an excitation effect or an extended emission loss for methanol. The coincidence of the two species is therefore not systematic and this different shape reflects an ongoing chemical evolution which deserves proper attention once the zero-spacing data is added. Similarly, Tercero et al. (2015) mention a different peak position for $^{13}\text{CH}_3\text{OH}$ and methyl formate along the ridge centered on the HC peak which they also interpret as ongoing transformation of methanol to methyl formate.

This complexity makes the single-dish telescope searches of weak lines difficult because of the mixing of many velocity components for each species. Even with ALMA resolving the sources and separating the components, great care must be taken to analyze the lines and correctly account for all components.

Another consequence of this complexity is the difficulty in deriving abundances. The total column density is derived from the dust emission (or the CO emission if it is possible to securely separate the local emission from the general emission) which cannot be split between the different velocity components. It seems therefore difficult to derive abundances per velocity component and attention should be paid to this problem when addressing the chemical evolution of the region.

4.3. Line of sight structure

In the band 6 setup, we observed the methyl cyanide (CH_3CN) ladder from $J_K: 12_3 \rightarrow 11_3$ (220.709 GHz) up to $J_K: 12_{11} \rightarrow 11_{11}$ (220.235 GHz, Fig. A.1f). The first transition is highly optically thick and when several velocity components are present on the same line of sight, the combination of their emission and absorption can change the observed profile if they are close enough in velocity to interact significantly. Though this low upper energy level transition is probably extended and some flux is missing,

Table 3. Order of velocity components along the line of sight

Source	Front (km s^{-1})	Middle (km s^{-1})	Back (km s^{-1})
MF4	8.7	11.2	14.2
MF5	6.2	9	11
MF10	7	3	(-3) ^a

Notes. ^(a) This velocity component is too distant to interfere with the others and to be definitively located along the line of sight.

we identify such an effect towards three sources, MF4, MF5 and MF10, for which we can try to match the profile by combining the velocity components in different sequences. Figure 29 shows the fit of methyl cyanide towards MF5. Unlike for all the other species, we use a non-LTE radiative transfer code (RADEX, van der Tak et al. 2007) to compute the line intensity since the structure of the symmetric top allows us to scan a wide range of energy levels for the same J level at nearby frequencies. The collisional coefficients are taken from Green (1986). The model includes three velocity components to match most of the line (we ignored the linewing), at 6.2, 9, and 11 km s^{-1} , similar to the velocity components we found for the other species, but slightly closer to the velocities of the O-COMs than to those of vinyl and ethyl cyanide (differences of a few tenths of km s^{-1}). While we manage to find a solution for the $K = 4 - 6$ transitions, the modeled $K = 3$ transition is always stronger than the observed line, most probably due to the loss of extended emission in the observations (Fig. 29, upper panel). If we rescale the spectrum to fit the observations for the $K = 3$ transition, we find that out of the six possible combinations, only one solution fits the observed profile (Fig. 29, lower panel). Two solutions are not shown because they give identical results to two others: when the central velocity component is in front or behind the two extreme velocity components, permuting the two extreme velocity components which do not mutually interfere makes no difference. With the supposition that the missing zero-spacing data would not change the line shape, we have ordered the velocity components of the three sources (MF4, MF5, MF10). Table 3 presents the results. For MF4 and MF5, the redshifted components are behind and the blueshifted components are in front, which indicates an expansion of the cloudlets, i.e. the cloudlets are receding at increasing velocities with increasing distance while for MF10, the reverse situation applies and the two components at positive velocity are moving towards each other (the third component at negative velocity does not interact and cannot be positioned).

4.4. Impact of the explosion on the cores

Figure 1 shows the position (yellow cross) where the 500-year-old explosion most probably took place (Gómez et al. 2005; Zapata et al. 2009). It is situated in the center of a belt of emission passing through IRC21, IRC2/MF10, HC, IRC7, IRC20/MF4 and IRC6/MF5. A number of works have revealed the H_2 and the ^{12}CO expansion linked to this explosion (e.g. Allen & Burton 1993; Zapata et al. 2009; Nissen et al. 2012; Youngblood et al. 2016) but it seems that the interaction of this event with the surrounding cores has only been considered by Zapata et al. (2011). While we will address in greater details the link we see between the explosion and a number of species peculiar velocity distributions (including nitrogen monoxide, isocyanic acid, vinyl and ethyl cyanide) in a forthcoming paper (Pagani et al. in prep), we want to mention a number of facts of interest here.

We already mentioned the interesting formic acid (HCOOH) extended emission away from the explosion center in Sect. 3.6. We also note that the vibrationally excited lines of cyanoacetylene (HC_3N), but also those of other species (vinyl and ethyl cyanides, which will be presented in Pagani et al. in prep.) are following the belt mentioned above (Fig. 8). Figure 26 also shows prominent wings on the methanol emission lines (and other molecules) towards sources that lie closer to the explosion center. MF4 and MF5 on the west of the explosion center display red wings, while IRC21, IRC7, and MF10, which lie southeast of the explosion center, display blue wings. Overall, the velocity components of MF4 and MF5 are all above 6 km s^{-1} while low or even negative components are found on the eastern side. We suggest that these wings are tracing material being accelerated by the high velocity ($> 100 \text{ km s}^{-1}$) outflowing gas resulting from the explosion. This would indicate that MF4 and MF5 are located behind the explosion center (to explain the red wings and the 9 to 13 km s^{-1} velocity components) and that they are receding from it, away from us, while the HC long ridge (including sources from MF2 to MF10, and possibly IRC21) is in front of the explosion center, also moving away from it, but towards us (to explain the blue wings and the velocity components mostly between 0 and 6 km s^{-1}). The recession of all the molecular clumps in Orion–KL is possibly induced by the slow (15 km s^{-1}) bubble expansion, i.e., 7.5 km s^{-1} radial (Zapata et al. 2011), following the explosion, but this requires further investigation. The whole structure, including the discussion of the Compact Ridge position (Sect. 4.5), is depicted in a sketch (Fig. 30), though we currently have no information to position in detail those parts of the region that are in front of the explosion center with respect to each other, nor of the MF4 and MF5 substructures in between them and relative to the other groups.

4.5. Compact Ridge

The Compact Ridge (CR/MF1) is very different from all the other cores. Ethyl cyanide ($\text{C}_2\text{H}_5\text{CN}$) emission is weak and vinyl cyanide ($\text{C}_2\text{H}_3\text{CN}$) is absent. It is an extremely quiescent emitter with lines close to 1 km s^{-1} width, sometimes barely resolved (or not at all) with our backend setup ($\sim 0.6 \text{ km s}^{-1}$), as illustrated by the tentative Gaussian fit of three methyl formate (CH_3OCHO) components towards this source (Fig. 31). The narrow components have line widths in the range $0.9 - 1.4 \text{ km s}^{-1}$. The line wings are symmetrical. Only the two lowest vibrational energy levels of cyanoacetylene are populated. It seems therefore that this core has escaped (at least until the present time) the influence of the explosive event. Since the much smaller IRC4/MF12 clump just above CR/MF1 is similar to the ring fragments in terms of line shape, asymmetric wings, and excitation, and is therefore being affected by the explosive event, it seems more probable that the CR is far enough away to have not yet been reached. Examining the maximum extent of the ^{12}CO filaments (Zapata et al. 2009) ($20 - 35''$ southward, up to $50''$ northward), we can consider that CR/MF1 has to be at least at such a distance to have escaped the high velocity gas until now. Orion’s distance of 388 pc combined with the angular offset of $50''$ corresponds to $20,000 \text{ au}$. Since CR/MF1 is only $10''$ south of the explosion center, it must be in front of or behind the explosion center by at least $10,000 \text{ au}$ (for the typical $25''$ CO bullet distance southward) and more probably by $20,000 \text{ au}$, and is therefore only loosely related to the other Orion–KL cores. Wang et al. (2010) also indicate the existence of a cavity between the HC and the CR from their analysis of high rotation levels of methyl cyanide.

5. Conclusions

We have observed 16 GHz of bandpass in the 1.3 mm window towards Orion–KL during the ALMA Cycle 2. The angular and resulting spatial resolution are sufficient to separate all the components of the region; the spectral resolution that we have employed is also sufficient except towards the compact ridge, which presents narrow lines close to 1 km s^{-1} only. Numerous interesting results already emerge from this first study, demonstrating the need to analyze all the dense structures as well as all the main lines in parallel to obtain a consistent model of this complex region. A wealth of information remains to be extracted from these data; in addition to possibly revealing new molecules, this new information will also help to better understand the structure and evolution of this source.

Acknowledgements. We thank an anonymous referee for the careful reading of the document; we enjoyed our discussion, which helped to improve the presentation of our results. We thank the IRAM ARC center for their hospitality and coaching for the ALMA data reduction process, in particular Gaëlle Dumas and Edwige Chapillon, ESO for the financial support during the visit to the ARC (MARCUs funding) and Crystal Brogan for her help and suggestions throughout the preparation and data reduction processes. This work made use of the SIMBAD resource offered by CDS Strasbourg, France, of the CDMS and JPL molecular line databases offered by the Köln University and by NASA respectively. We thank Arnaud Belloche and Holger Müller for their great help in the identification of the excited modes of cyanide species and other advice that they endlessly provided. L.P. thanks the CNRS for the permanent funding of his position, without which this work could not have been performed. A short term funding would never have permitted this type of work. C.F. acknowledges funding from the French space agency CNES, and support from the Italian Ministry of Education, Universities and Research, project SIR (RBSI14ZRHR). This work was carried out in part at the Jet Propulsion Laboratory, which is operated for NASA by the California Institute of Technology. E.A.B. acknowledges support from the National Science Foundation grant AST-1514670.

References

- Allen, D. A. & Burton, M. G. 1993, *Nature*, 363, 54
- Amano, T. & Tanaka, K. 1986, *Journal of Molecular Spectroscopy*, 116, 112
- Barros, J., Appadoo, D., McNaughton, D., et al. 2015, *Journal of Molecular Spectroscopy*, 307, 44
- Belloche, A., Garrod, R. T., Müller, H. S. P., & Menten, K. M. 2014, *Science*, 345, 1584
- Belloche, A., Müller, H. S. P., Garrod, R. T., & Menten, K. M. 2016, *A&A*, 587, A91
- Belloche, A., Müller, H. S. P., Menten, K. M., Schilke, P., & Comito, C. 2013, *A&A*, 559, A47
- Bergin, E. A., Phillips, T. G., Comito, C., et al. 2010, *A&A*, 521, L20+
- Bergman, P., Parise, B., Liseau, R., et al. 2011, *A&A*, 531, L8
- Bizzocchi, L. & Degli Esposti, C. 2004, *ApJ*, 614, 518
- Blake, G. A., Sutton, E. C., Masson, C. R., & Phillips, T. G. 1986, *ApJS*, 60, 357
- Blake, G. A., Sutton, E. C., Masson, C. R., & Phillips, T. G. 1987, *Astrophysical Journal*, 315, 621
- Brouillet, N., Despois, D., Baudry, A., et al. 2013, *A&A*, 550, A46
- Brouillet, N., Despois, D., Lu, X. H., et al. 2015, *A&A*, 576, A129
- Butler, R. A. H., De Lucia, F. C., Petkie, D. T., et al. 2001, *ApJS*, 134, 319
- Cernicharo, J., Kisiel, Z., Tercero, B., et al. 2016, *A&A*, 587, L4
- Chen, J.-H., Goldsmith, P. F., Viti, S., et al. 2014, *ApJ*, 793, 111
- Crockett, N. R., Bergin, E. A., Neill, J. L., et al. 2014, *Astrophysical Journal*, 787, 112
- Daly, A. M., Bermúdez, C., Kolesníková, L., & Alonso, J. L. 2015, *ApJS*, 218, 30
- Daly, A. M., Bermúdez, C., López, A., et al. 2013, *Astrophysical Journal*, 768, 81
- de Vicente, P., Martín-Pintado, J., Neri, R., & Rodríguez-Franco, A. 2002, *ApJ*, 574, L163
- Demailon, J. & Dreizler, H. 1982, *Zeitschrift Naturforschung Teil A*, 37, 199
- Demailon, J., Maes, H., Van Eijck, B. P., Włodarczak, G., & Lasne, M. C. 1987, *Journal of Molecular Spectroscopy*, 125, 214
- Esplughes, G. B., Cernicharo, J., Viti, S., et al. 2013, *A&A*, 559, A51
- Favre, C., Despois, D., Brouillet, N., et al. 2011, *A&A*, 532, A32
- Favre, C., Wootten, H. A., Remijan, A. J., et al. 2011, *ApJ*, 739, L12
- Feng, S., Beuther, H., Henning, T., et al. 2015, *A&A*, 581, A71

- Fourikis, N., Takagi, K., & Morimoto, M. 1974, *ApJ*, 191, L139
- Friedel, D. N. & Snyder, L. E. 2008, *ApJ*, 672, 962
- Friedel, D. N. & Weaver, S. L. W. 2011, *Astrophysical Journal*, 742, 64
- Friedel, D. N. & Widicus Weaver, S. L. 2012, *ApJS*, 201, 17
- Garrod, R. T., Belloche, A., Müller, H. S. P., & Menten, K. M. 2017, *A&A*, 601, A48
- Goddi, C., Greenhill, L. J., Humphreys, E. M. L., Chandler, C. J., & Matthews, L. D. 2011, *ApJ*, 739, L13
- Goldsmith, P. F., Krotkov, R., Snell, R. L., Brown, R. D., & Godfrey, P. 1983, *ApJ*, 274, 184
- Goldsmith, P. F., Liseau, R., Bell, T. A., et al. 2011, *ApJ*, 737, 96
- Goldsmith, P. F., Melnick, G. J., Bergin, E. A., et al. 2000, *ApJ*, 539, L123
- Goldsmith, P. F., Snell, R. L., Deguchi, S., Krotkov, R., & Linke, R. A. 1982, *Astrophysical Journal*, 260, 147
- Goldsmith, P. F., Snell, R. L., Erickson, N. R., et al. 1985, *ApJ*, 289, 613
- Gómez, L., Rodríguez, L. F., Loinard, L., et al. 2005, *ApJ*, 635, 1166
- Green, S. 1986, *ApJ*, 309, 331
- Hardy, J. A., Cox, A. P., Fliege, E., & Dreizler, H. 1982, *Zeitschrift Naturforschung Teil A*, 37, 1035
- Hirota, T., Kim, M. K., & Honma, M. 2012, *ApJ*, 757, L1
- Irvine, W. M., Goldsmith, P. F., & Hjalmarsen, Å. 1987, in *IN: Interstellar processes; Proceedings of the Symposium, Five College Radio Astronomy Observatory*, Amherst, MA (Dordrecht: Springer Netherlands), 561–609
- Johansson, L. E. B., Andersson, C., Elder, J., et al. 1984, *Astronomy and Astrophysics (ISSN 0004-6361)*, 130, 227
- Johnson, D. R., Suenram, R. D., & Lafferty, W. J. 1976, *ApJ*, 208, 245
- Jørgensen, J. K., van der Wiel, M., Coutens, A., et al. 2016, *A&A*, 595, A117
- Kaifu, N., Morimoto, M., Nagane, K., et al. 1974, *ApJ*, 191, L135
- Kirby, C., Krot, H. W., & Walton, D. R. M. 1980, *Journal of Molecular Spectroscopy*, 83, 261
- Kounkel, M., Hartmann, L., Loinard, L., et al. 2017, *ApJ*, 834, 1
- Larsson, B., Liseau, R., Pagani, L., et al. 2007, *A&A*, 466, 999
- Lerate, M. R., Yates, J., Viti, S., et al. 2008, *MNRAS*, 387, 1660
- Linnartz, H., Motylewski, T., Vazert, O., et al. 1999, *Journal of Molecular Spectroscopy*, 197, 1
- Liseau, R., Goldsmith, P. F., Larsson, B., et al. 2012, *A&A*, 541, A73
- Liseau, R. & Larsson, B. 2015, *A&A*, 583, A53
- Liseau, R., Larsson, B., Bergman, P., et al. 2010, *A&A*, 510, A98
- Liu, S.-Y., Girart, J. M., Remijan, A., & Snyder, L. E. 2002, *ApJ*, 576, 255
- López, A., Tercero, B., Kisiel, Z., et al. 2014, *A&A*, 572, A44
- Madden, S. C., Irvine, W. M., Swade, D. A., Matthews, H. E., & Friberg, P. 1989, *AJ*, 97, 1403
- Mangum, J. G., Wootten, A., Wadiak, E. J., & Loren, R. B. 1990, *Astrophysical Journal*, 348, 542
- Maréchal, P., Pagani, L., Langer, W. D., & Castets, A. 1997a, *A&A*, 318, 252
- Maréchal, P., Viala, Y. P., & Pagani, L. 1997b, *A&A*, 328, 617
- Maret, S., Hily-Blant, P., Pety, J., Bardeau, S., & Reynier, E. 2011, *A&A*, 526, A47
- McCarthy, M. C., Levine, E. S., Apponi, A. J., & Thaddeus, P. 2000, *Journal of Molecular Spectroscopy*, 203, 75
- McGuire, B. A., Carroll, P. B., Dollhopf, N. M., et al. 2015, *ApJ*, 812, 76
- McKellar, A. R. W., Watson, J. K. G., Chu, L.-K., & Lee, Y.-P. 2008, *Journal of Molecular Spectroscopy*, 252, 230
- McMullin, J. P., Waters, B., Schiebel, D., Young, W., & Golap, K. 2007, in *Astronomical Society of the Pacific Conference Series*, Vol. 376, *Astronomical Data Analysis Software and Systems XVI*, ed. R. A. Shaw, F. Hill, & D. J. Bell, 127
- Melnick, G. J. & Kaufman, M. J. 2015, *ApJ*, 806, 1
- Menten, K. M., Reid, M. J., Forbrich, J., & Brunthaler, A. 2007, *A&A*, 474, 515
- Morino, I., Yamada, K. M. T., Klein, H., et al. 2000, *Journal of Molecular Structure*, 517, 367
- Moruzzi, G., Jabs, W., Winnewisser, B. P., & Winnewisser, M. 1998, *Journal of Molecular Spectroscopy*, 190, 353
- Motiyenko, R. A., Ilyushin, V. V., Drouin, B. J., Yu, S., & Margulès, L. 2014, *A&A*, 563, A137
- Müller, H. S. P., Coutens, A., Walters, A., Grabow, J.-U., & Schlemmer, S. 2011, *Journal of Molecular Spectroscopy*, 267, 100
- Müller, H. S. P., Schlöder, F., Stutzki, J., & Winnewisser, G. 2005, *Journal of Molecular Structure*, 742, 215
- Müller, H. S. P., Thorwirth, S., Roth, D. A., & Winnewisser, G. 2001, *A&A*, 370, L49
- Nissen, H. D., Cunningham, N. J., Gustafsson, M., et al. 2012, *A&A*, 540, A119
- Pagani, L., Olofsson, A. O. H., Bergman, P., et al. 2003, *A&A*, 402, L77
- Pardo, J. R. & Cernicharo, J. 2007, *ApJ*, 654, 978
- Peng, T.-C., Despois, D., Brouillet, N., et al. 2013, *A&A*, 554, A78
- Peng, T. C., Despois, D., Brouillet, N., Parise, B., & Baudry, A. 2012, *A&A*, 543, A152
- Peng, Y., Qin, S.-L., Schilke, P., et al. 2017, *ApJ*, 837, 49
- Pickett, H. M., Poynter, R. L., Cohen, E. A., et al. 1998, *J. Quant. Spec. Radiat. Transf.*, 60, 883
- Pulliam, R. L., McGuire, B. A., & Remijan, A. J. 2012, *ApJ*, 751, 1
- Rieke, G. H., Low, F. J., & Kleinmann, D. E. 1973, *ApJ*, 186, L7+
- Roberto, M., Beckwith, S. V. W., Panagia, N., et al. 2005, *AJ*, 129, 1534
- Rodríguez, L. F., Dzib, S. A., Loinard, L., et al. 2017, *ApJ*, 834, 1
- Rodríguez, L. F., Poveda, A., Lizano, S., & Allen, C. 2005, *Astrophysical Journal*, 627, L65
- Sandstrom, K. M., Peek, J. E. G., Bower, G. C., Bolatto, A. D., & Plambeck, R. L. 2007, *ApJ*, 667, 1161
- Shuping, R. Y., Morris, M., & Bally, J. M. 2004, *AJ*, 128, 363
- Sutton, E. C., Blake, G. A., Masson, C. R., & Phillips, T. G. 1985, *ApJS*, 58, 341
- Tercero, B., Cernicharo, J., López, A., et al. 2015, *A&A*, 582, L1
- Tercero, B., Cernicharo, J., Pardo, J. R., & Goicoechea, J. R. 2010, *A&A*, 517, A96
- Tercero, B., Vincent, L., Cernicharo, J., Viti, S., & Marcelino, N. 2011, *A&A*, 528, A26
- Thorwirth, S., Mueller, H. S. P., & Winnewisser, G. 2001, *Physical Chemistry Chemical Physics (Incorporating Faraday Transactions)*, 3, 1236
- Thorwirth, S., Müller, H. S. P., & Winnewisser, G. 2000, *Journal of Molecular Spectroscopy*, 204, 133
- Tsunekawa, S. 1972, *Journal of the Physical Society of Japan*, 33, 167
- Turner, B. E. 1991, *ApJS*, 76, 617
- van der Tak, F. F. S., Black, J. H., Schöier, F. L., Jansen, D. J., & van Dishoeck, E. F. 2007, *A&A*, 468, 627
- Vormann, K. & Dreizler, H. 1988, *Zeitschrift Naturforschung Teil A*, 43, 338
- Wang, K.-S., Kuan, Y.-J., Liu, S.-Y., & Charnley, S. B. 2010, *Astrophysical Journal*, 713, 1192
- Winnewisser, G. 1973, *Journal of Molecular Spectroscopy*, 46, 16
- Winnewisser, M., Winnewisser, B. P., Stein, M., et al. 2002, *Journal of Molecular Spectroscopy*, 216, 259
- Wlodarczyk, G., Martinache, L., Demaison, J., Marstokk, K.-M., & Møllendal, H. 1988, *Journal of Molecular Spectroscopy*, 127, 178
- Yamada, K. M. T. & Creswell, R. A. 1986, *Journal of Molecular Spectroscopy*, 116, 384
- Youngblood, A., Ginsburg, A., & Bally, J. M. 2016, *AJ*, 151, 1
- Zapata, L. A., Schmid-Burgk, J., Ho, P. T. P., Rodríguez, L. F., & Menten, K. M. 2009, *Astrophysical Journal*, 704, L45
- Zapata, L. A., Schmid-Burgk, J., & Menten, K. M. 2011, *A&A*, 529, A24

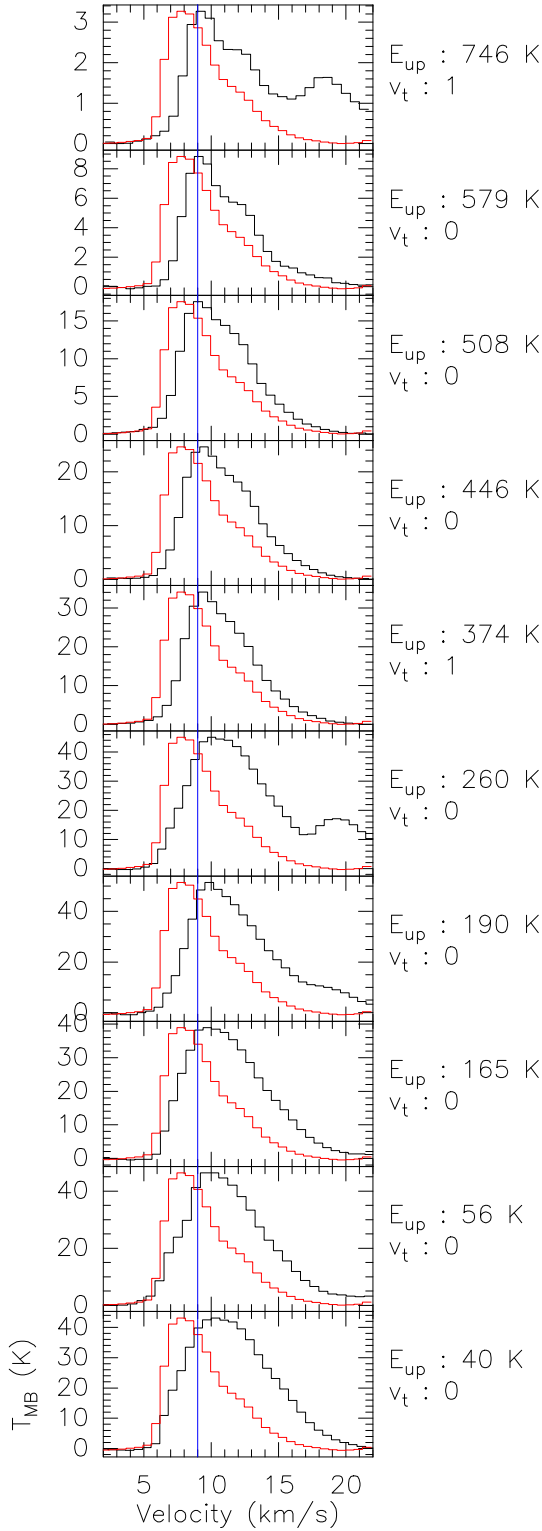


Fig. 28. Line shape difference between methanol (CH_3OH) and methyl formate (CH_3OCHO) towards MF4 for different transitions of methanol (in black; the upper state energy (K) and the torsional mode are indicated to the right) compared to the same methyl formate line (in red) for reference. The blue line marks the 9 km s^{-1} average velocity of the region.

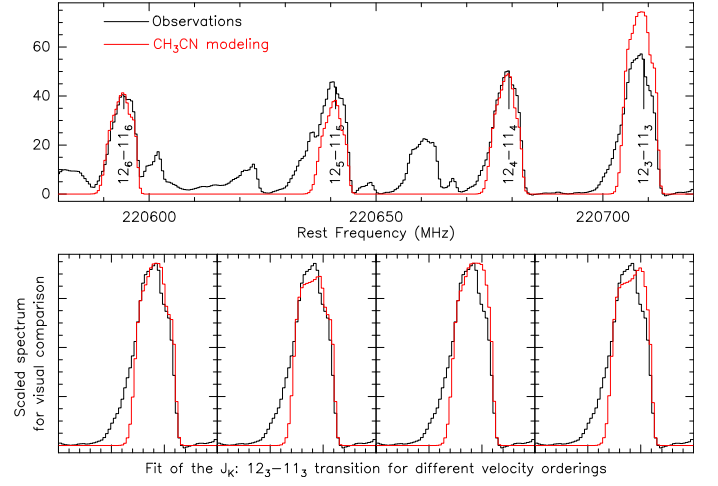


Fig. 29. Fit of CH_3CN K components of the $J:12 \rightarrow 11$ rotational transition towards MF5. **Upper panel:** Fit of four K ladder components. **Lower level:** Three velocity components ordered differently on the line of sight to fit the observed profile of the $K = 3$ transition (scaled to visually match the observations).

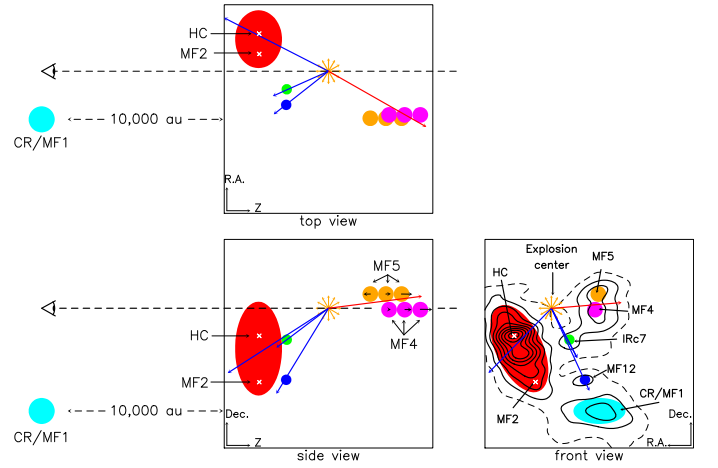


Fig. 30. Different components in the KL region following the discussion in Sects. 4.4 and 4.5. The front view shows the continuum contours from Fig. 1 employing simple elliptical shapes to indicate the different parts of the cloud. The red ellipse includes the HC ridge, encompassing IRc21, MF10, MF6, MF2, and the Glycol Peak. The explosion center is indicated by the set of orange arrows, and the velocity shifts of both the bulk of the gas and the line wings are shown in the corresponding color. The respective position of MF12 (dark blue), IRc7 (green) and the HC group along the Z-axis is not known and the arrangement shown is arbitrary. The only constraint is that MF4 (purple)/MF5 (orange) be behind the explosion center and the rest of the components be in front along the Z-axis. We have also not given any inclination or bent shape to the HC ridge along the Z-axis. The CR/MF1 (cyan) source is supposed to be at least 10,000 AU in front but could also be behind. MF4 and MF5 are split into three blobs with small velocity arrows of increasing length (and possibly approaching the observer for the first MF5 blob) to illustrate that the farther away from the explosion center, the higher is the source's velocity (see Table 3).

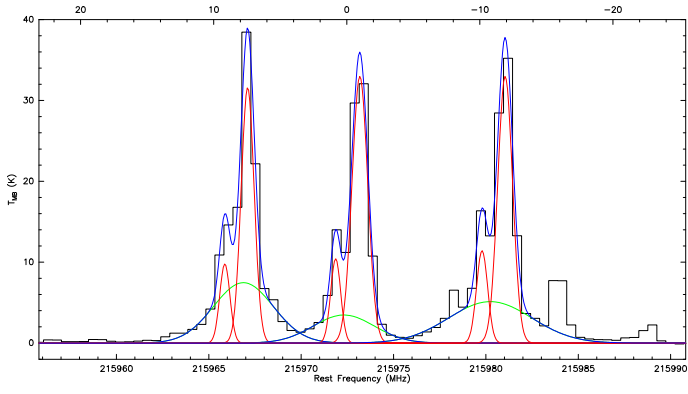


Fig. 31. Three methyl formate (CH₃OCHO) components observed towards CR/MF1. Data are in black; individual components: narrow are in red, wide are in green, sum of the components are in blue.

Appendix A: Complete set of data

We present here the full set of data towards the ten sources defined in Fig. 1 in full-scale mode and zoomed to 5 K to highlight the weaker lines. The data are presented band by band for all ten sources in parallel to allow direct comparison of the variations between the sources, first without any fit (Figs. A.1a – p and A.2a – p) and then including the combination of the fits to individual species (Figs. A.3a – p and A.4a – p).

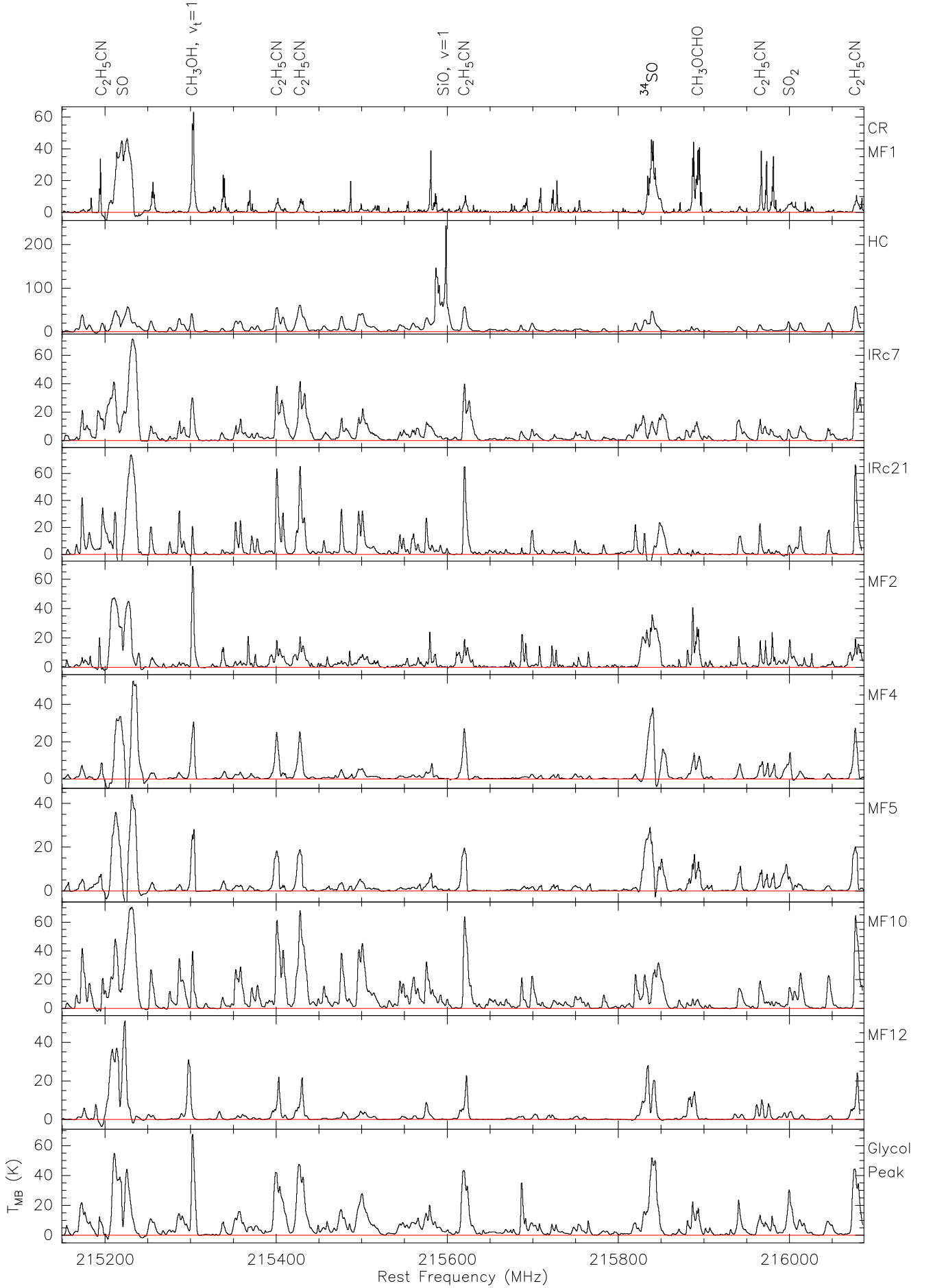


Fig. A.1a. Spectra from the band 1 setup for all ten sources. The strongest lines are identified at the top of the figure. The red line indicates the zero level. This figure is identical to Fig. 2 and is reproduced here for completeness of the Appendix.

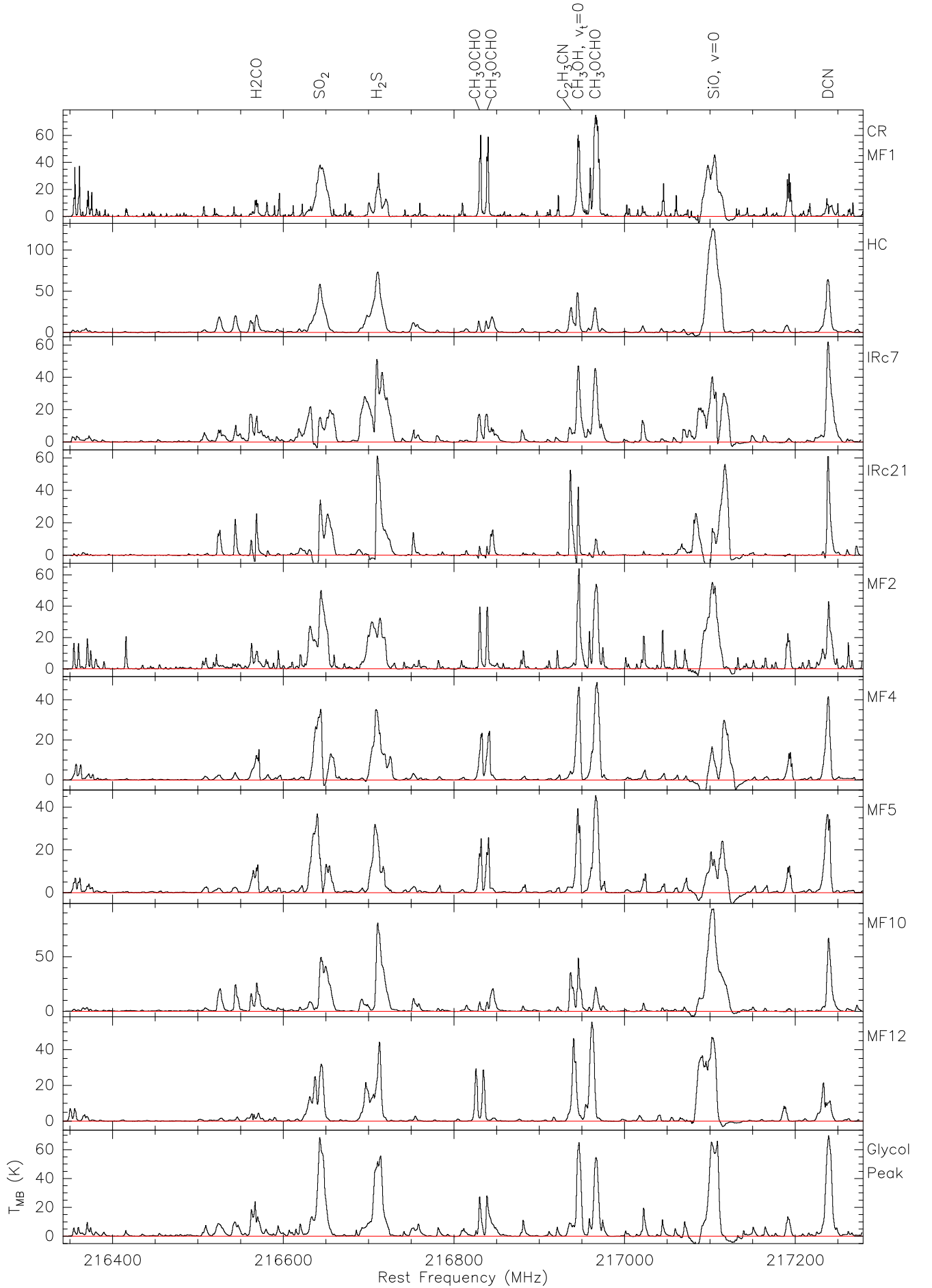


Fig. A.1b. Spectra from the band 2 setup for all ten sources.

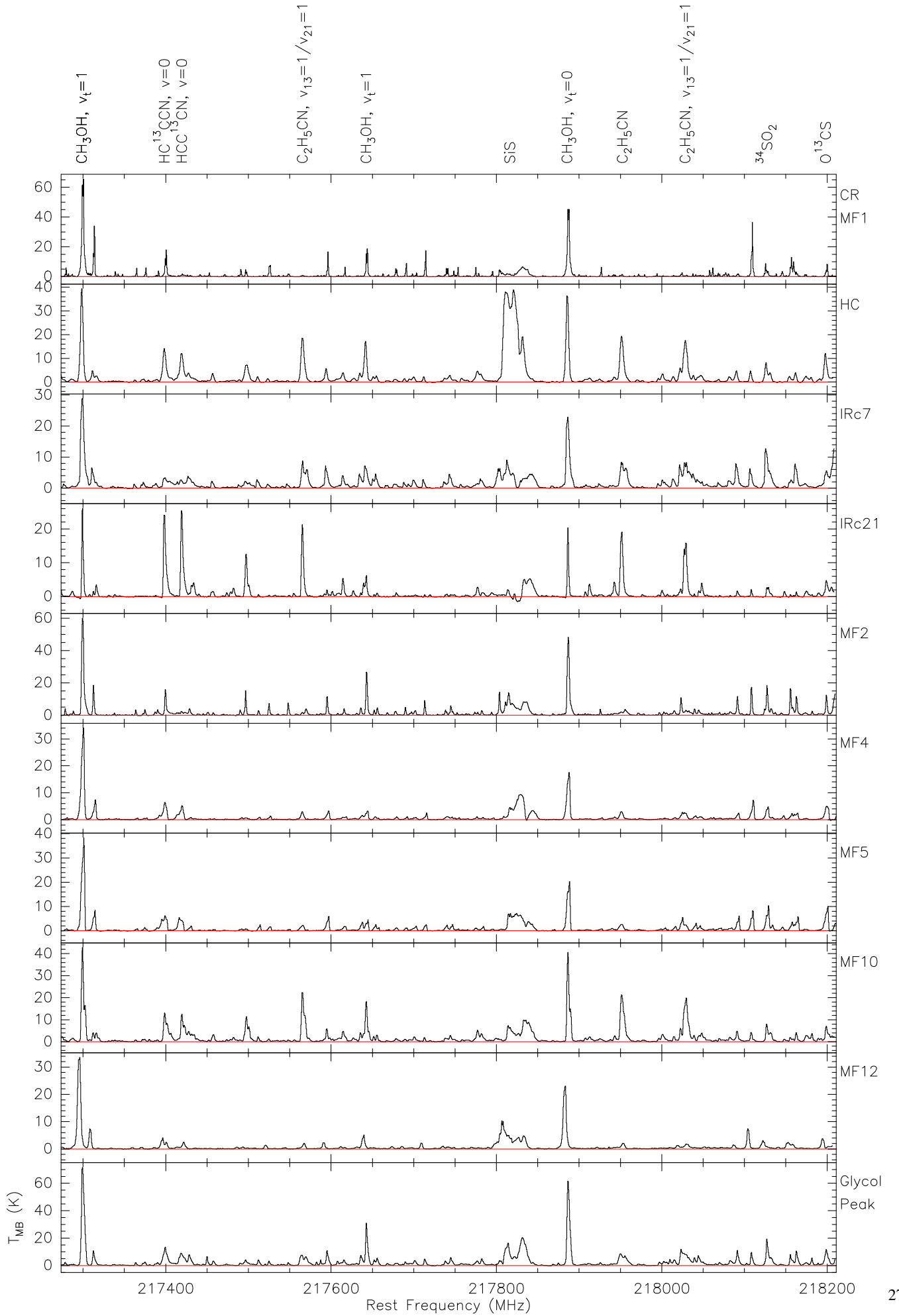


Fig. A.1c. Spectra from the band 3 setup for all ten sources.

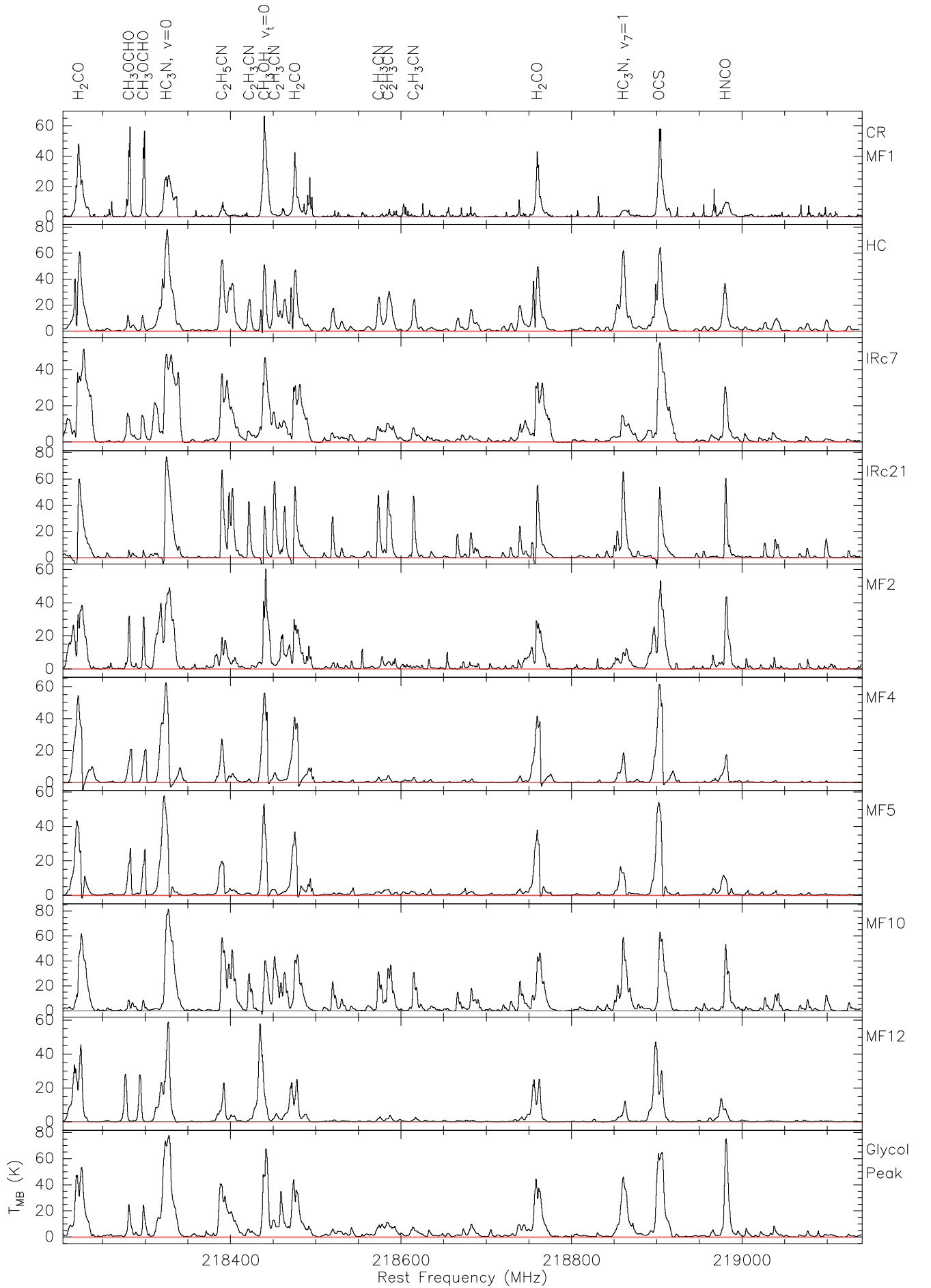


Fig. A.1d. Spectra from the band 4 setup for all ten sources.

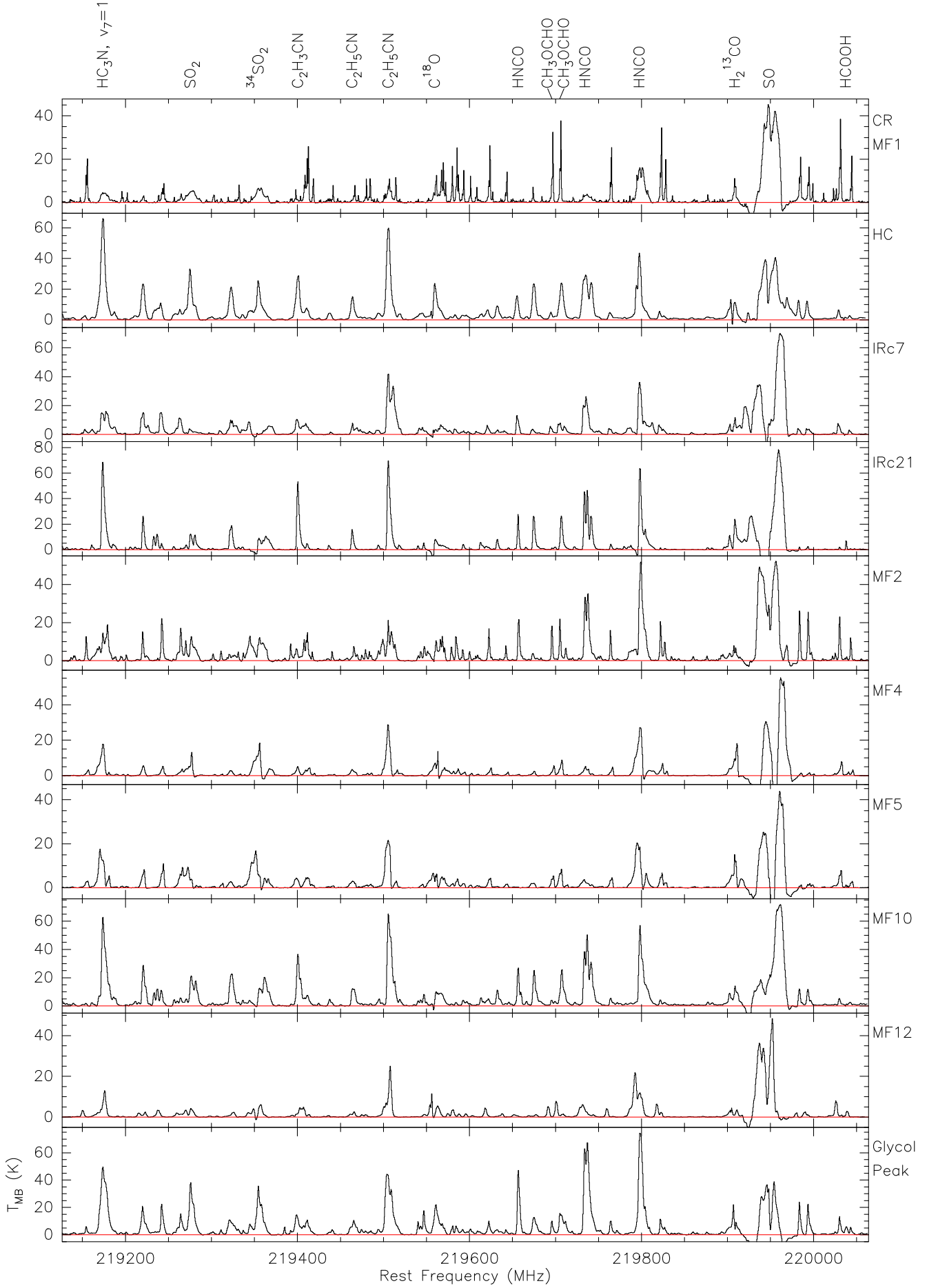


Fig. A.1e. Spectra from the band 5 setup for all ten sources. A ~ 250 MHz overlap with Fig A.1f is present, due to an incorrect setup.

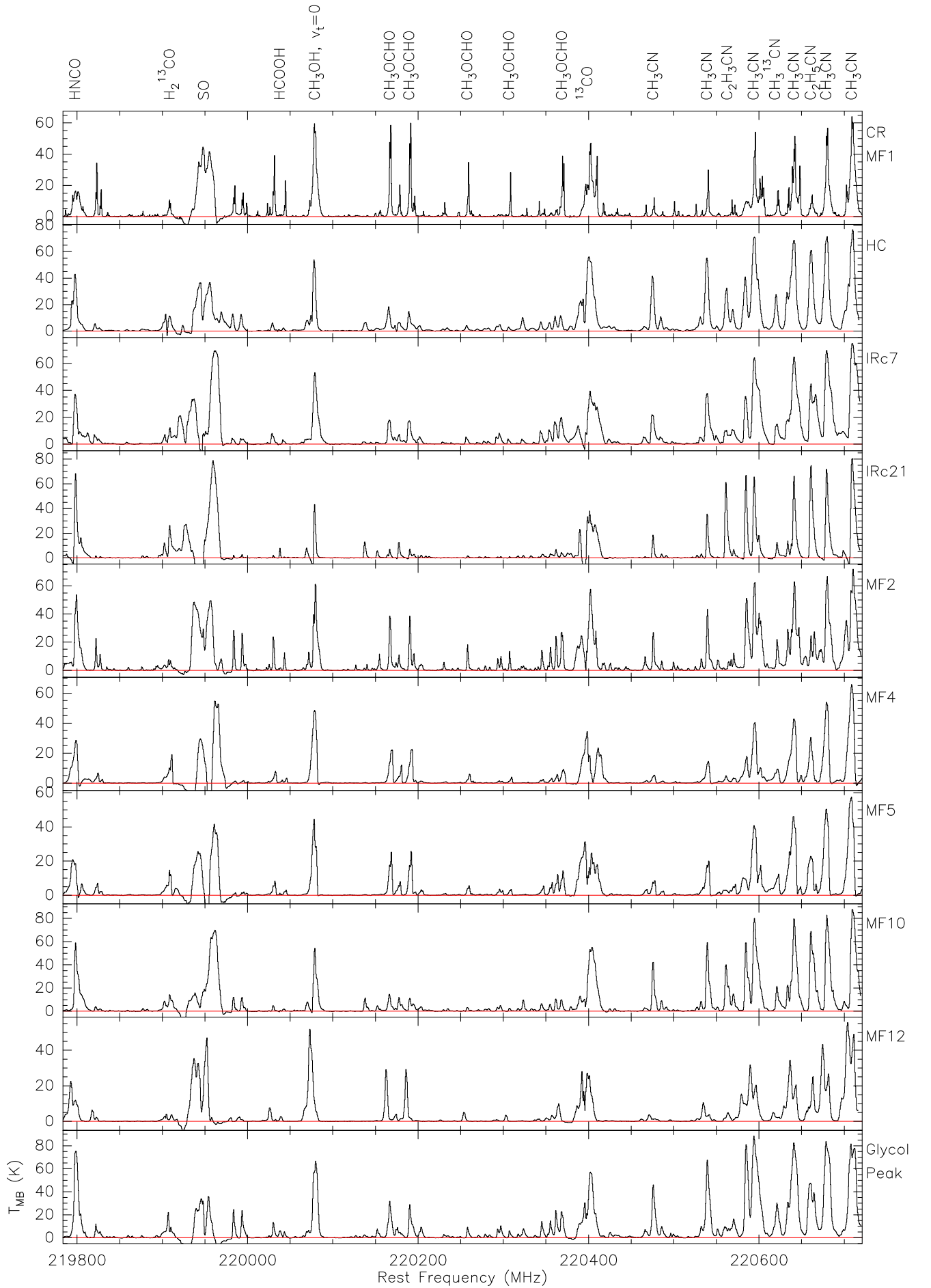


Fig. A.1f. Spectra from the band 6 setup for all ten sources.

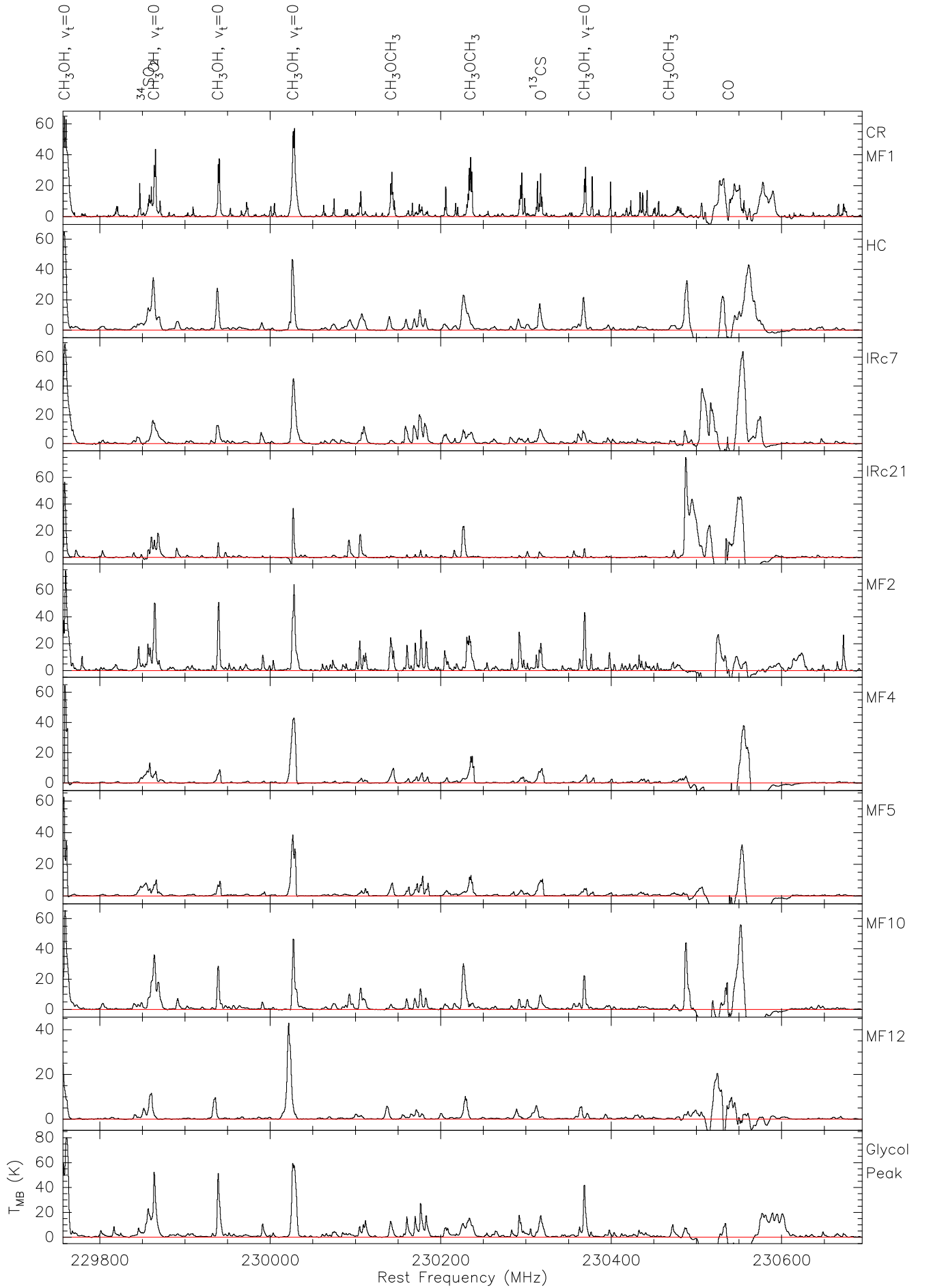


Fig. A.1g. Spectra from the band 7 setup for all ten sources.

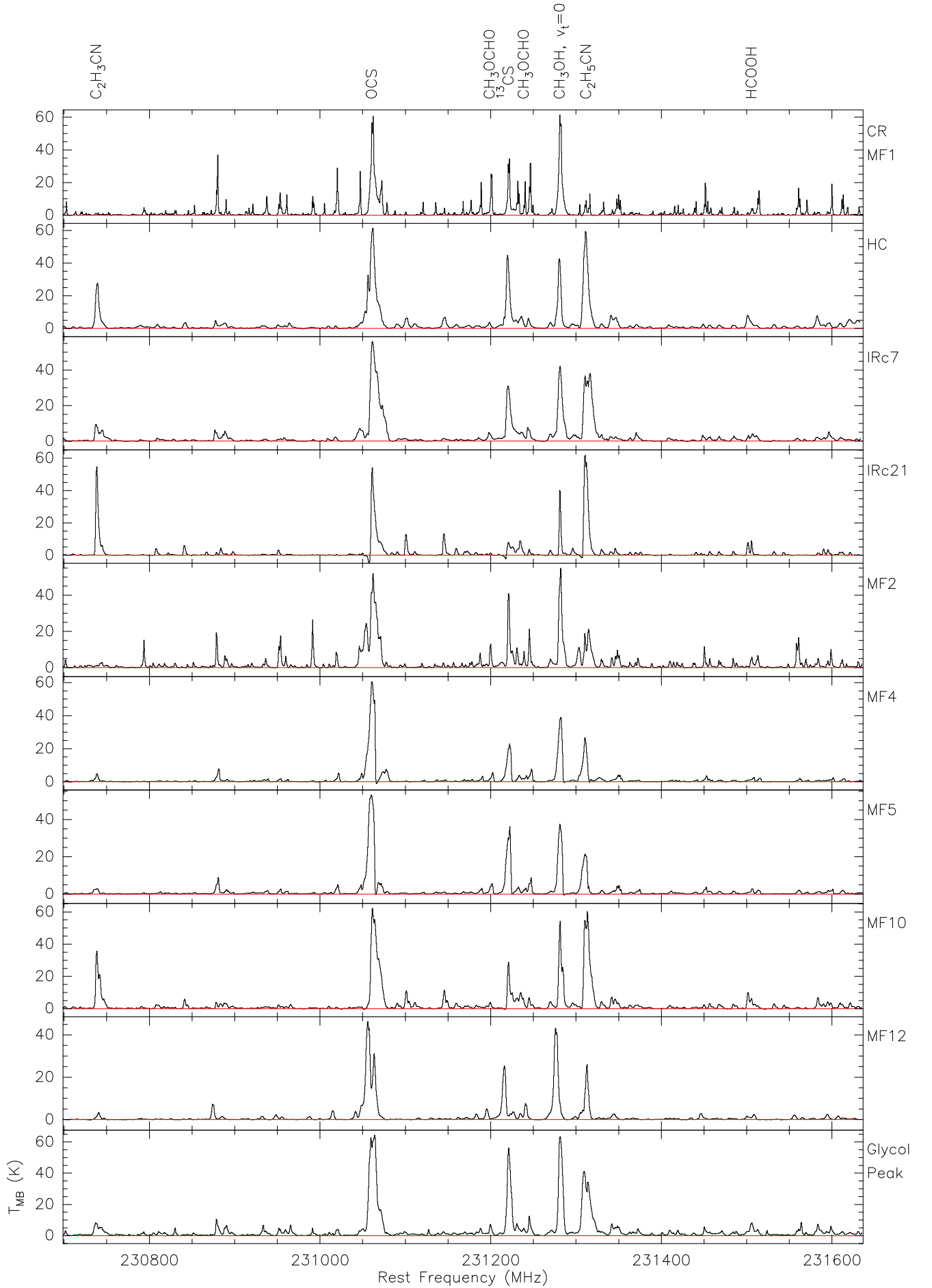


Fig. A.1h. Spectra from the band 8 setup for all ten sources.

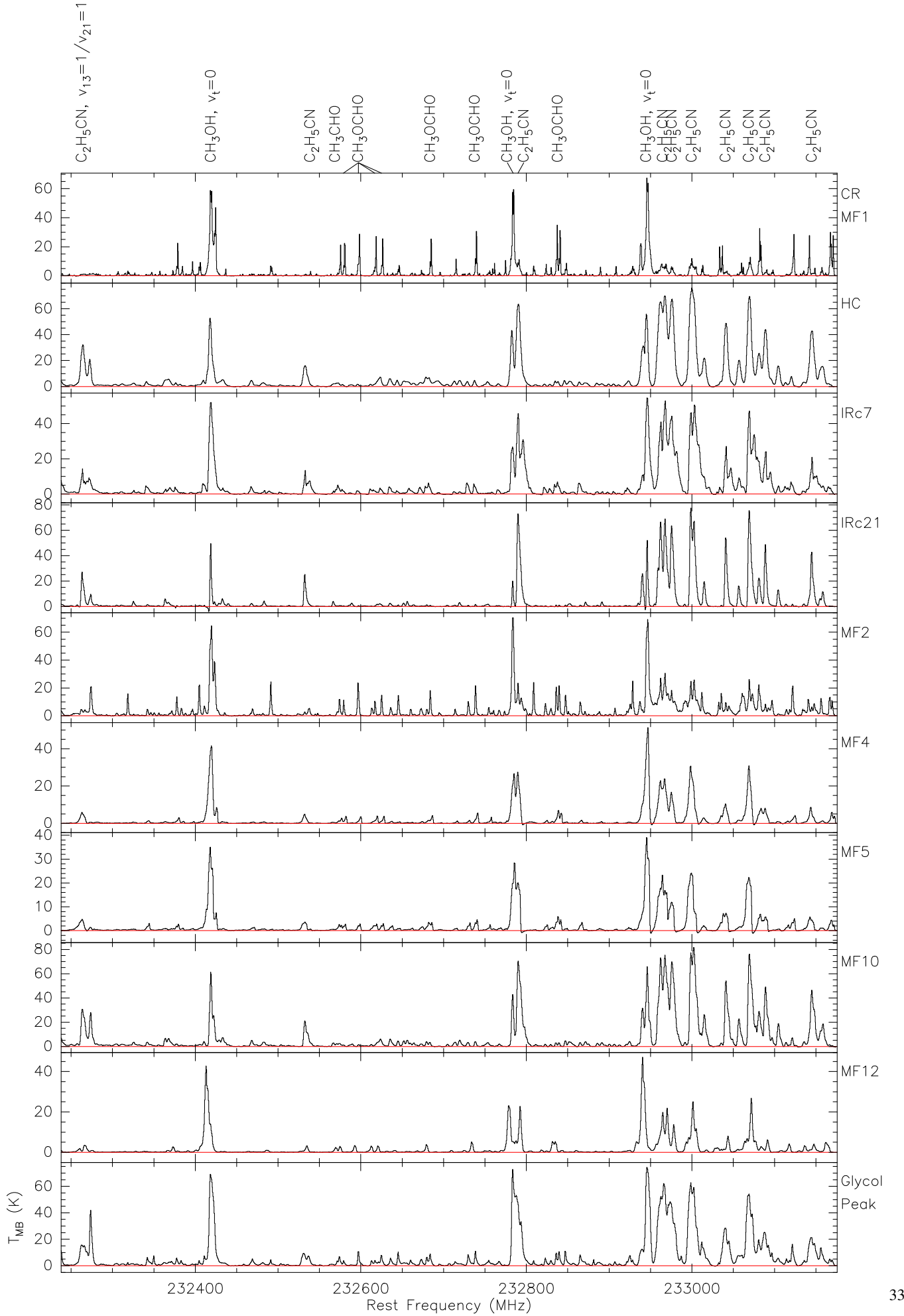


Fig. A.1i. Spectra from the band 9 setup for all ten sources.

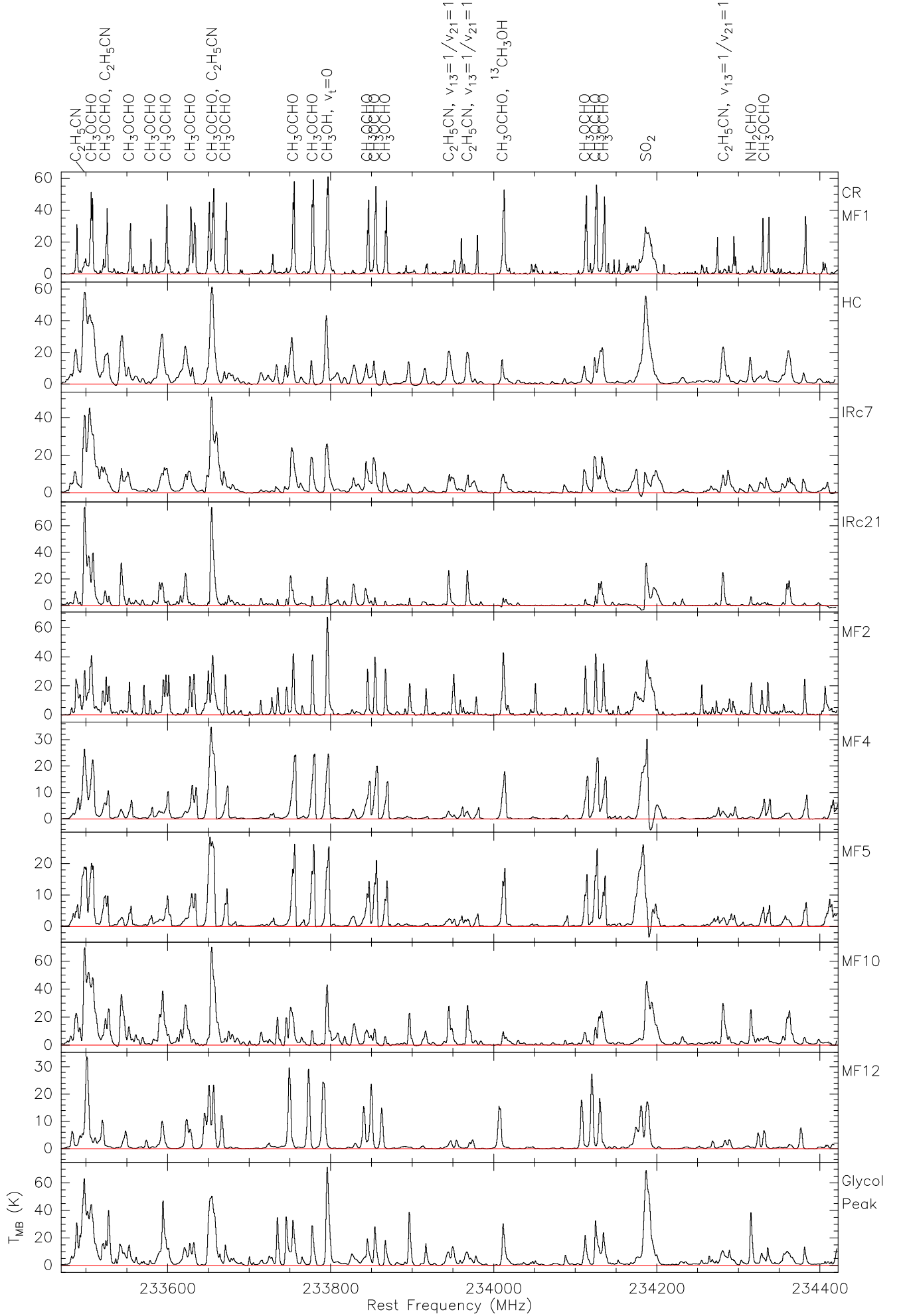


Fig. A.1j. Spectra from the band 10 setup for all ten sources.

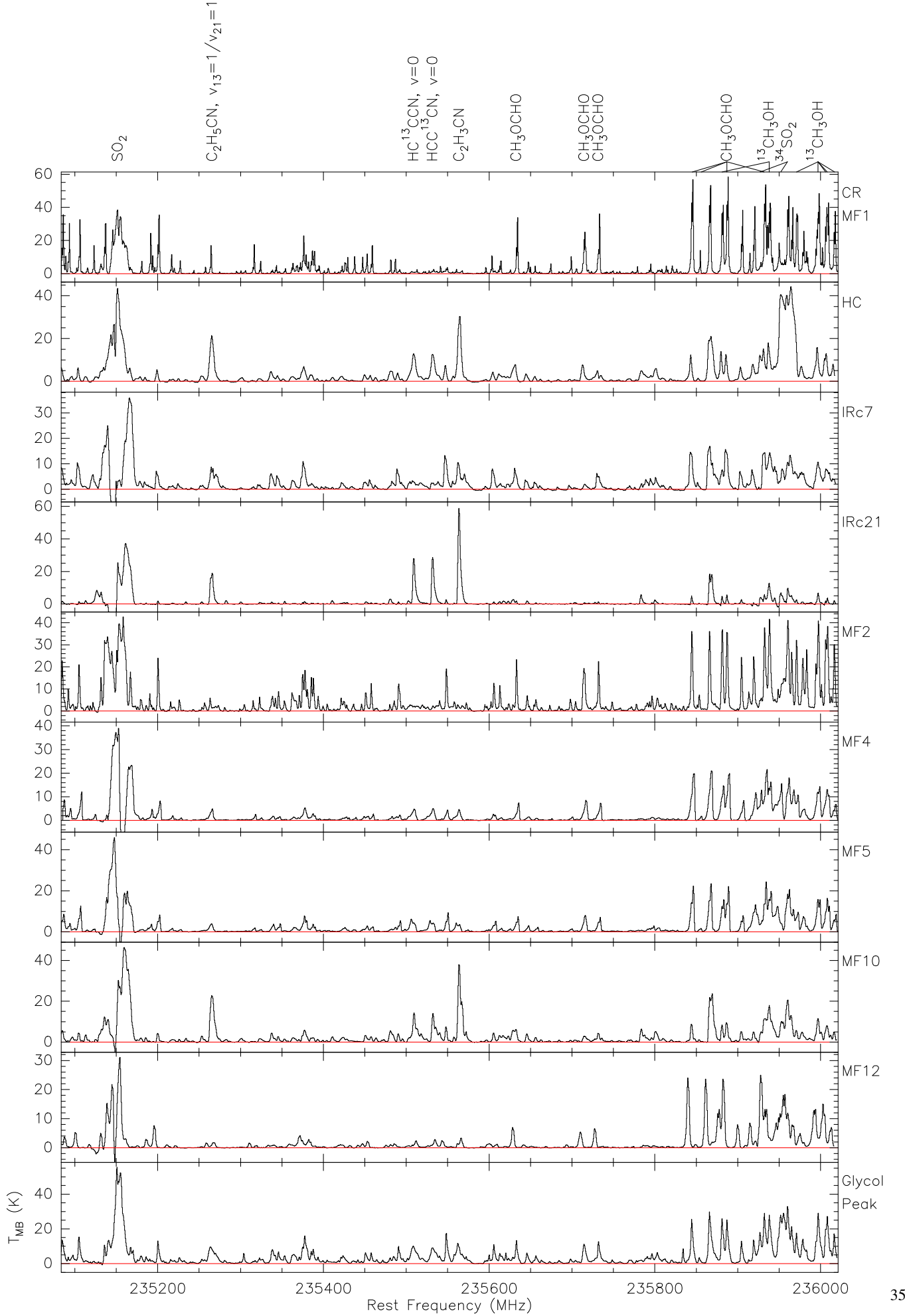


Fig. A.1k. Spectra from the band 11 setup for all ten sources.

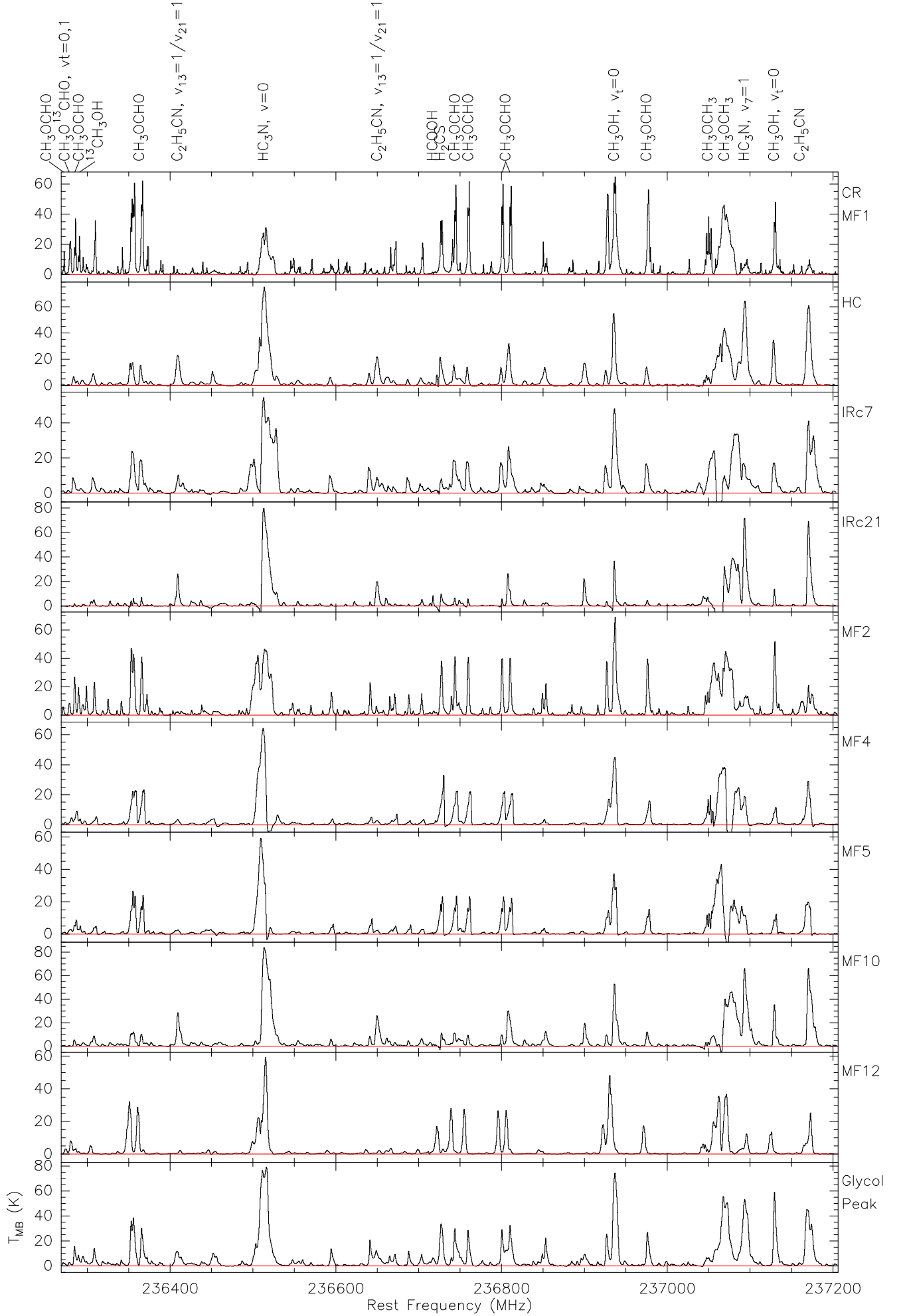


Fig. A.11. Spectra from the band 12 setup for all ten sources.

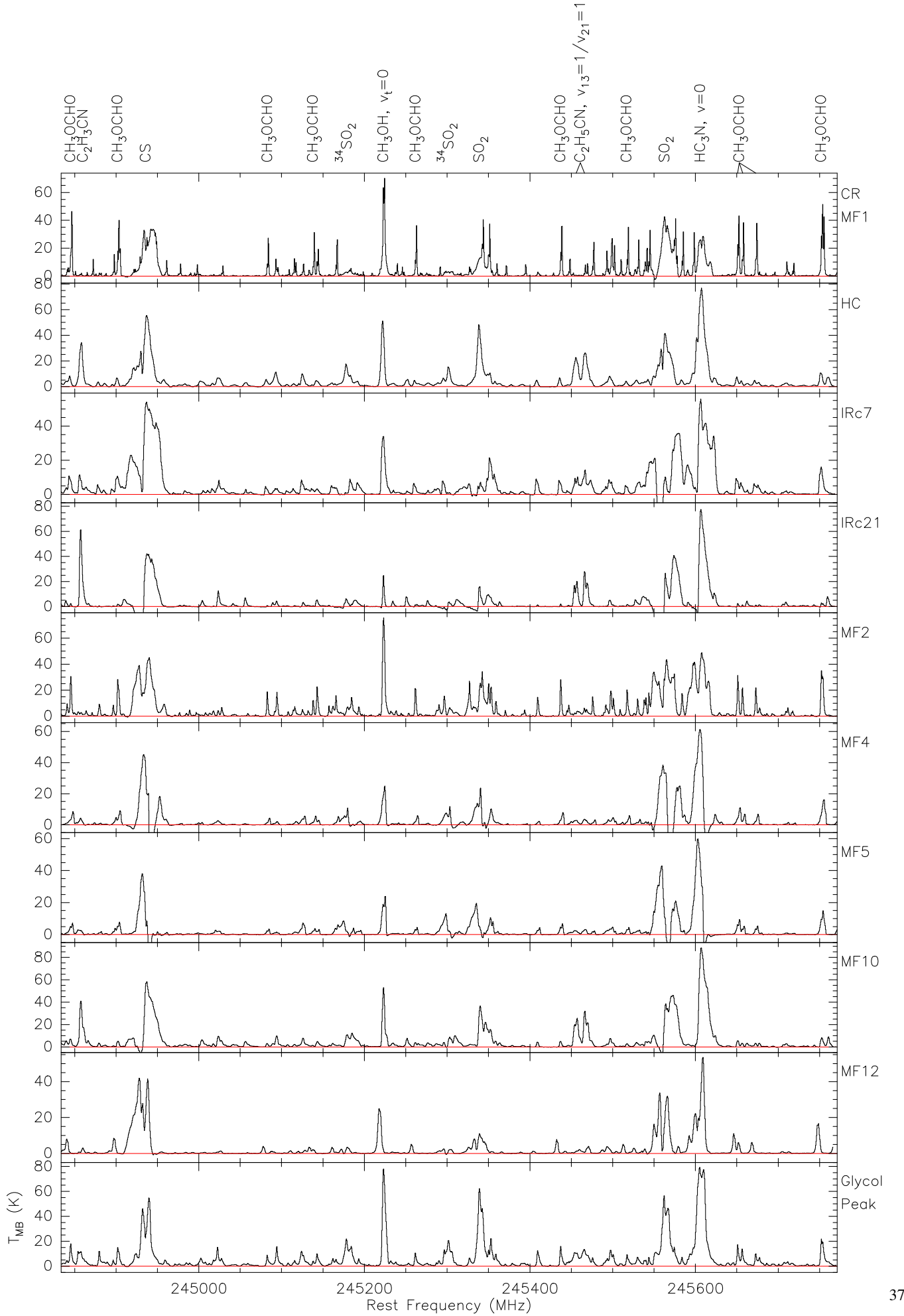


Fig. A.1m. Spectra from the band 13 setup for all ten sources.



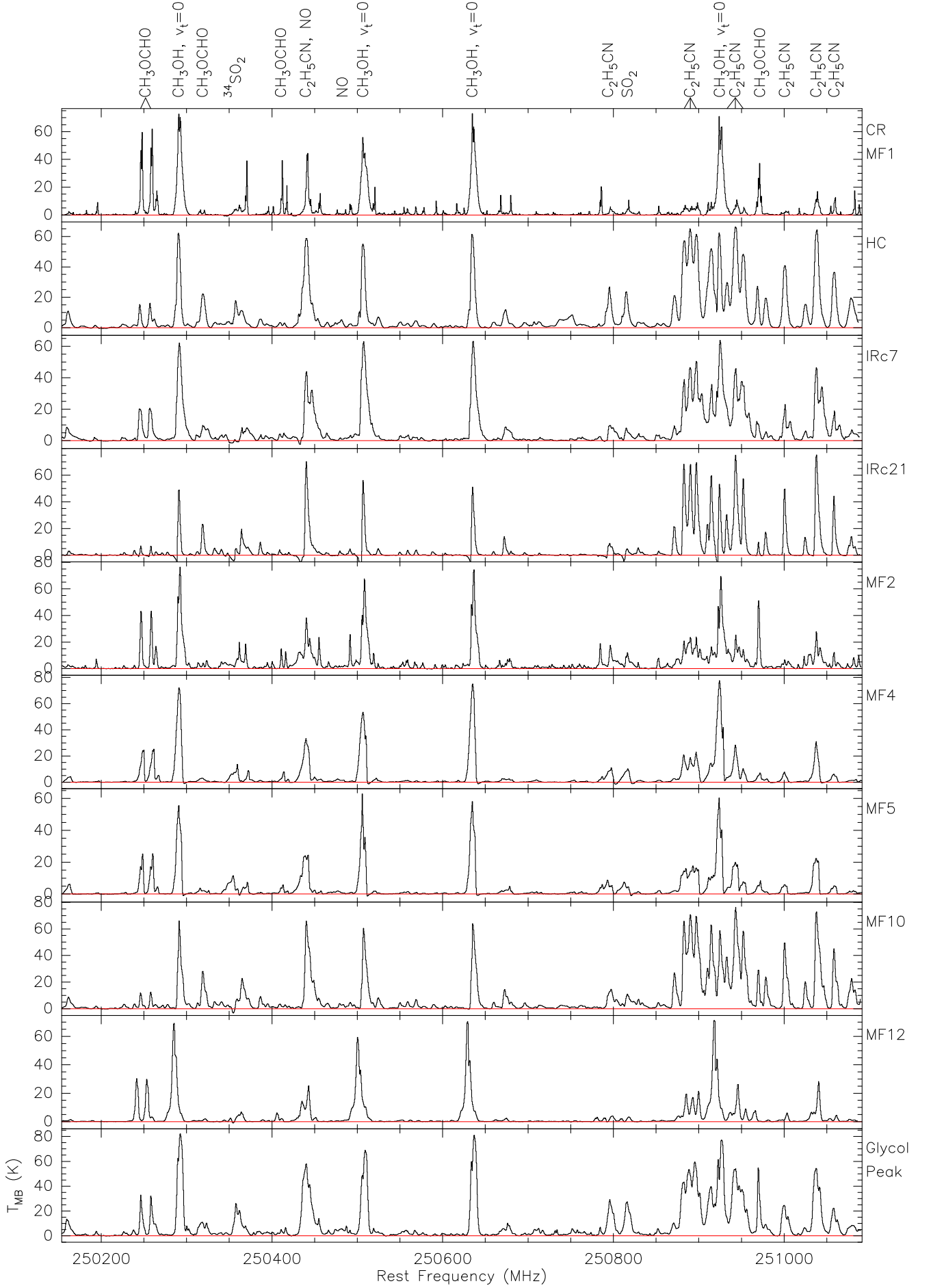


Fig. A.10. Spectra from the band 15 setup for all ten sources.

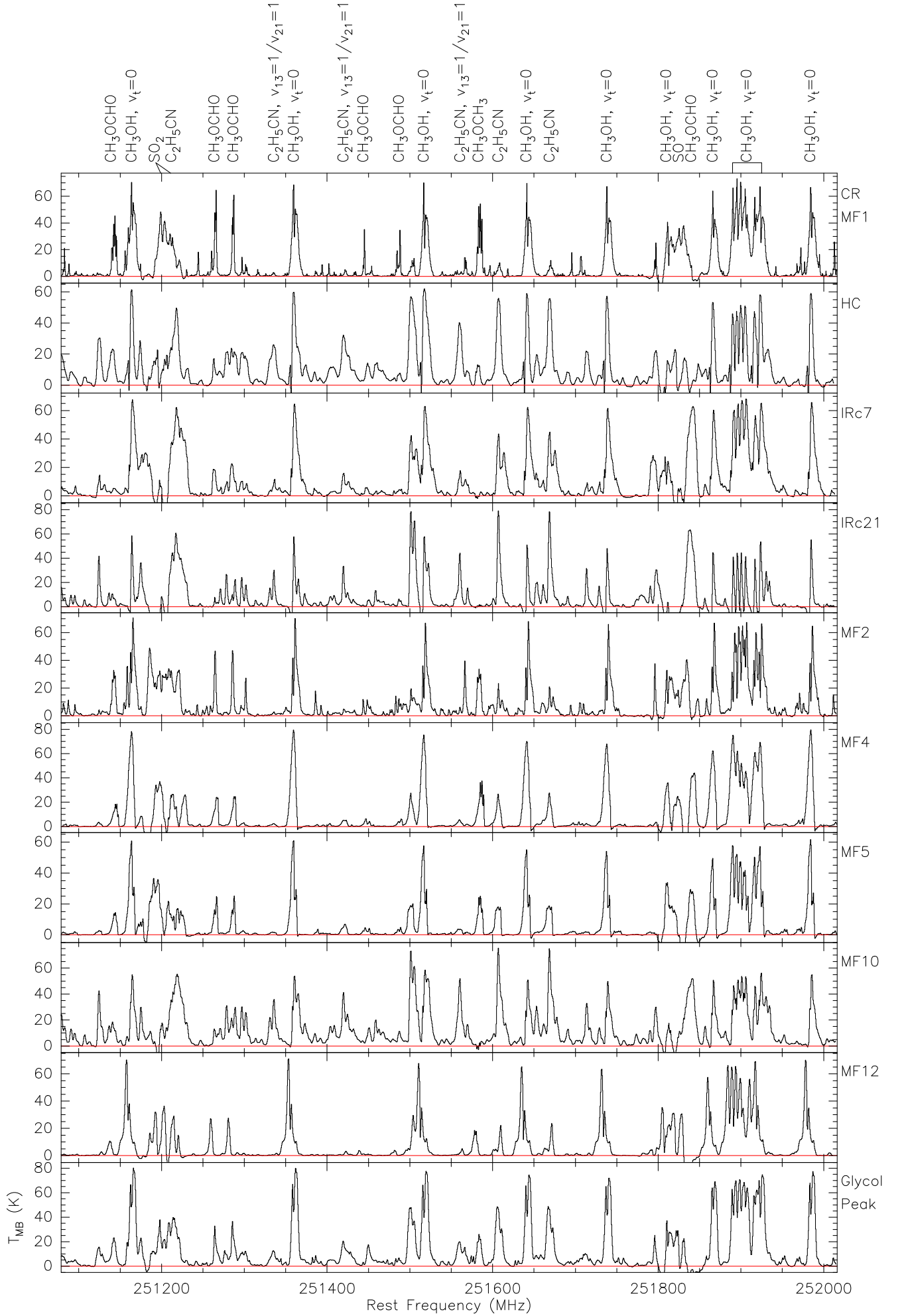


Fig. A.1p. Spectra from the band 16 setup for all ten sources.

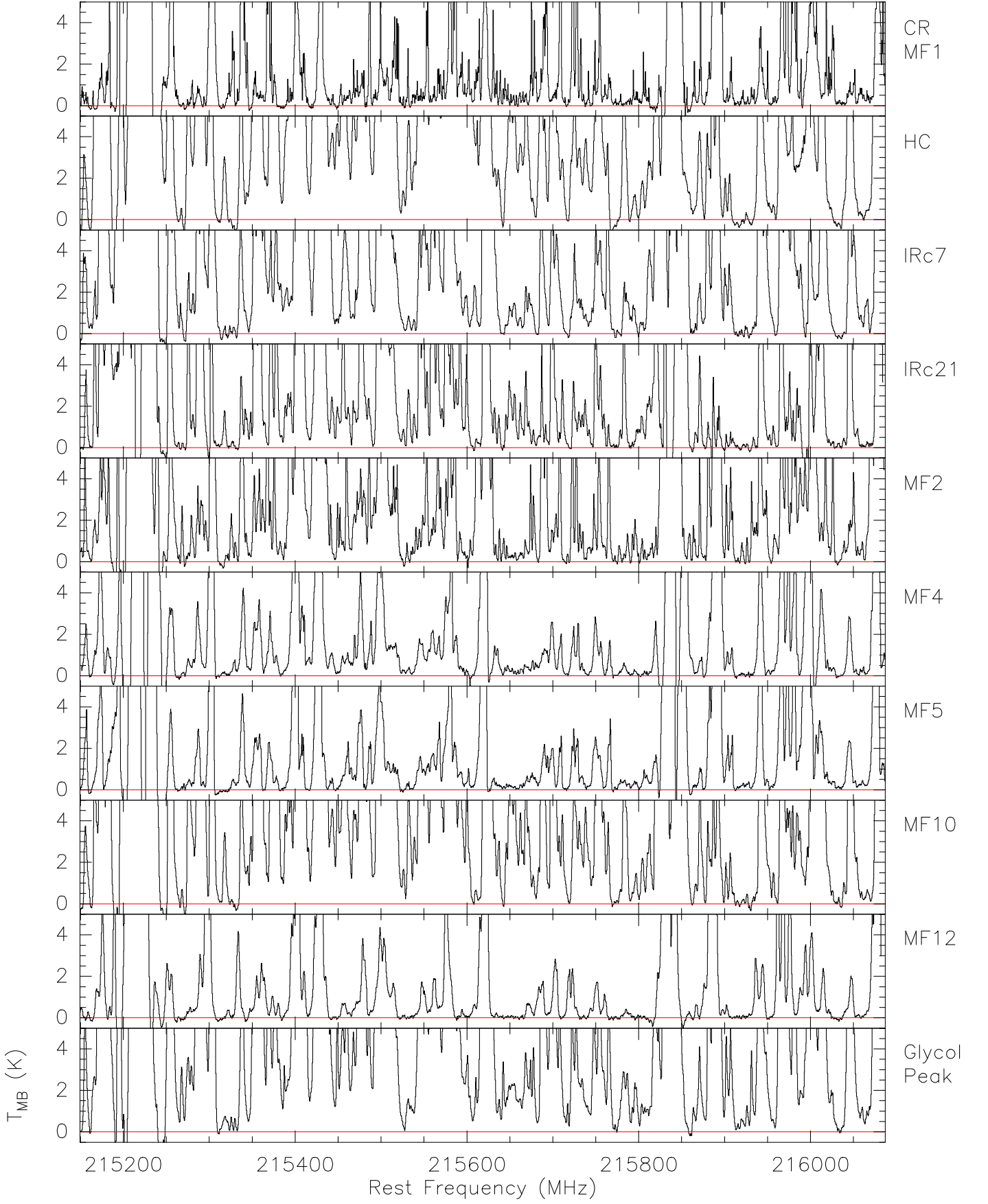


Fig. A.2a. Spectra from the band 1 setup for all ten sources with a fixed maximum temperature scale of 5 K to highlight the weaker lines. The red line indicates the 0 K (continuum-removed) level. This figure is identical to Fig. 3 and is reproduced here for completeness of the Appendix.

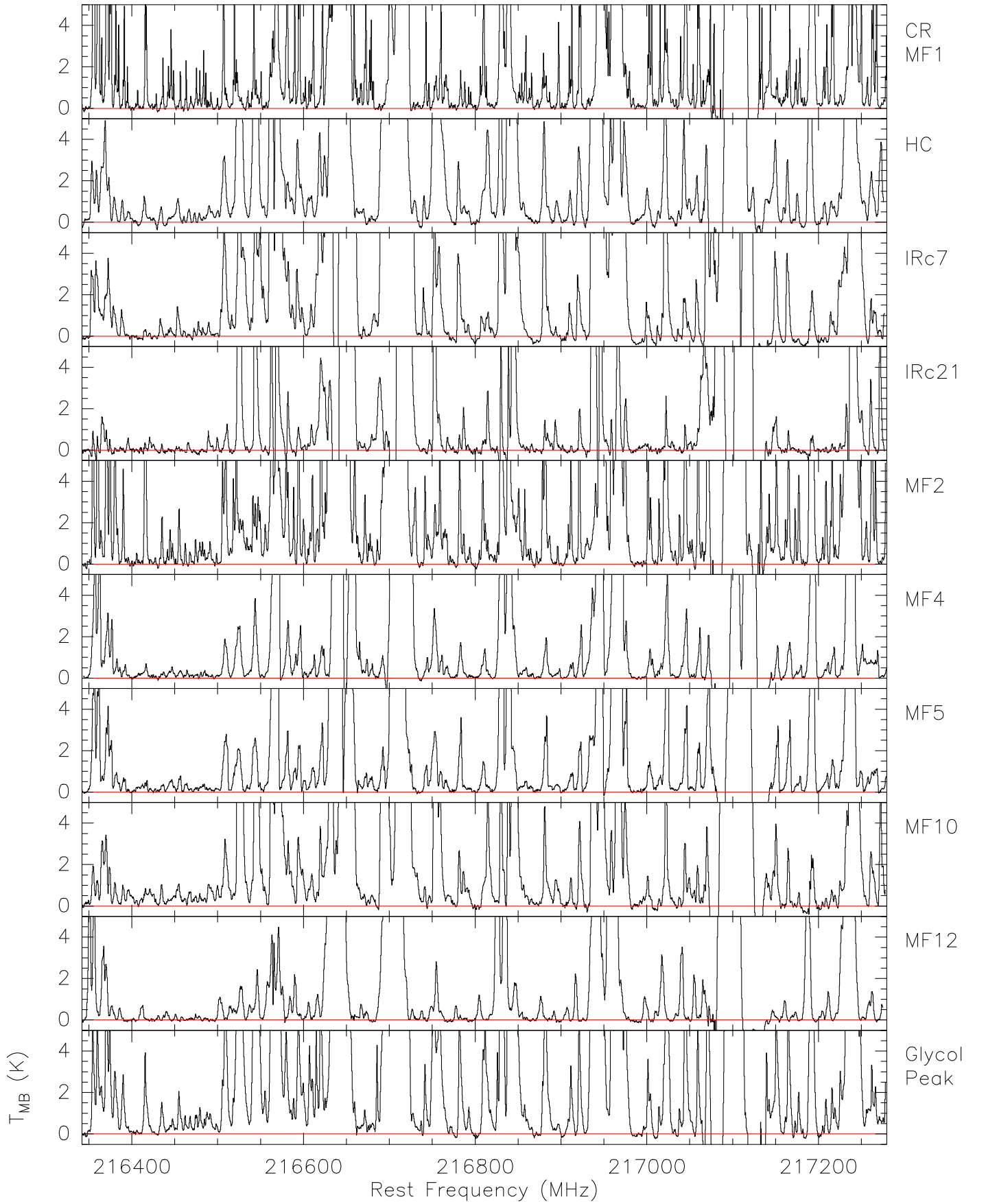


Fig. A.2b. Spectra from the band 2 setup for all ten sources with a fixed maximum temperature scale of 5 K to highlight the weaker lines. The red line indicates the 0 K (continuum-removed) level.

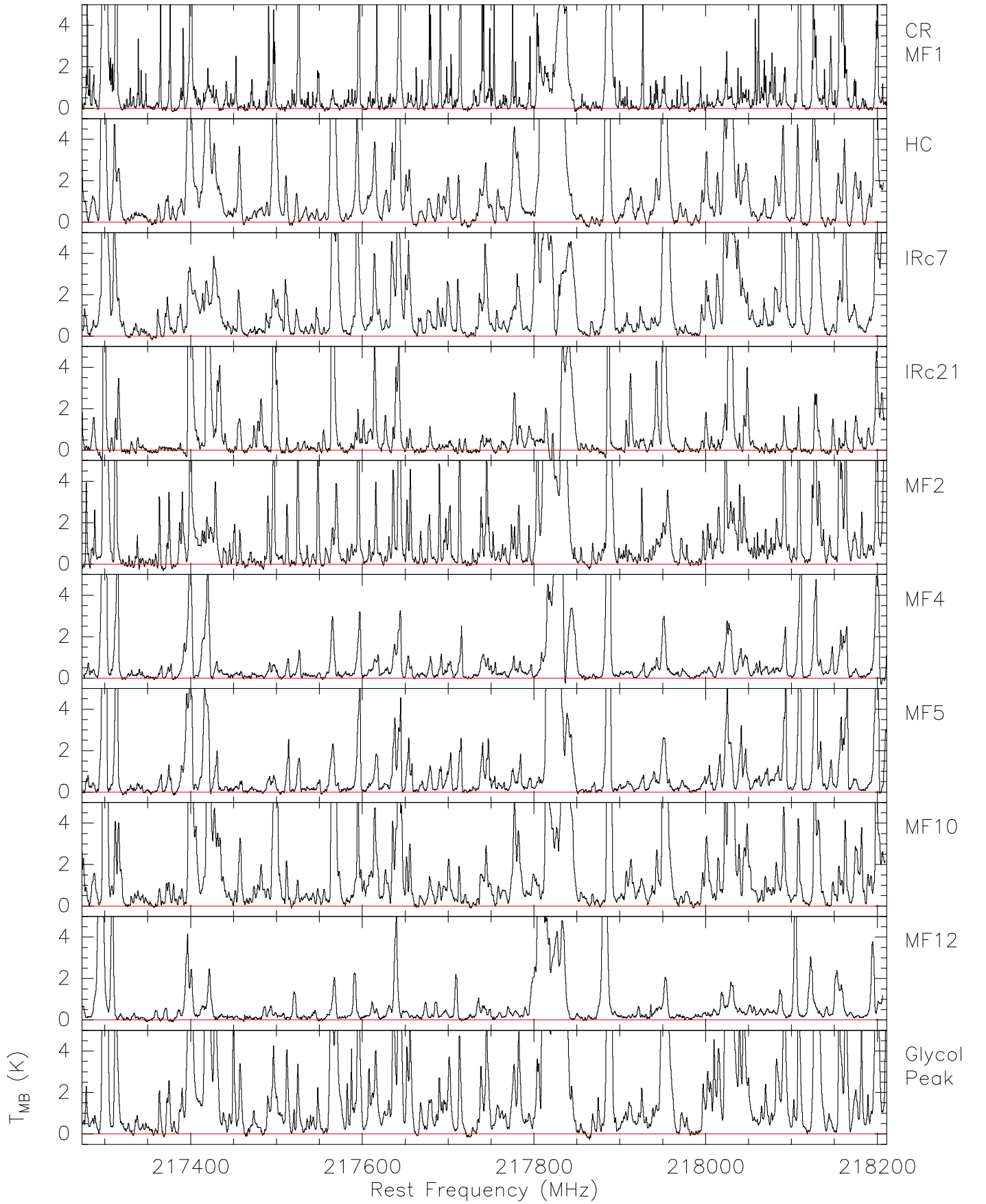


Fig. A.2c. Spectra from the band 3 setup for all ten sources with a fixed maximum temperature scale of 5 K to highlight the weaker lines. The red line indicates the 0 K (continuum-removed) level.

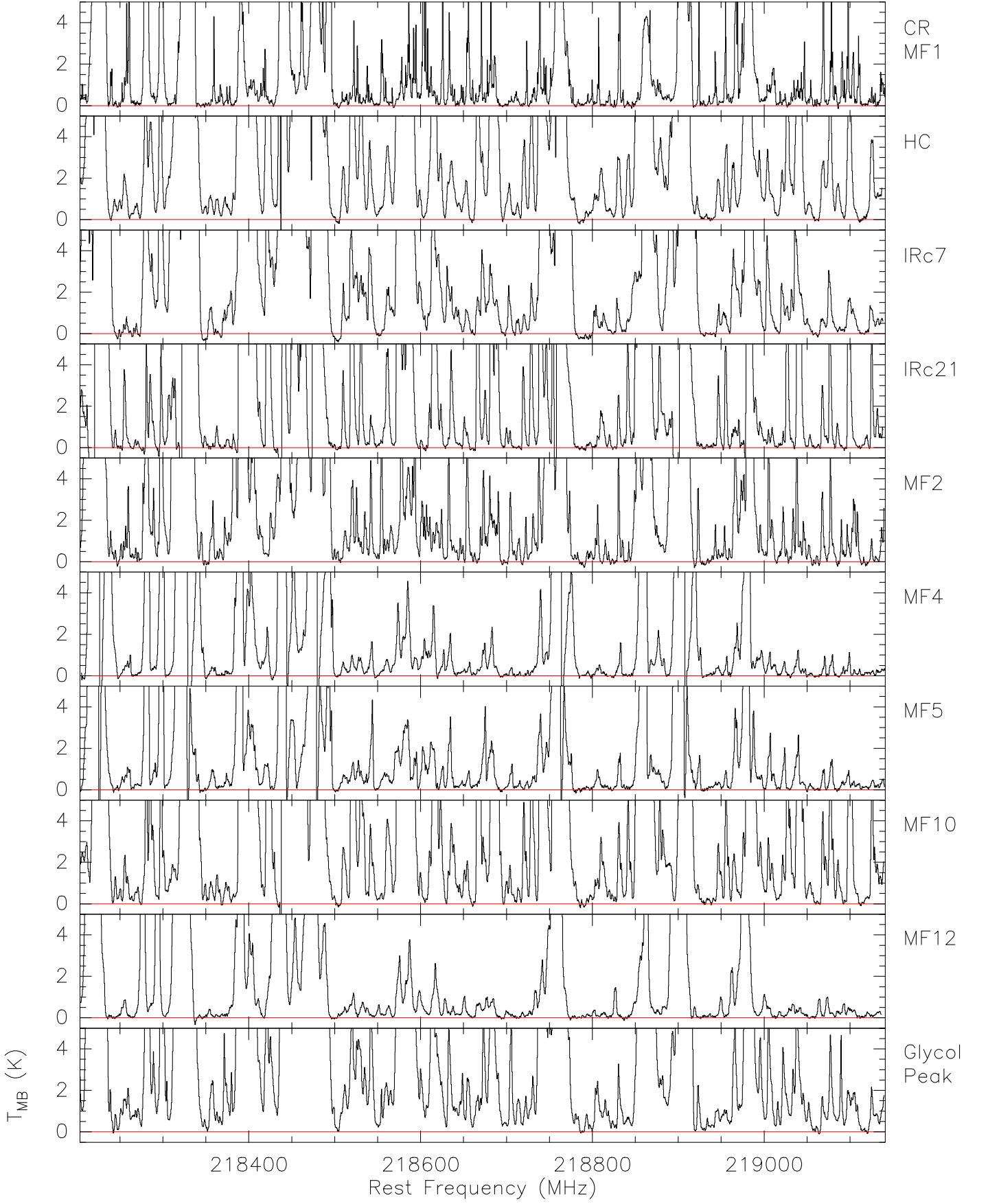


Fig. A.2d. Spectra from the band 4 setup for all ten sources with a fixed maximum temperature scale of 5 K to highlight the weaker lines. The red line indicates the 0 K (continuum-removed) level.

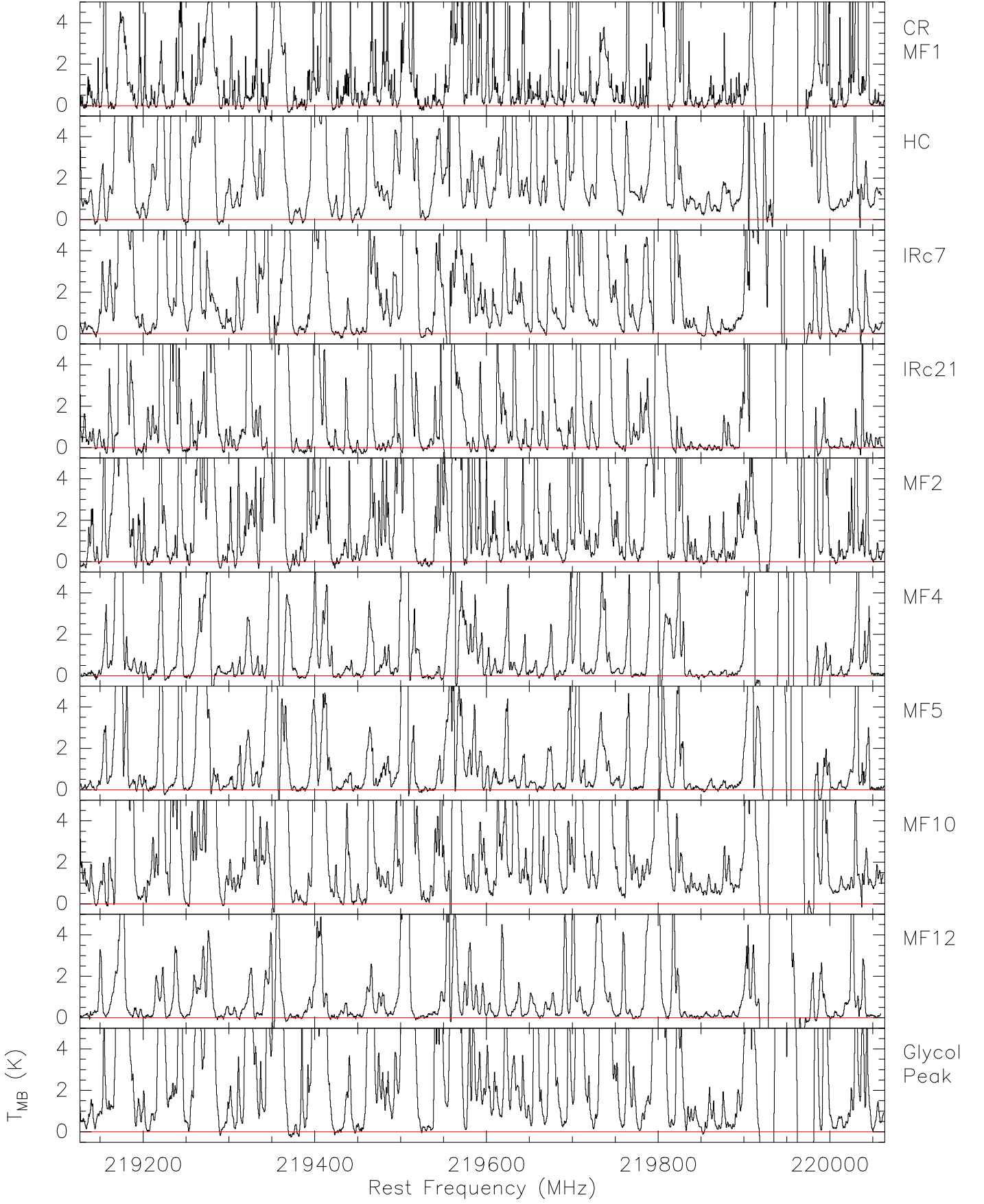


Fig. A.2e. Spectra from the band 5 setup for all ten sources with a fixed maximum temperature scale of 5 K to highlight the weaker lines. A ~ 250 MHz overlap with Fig A.2f is present, due to an incorrect setup. The red line indicates the 0 K (continuum-removed) level.

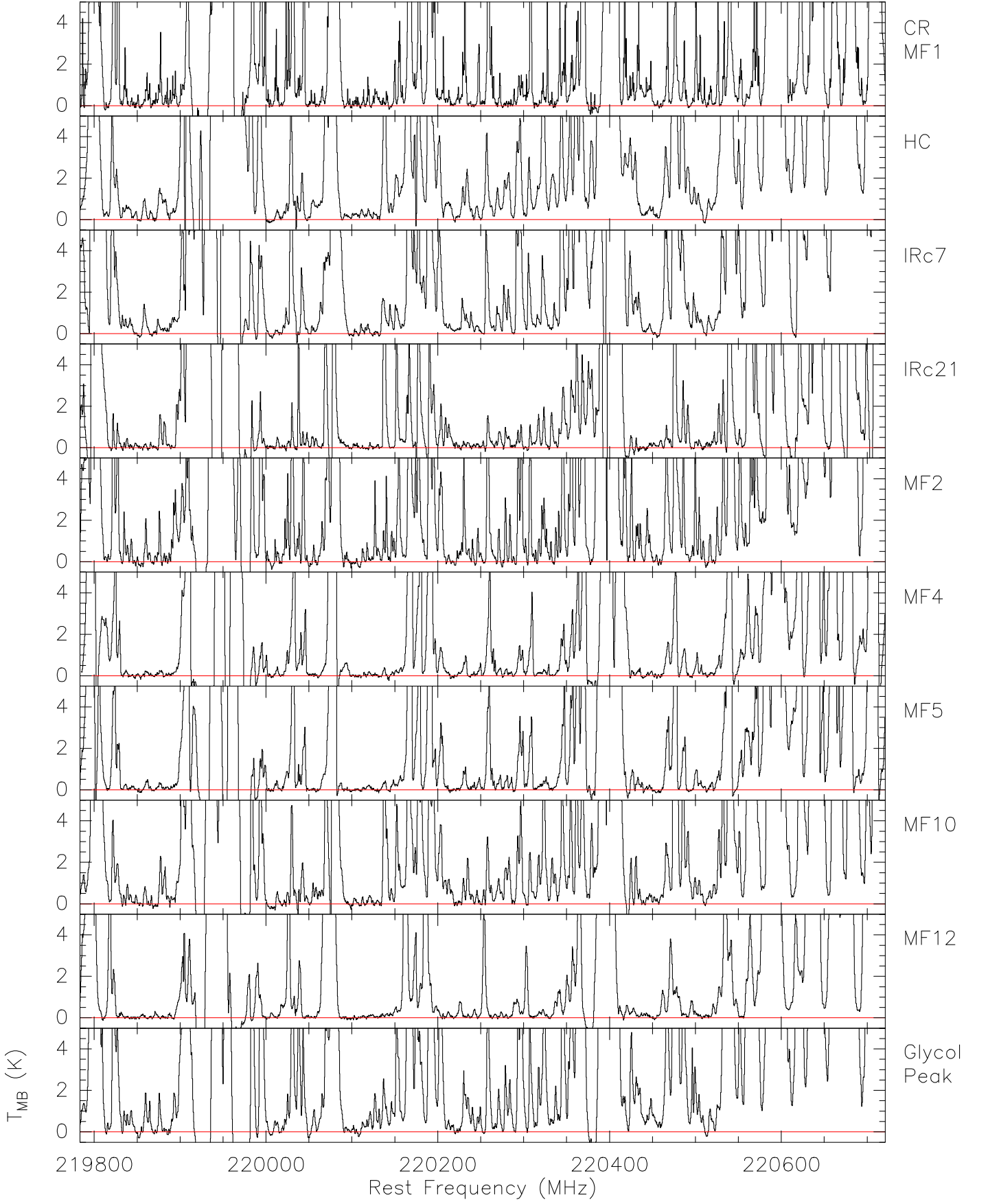


Fig. A.2f. Spectra from the band 6 setup for all ten sources with a fixed maximum temperature scale of 5 K to highlight the weaker lines. The red line indicates the 0 K (continuum-removed) level.

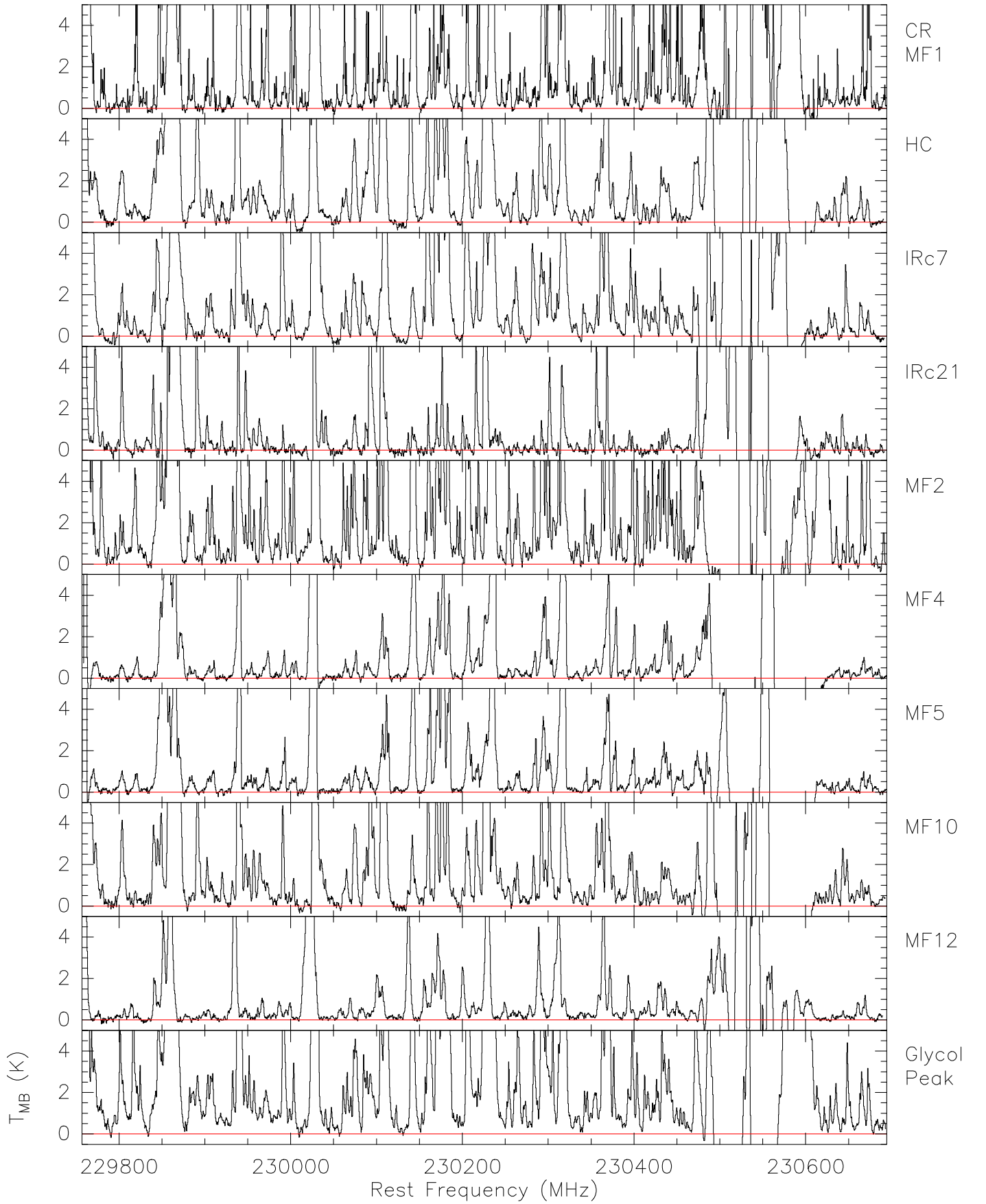


Fig. A.2g. Spectra from the band 7 setup for all ten sources with a fixed maximum temperature scale of 5 K to highlight the weaker lines. The red line indicates the 0 K (continuum-removed) level.

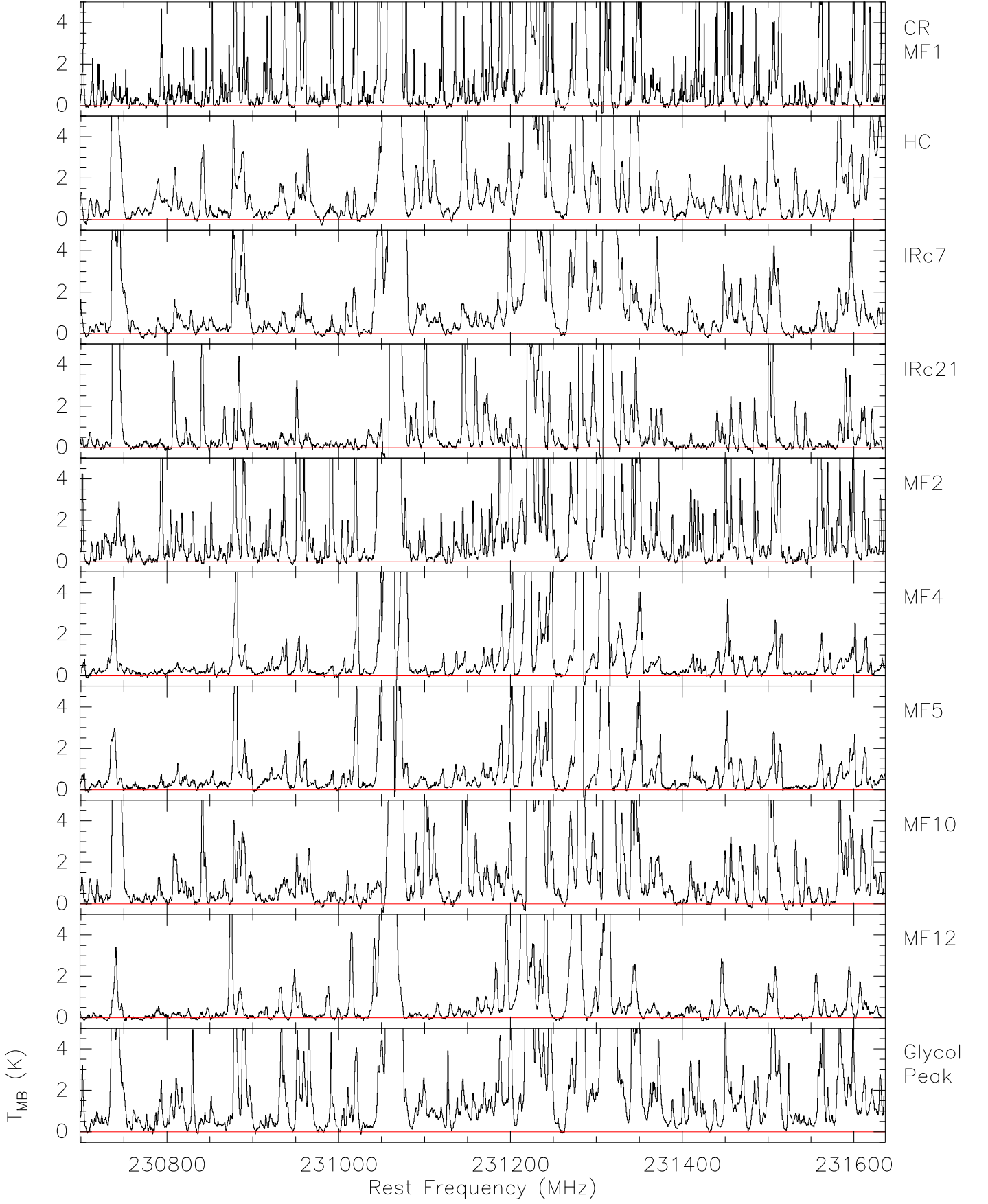


Fig. A.2h. Spectra from the band 8 setup for all ten sources with a fixed maximum temperature scale of 5 K to highlight the weaker lines. The red line indicates the 0 K (continuum-removed) level.

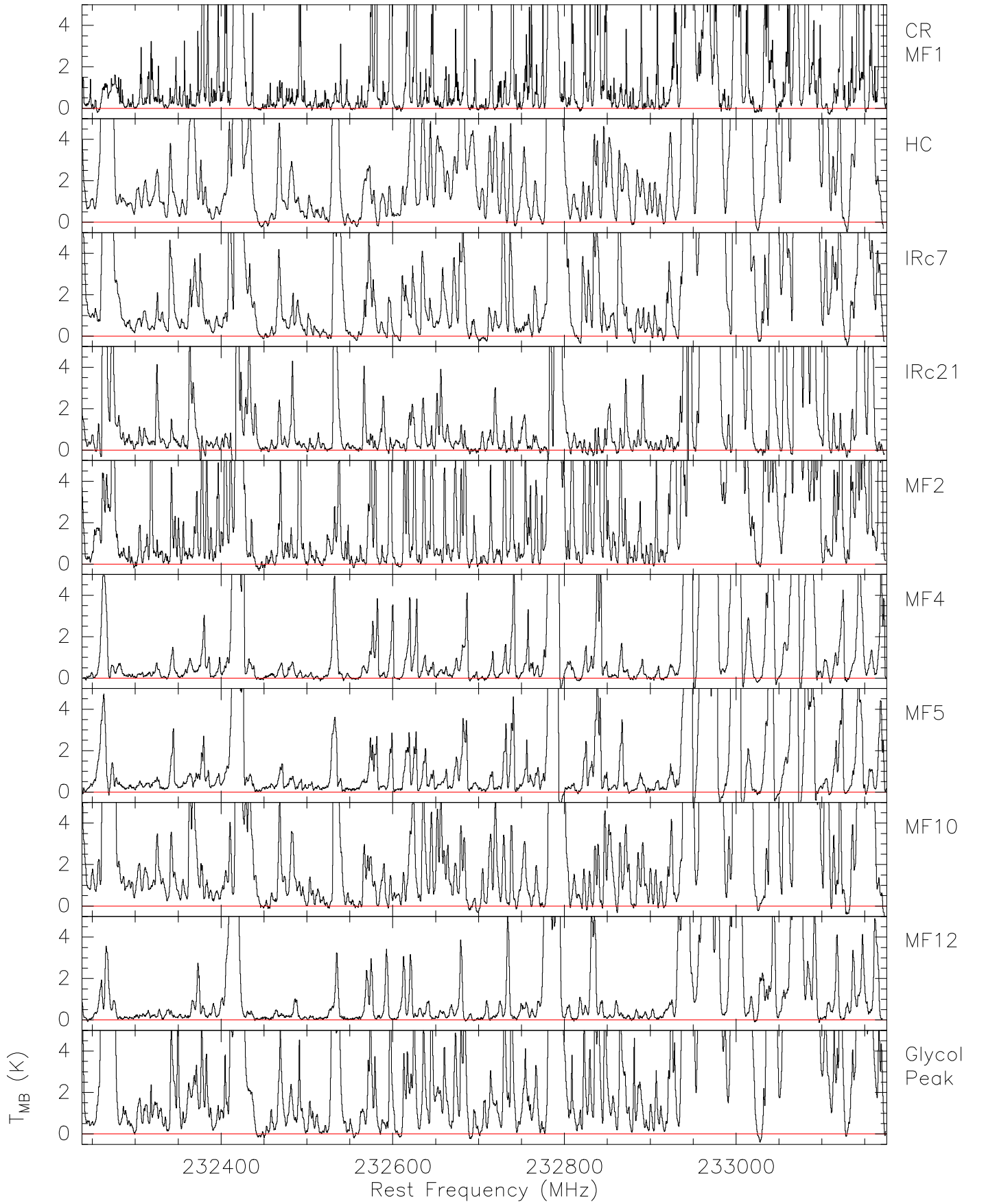


Fig. A.2i. Spectra from the band 9 setup for all ten sources with a fixed maximum temperature scale of 5 K to highlight the weaker lines. The red line indicates the 0 K (continuum-removed) level.

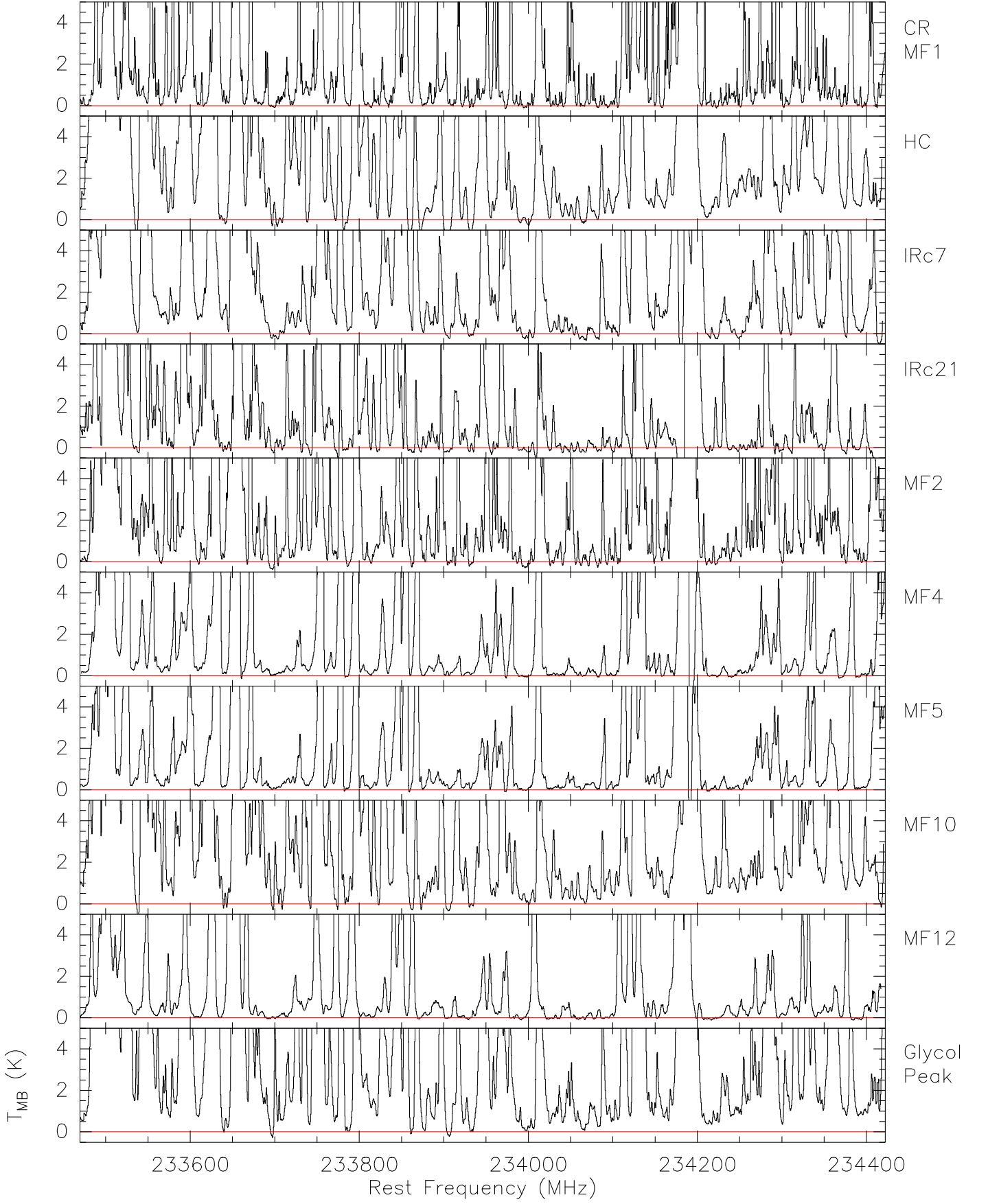


Fig. A.2j. Spectra from the band 10 setup for all ten sources with a fixed maximum temperature scale of 5 K to highlight the weaker lines. The red line indicates the 0 K (continuum-removed) level.

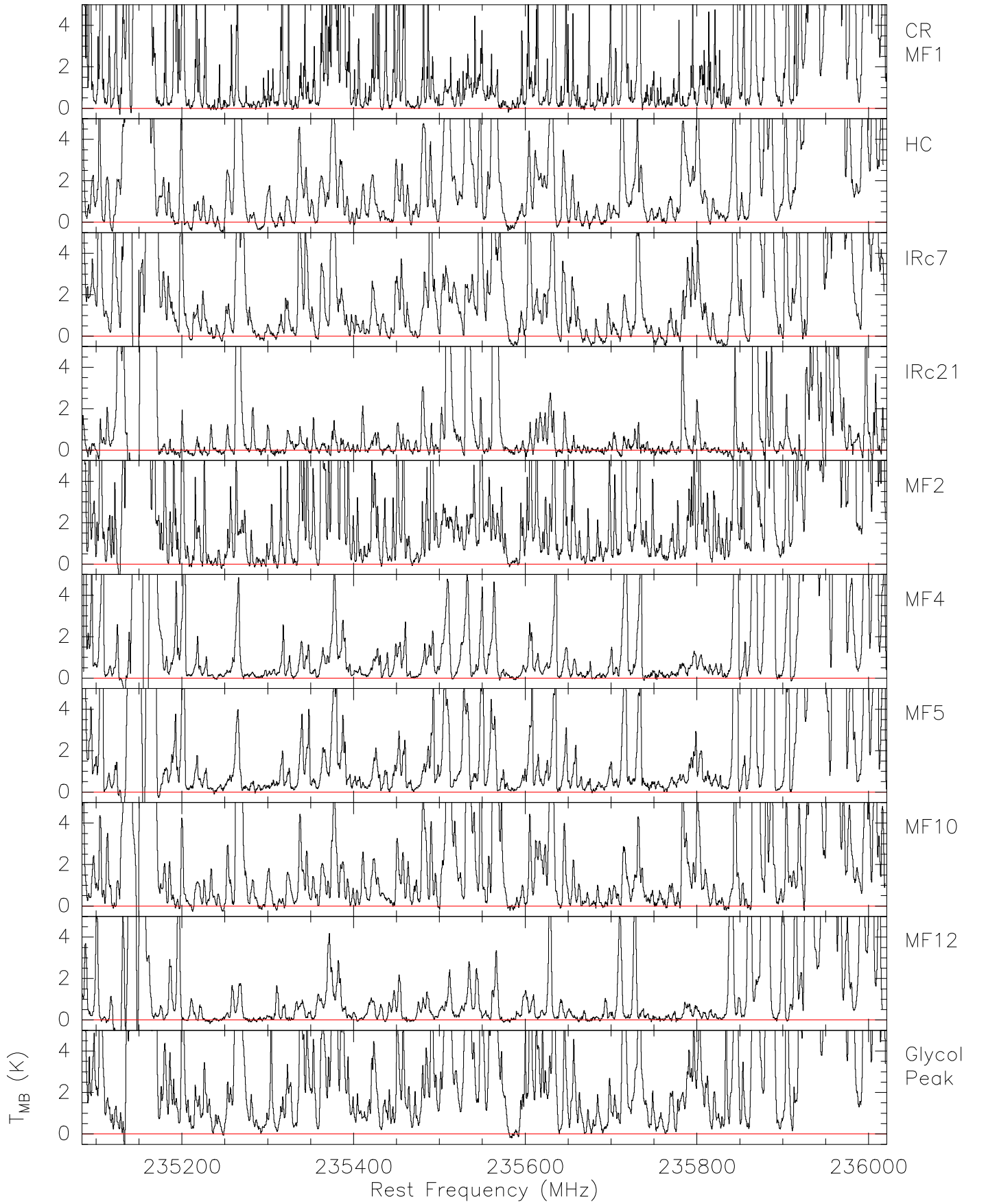


Fig. A.2k. Spectra from the band 11 setup for all ten sources with a fixed maximum temperature scale of 5 K to highlight the weaker lines. The red line indicates the 0 K (continuum-removed) level.

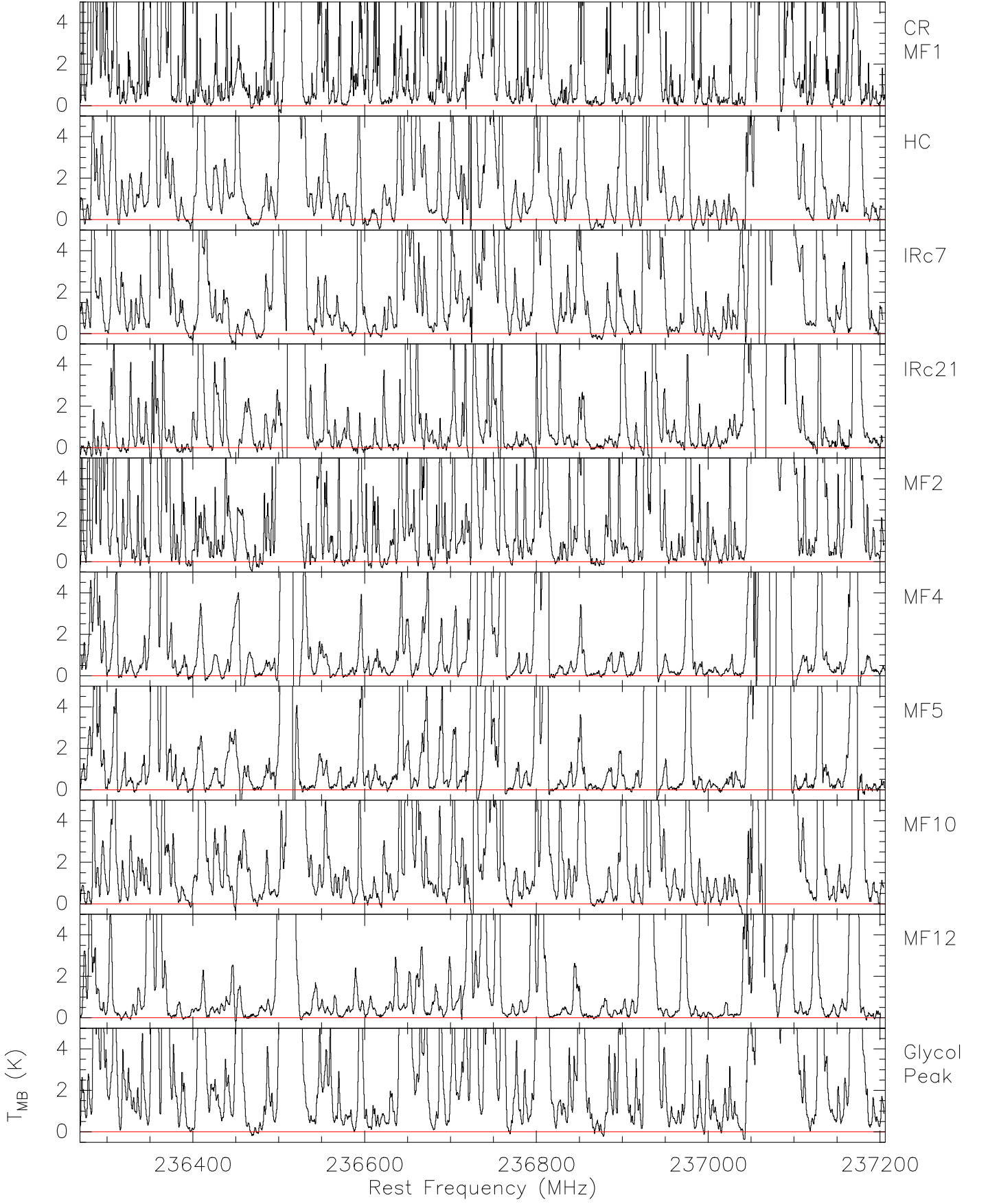


Fig. A.2I. Spectra from the band 12 setup for all ten sources with a fixed maximum temperature scale of 5 K to highlight the weaker lines. The red line indicates the 0 K (continuum-removed) level.

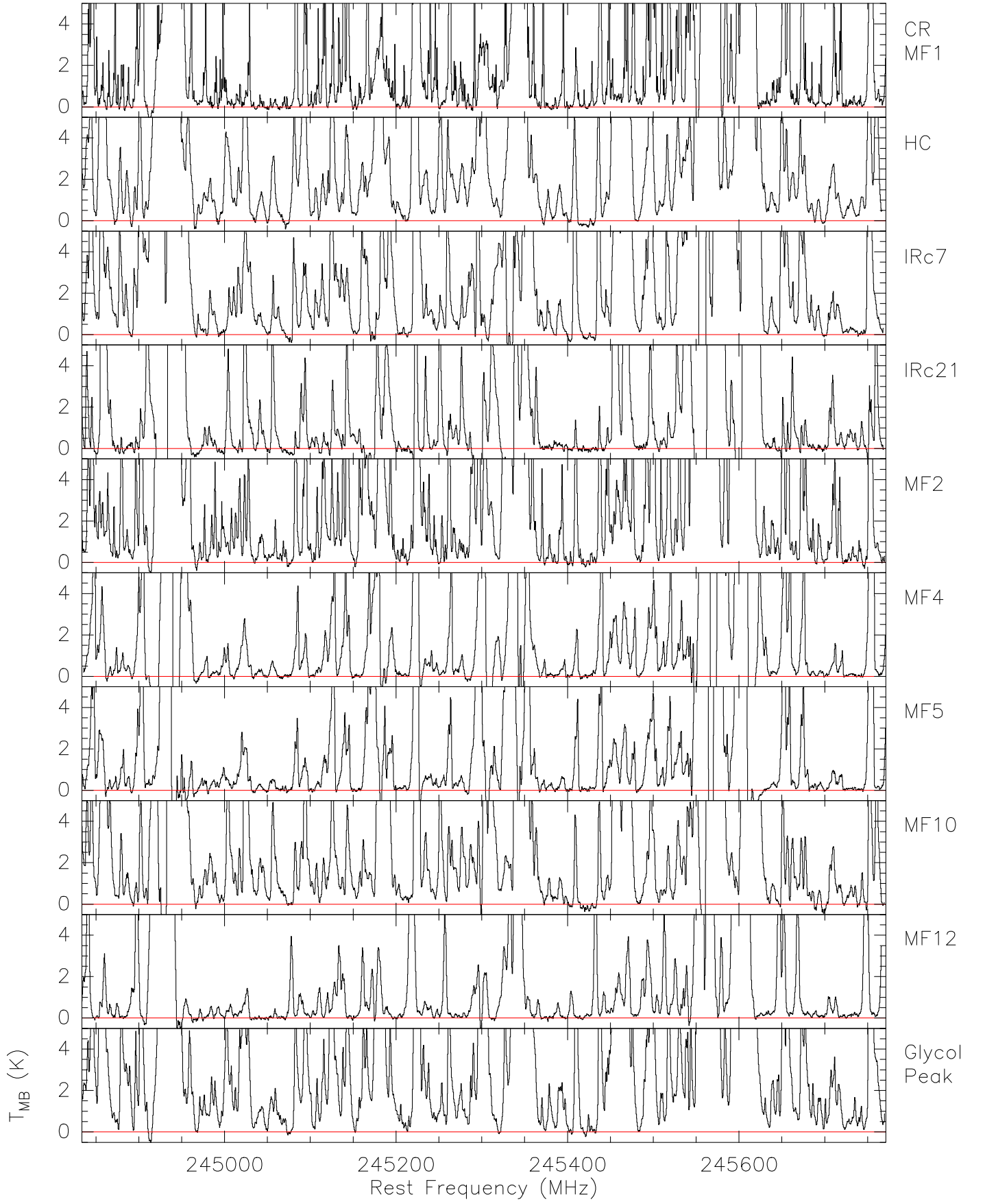


Fig. A.2m. Spectra from the band 13 setup for all ten sources with a fixed maximum temperature scale of 5 K to highlight the weaker lines. The red line indicates the 0 K (continuum-removed) level.

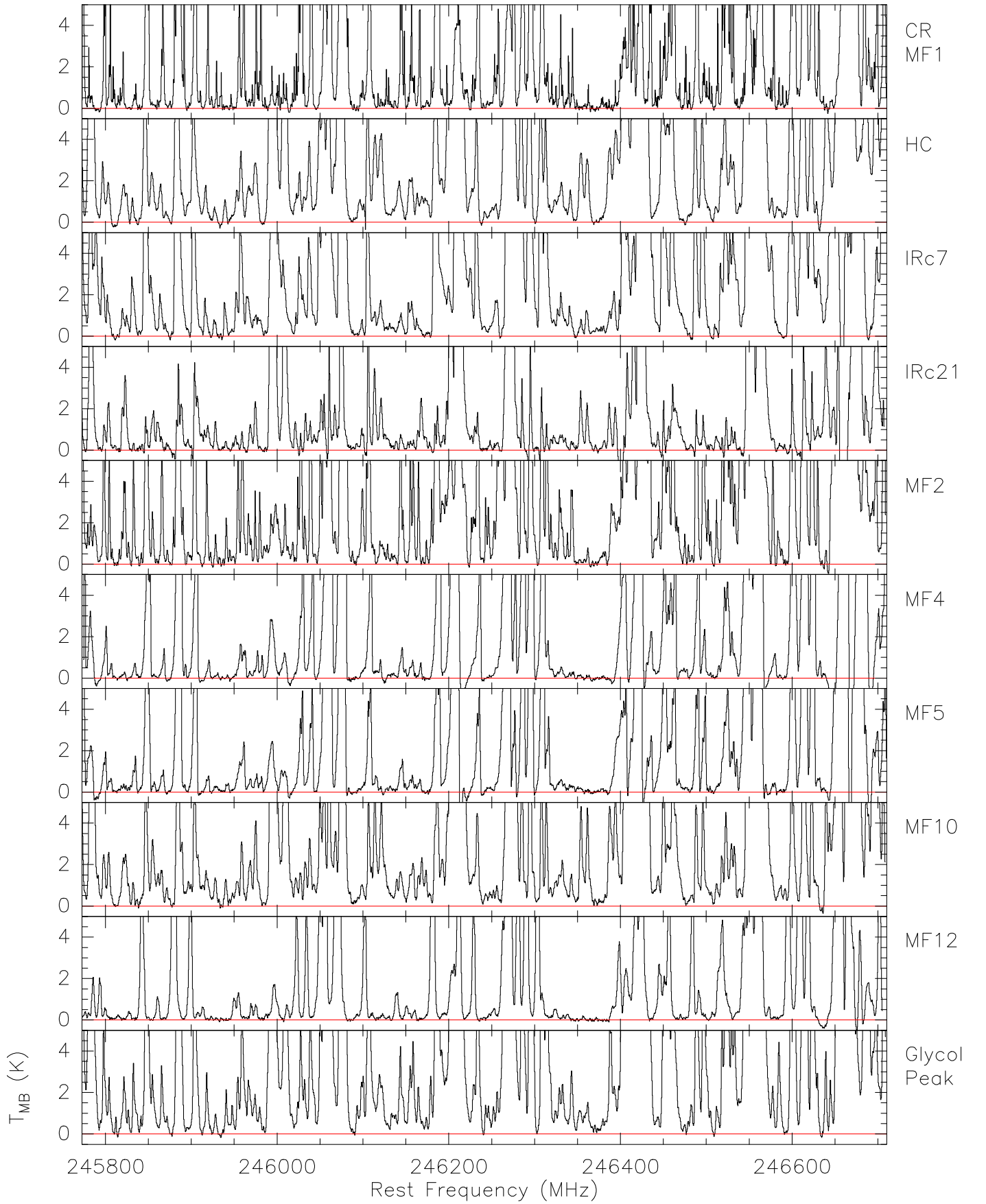


Fig. A.2n. Spectra from the band 14 setup for all ten sources with a fixed maximum temperature scale of 5 K to highlight the weaker lines. The red line indicates the 0 K (continuum-removed) level.

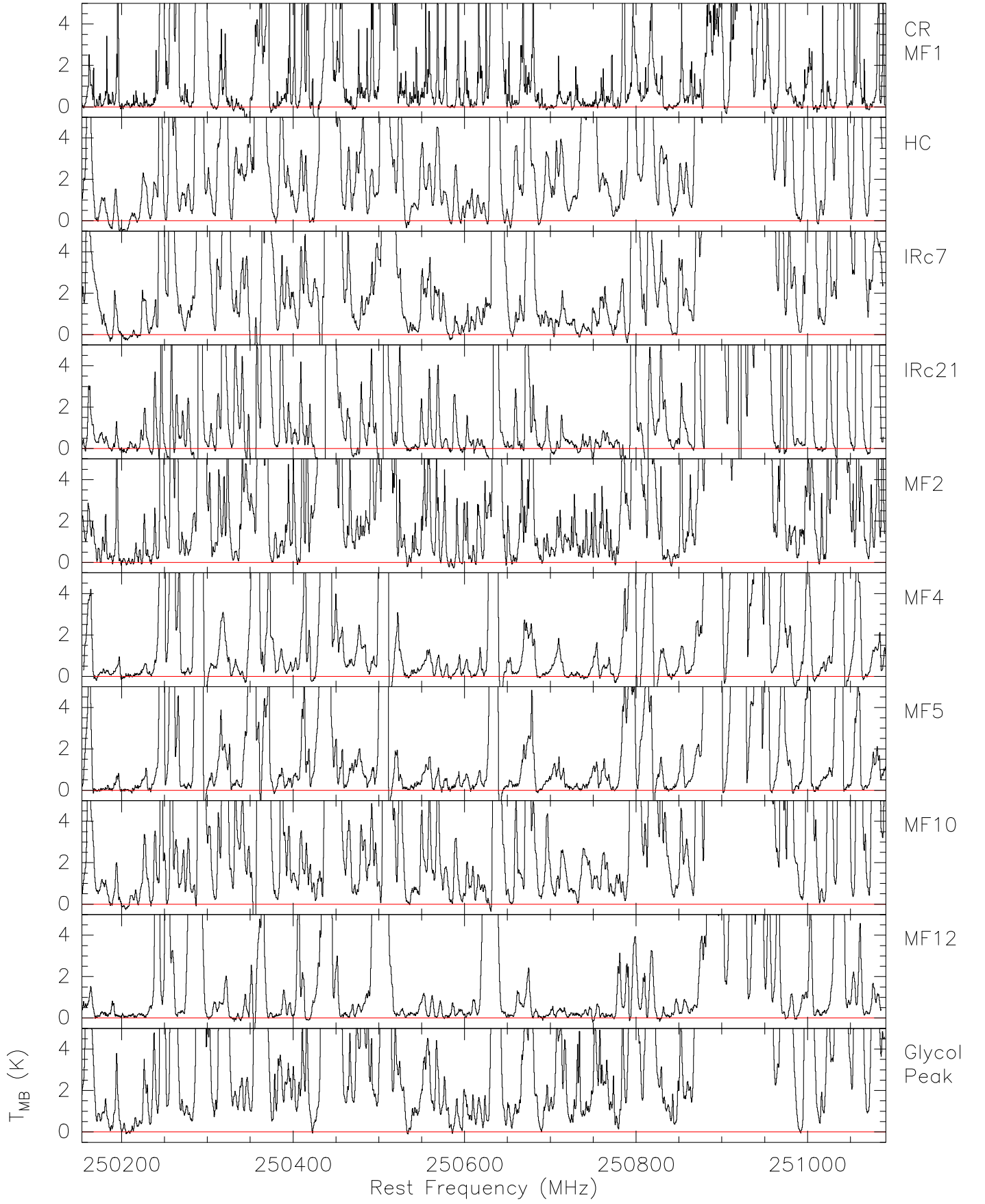


Fig. A.20. Spectra from the band 15 setup for all ten sources with a fixed maximum temperature scale of 5 K to highlight the weaker lines. The red line indicates the 0 K (continuum-removed) level.

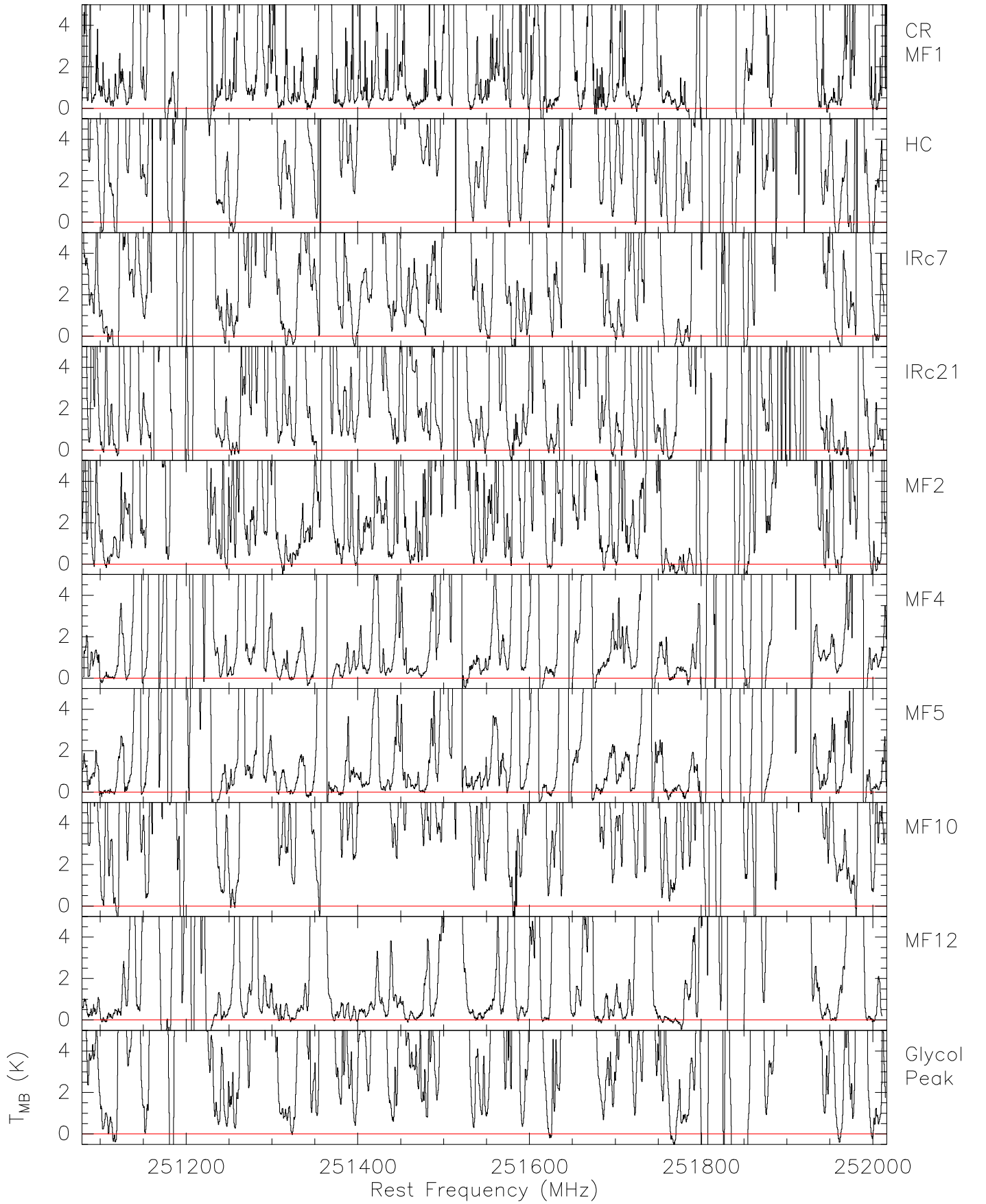


Fig. A.2p. Spectra from the band 16 setup for all ten sources with a fixed maximum temperature scale of 5 K to highlight the weaker lines. The red line indicates the 0 K (continuum-removed) level.

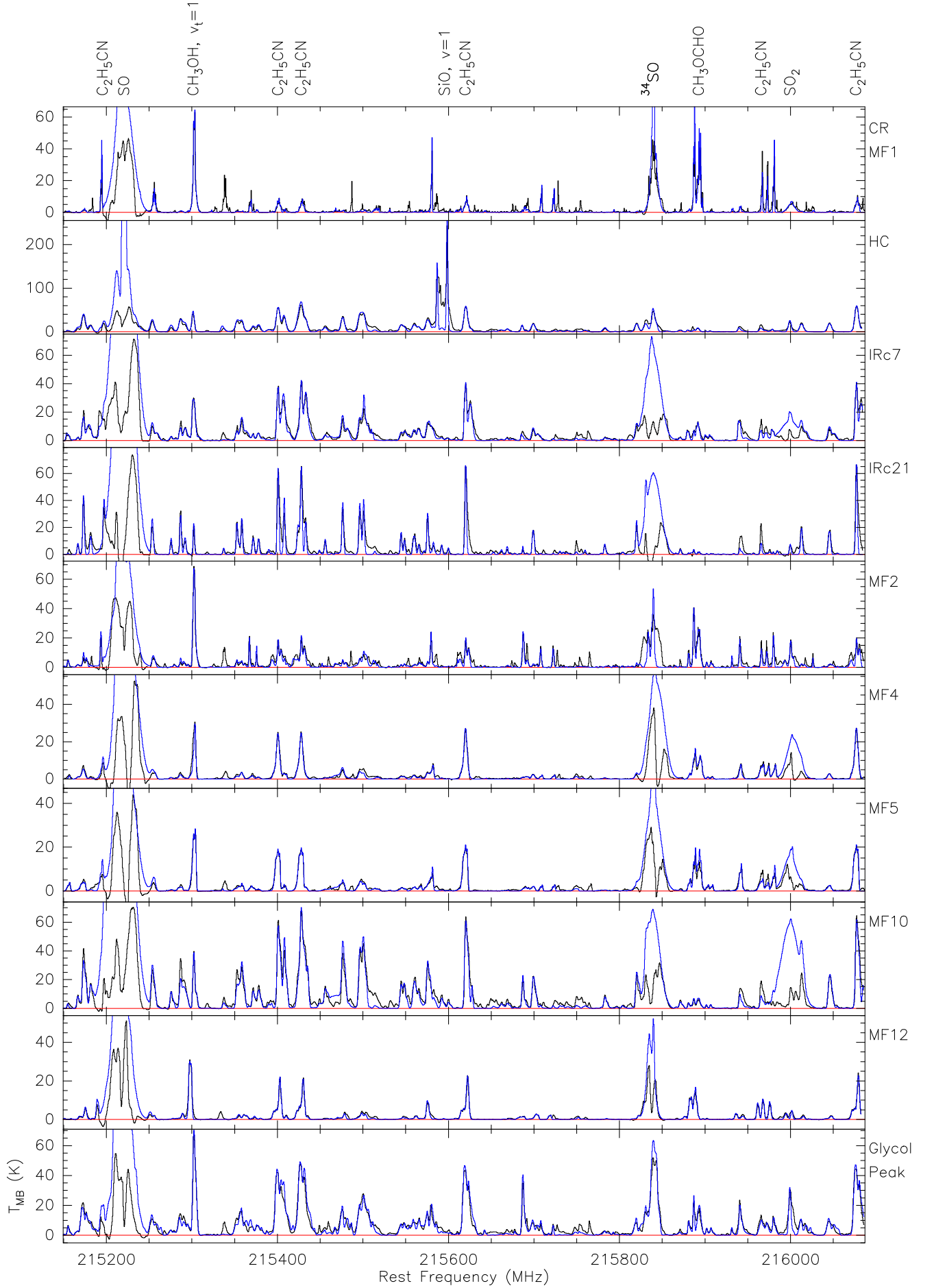


Fig. A.3a. Spectra from the band 1 setup for all ten sources with the summation of fits to individual species in blue. The strongest lines are identified at the top of the figure.

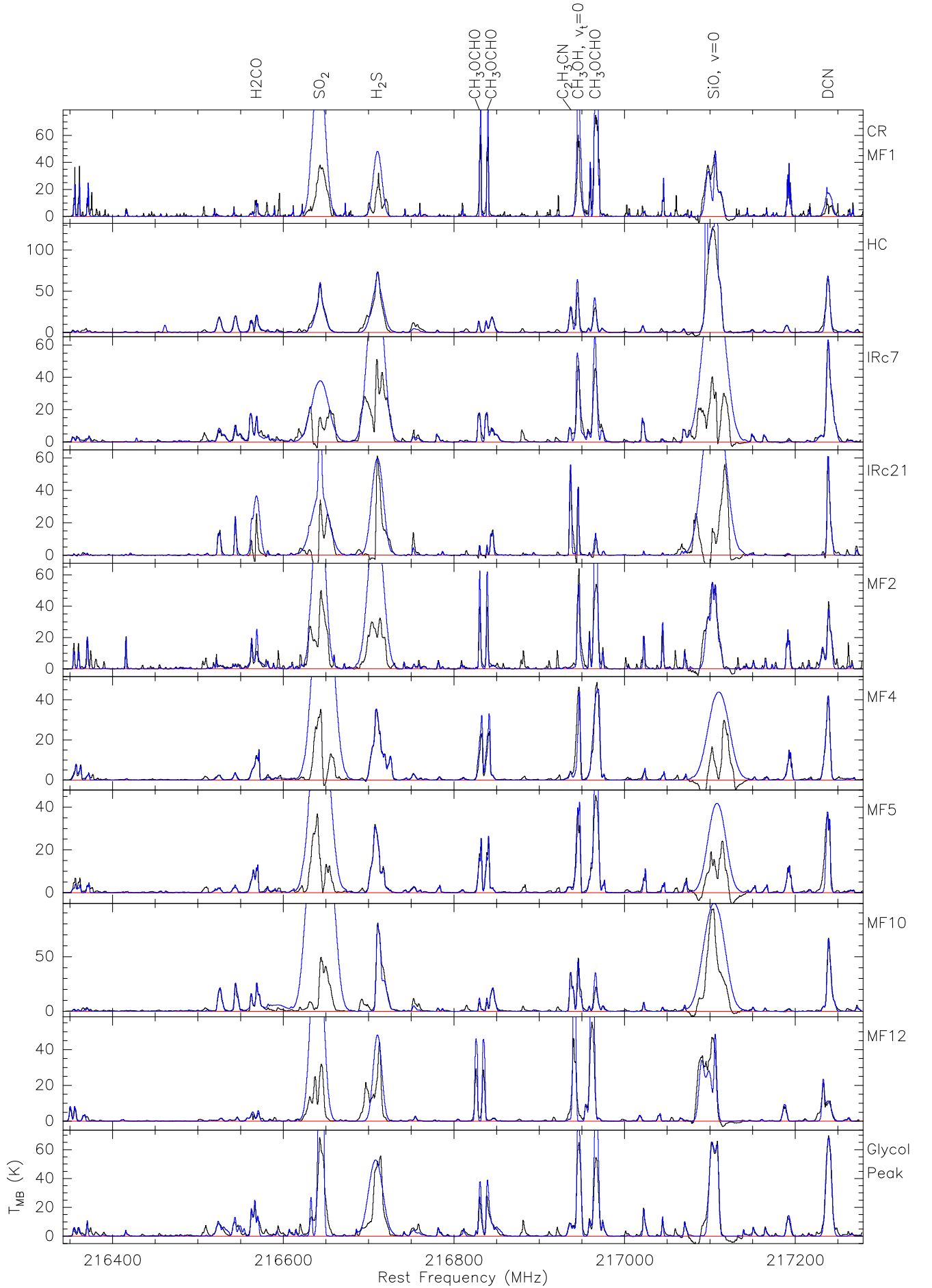


Fig. A.3b. Spectra from the band 2 setup for all ten sources with the summation of fits to individual species in blue.

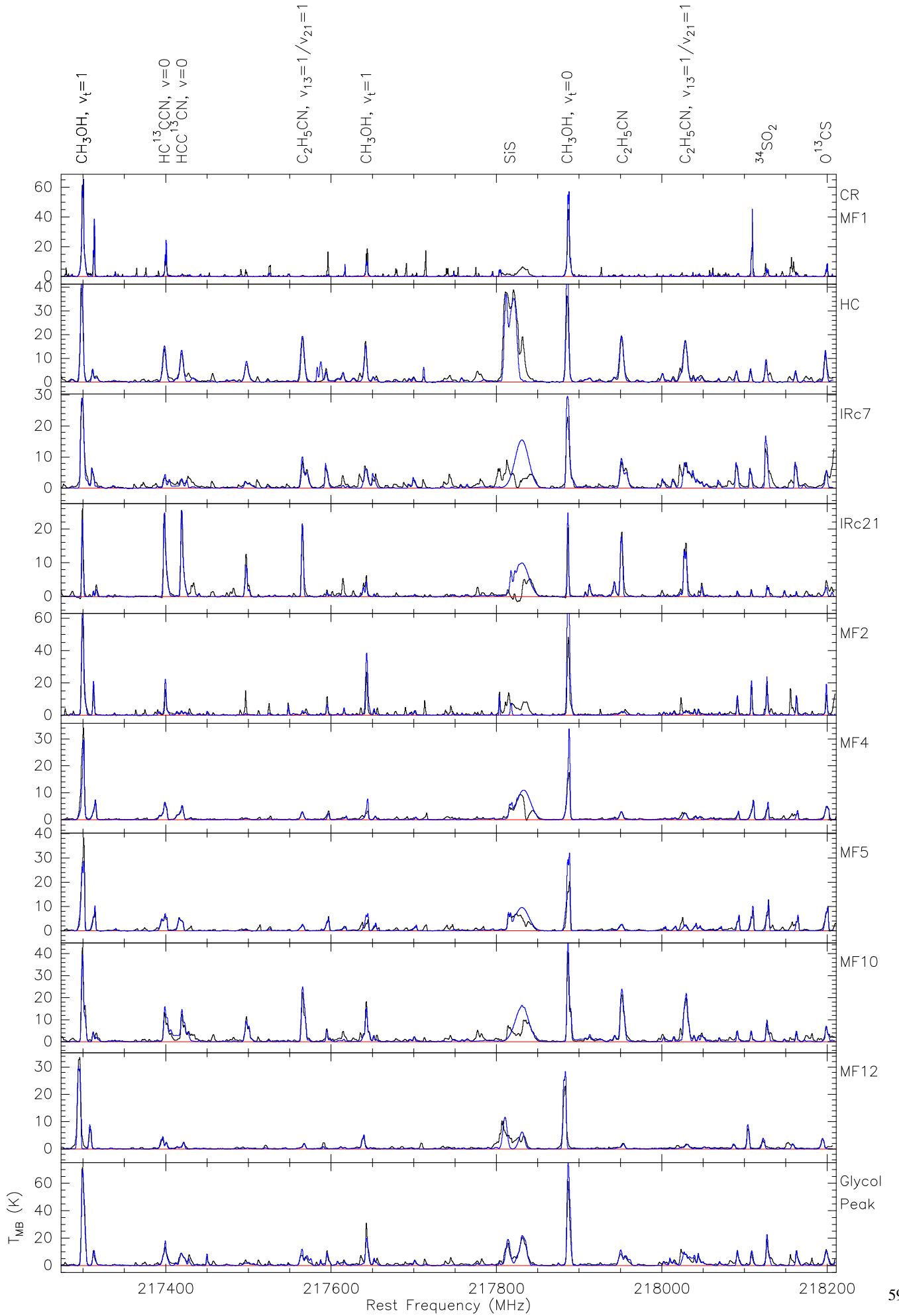


Fig. A.3c. Spectra from the band 3 setup for all ten sources with the summation of fits to individual species in blue.

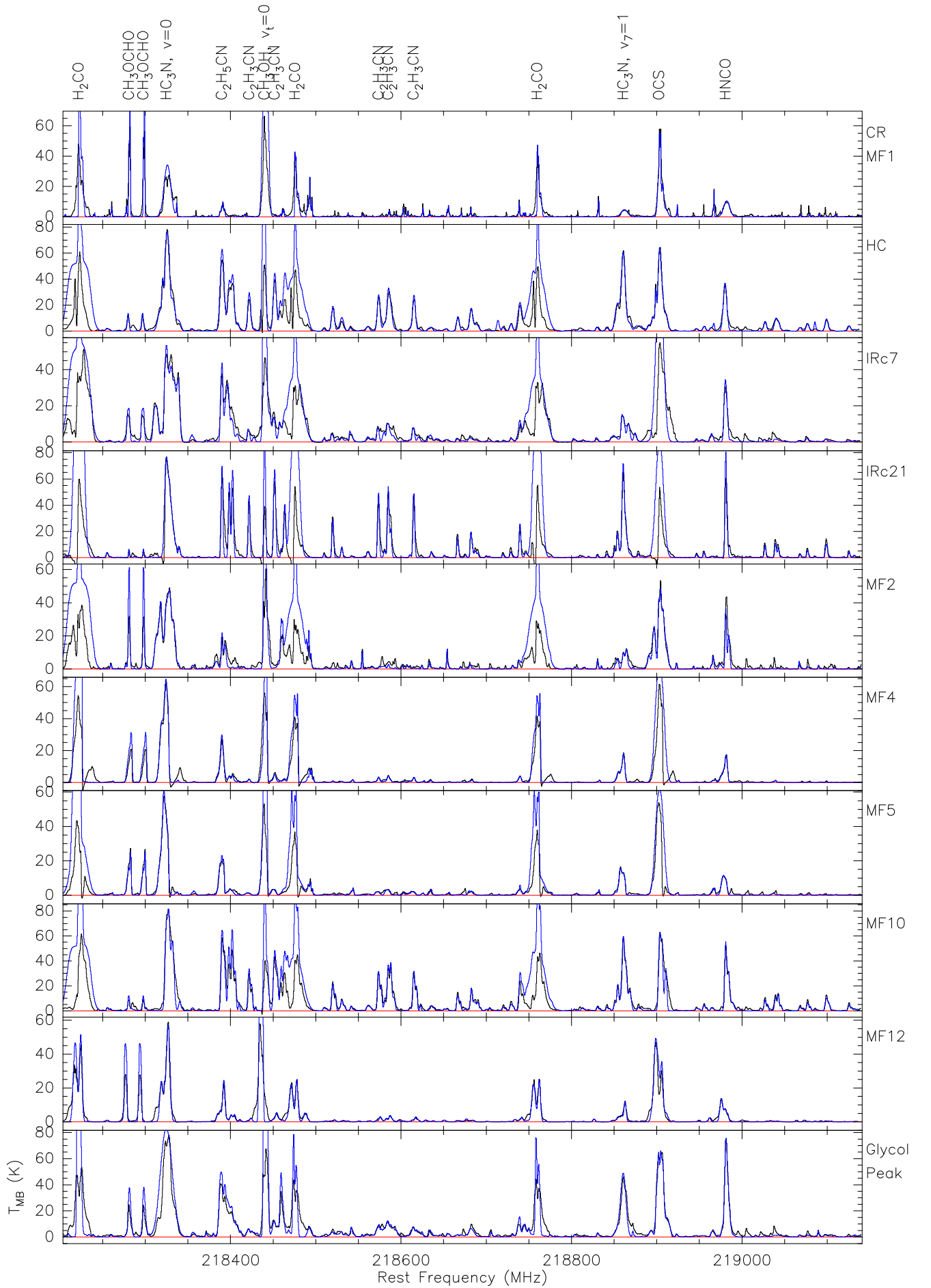


Fig. A.3d. Spectra from the band 4 setup for all ten sources with the summation of fits to individual species in blue.

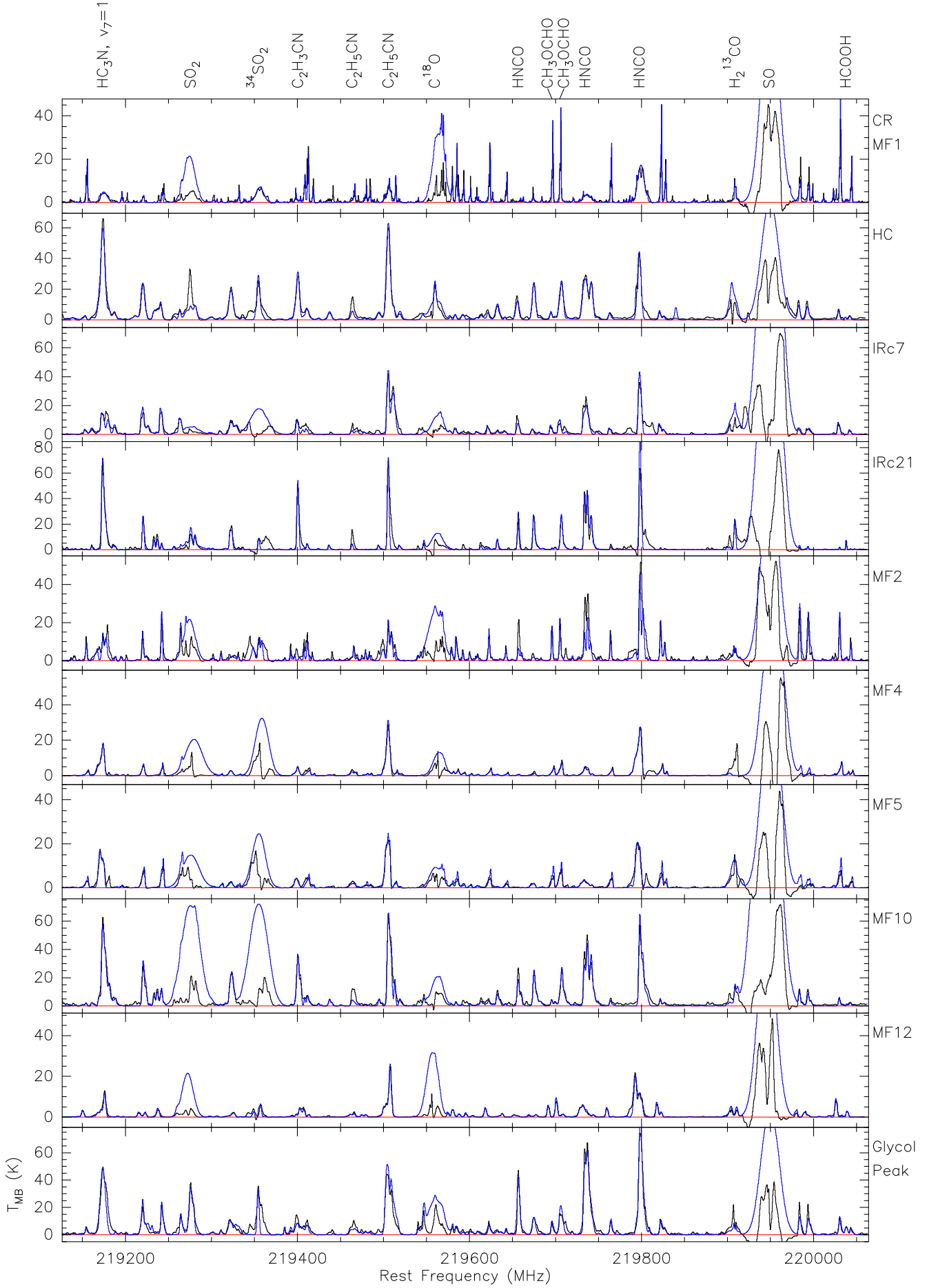


Fig. A.3e. Spectra from the band 5 setup for all ten sources with the summation of fits to individual species in blue. A ~ 250 MHz overlap with Fig A.3f is present, due to an incorrect setup.

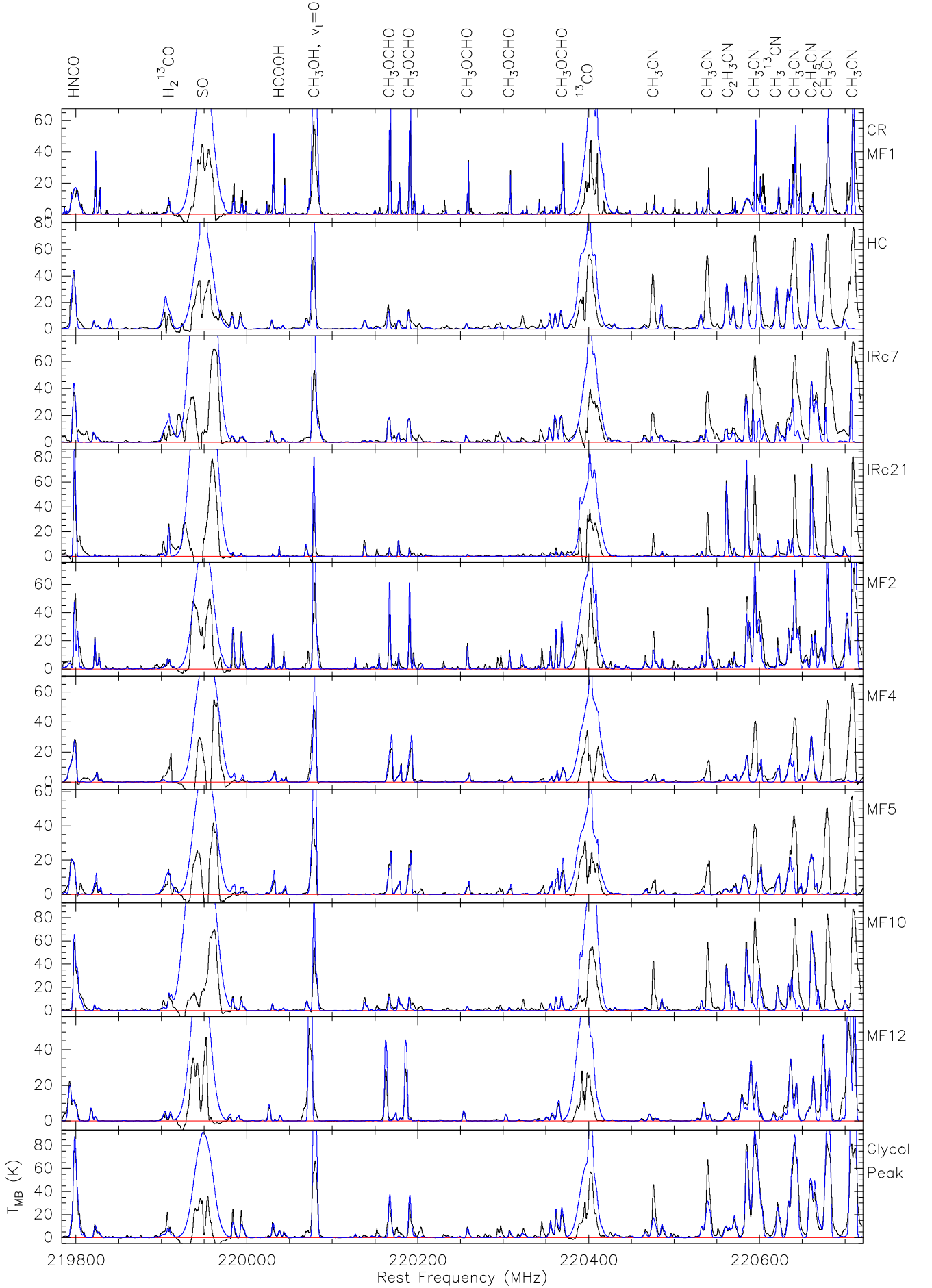


Fig. A.3f. Spectra from the band 6 setup for all ten sources with the summation of fits to individual species in blue except for CH_3CN which must be fitted with a non-LTE model and is therefore not added here (see Sect.4.3).

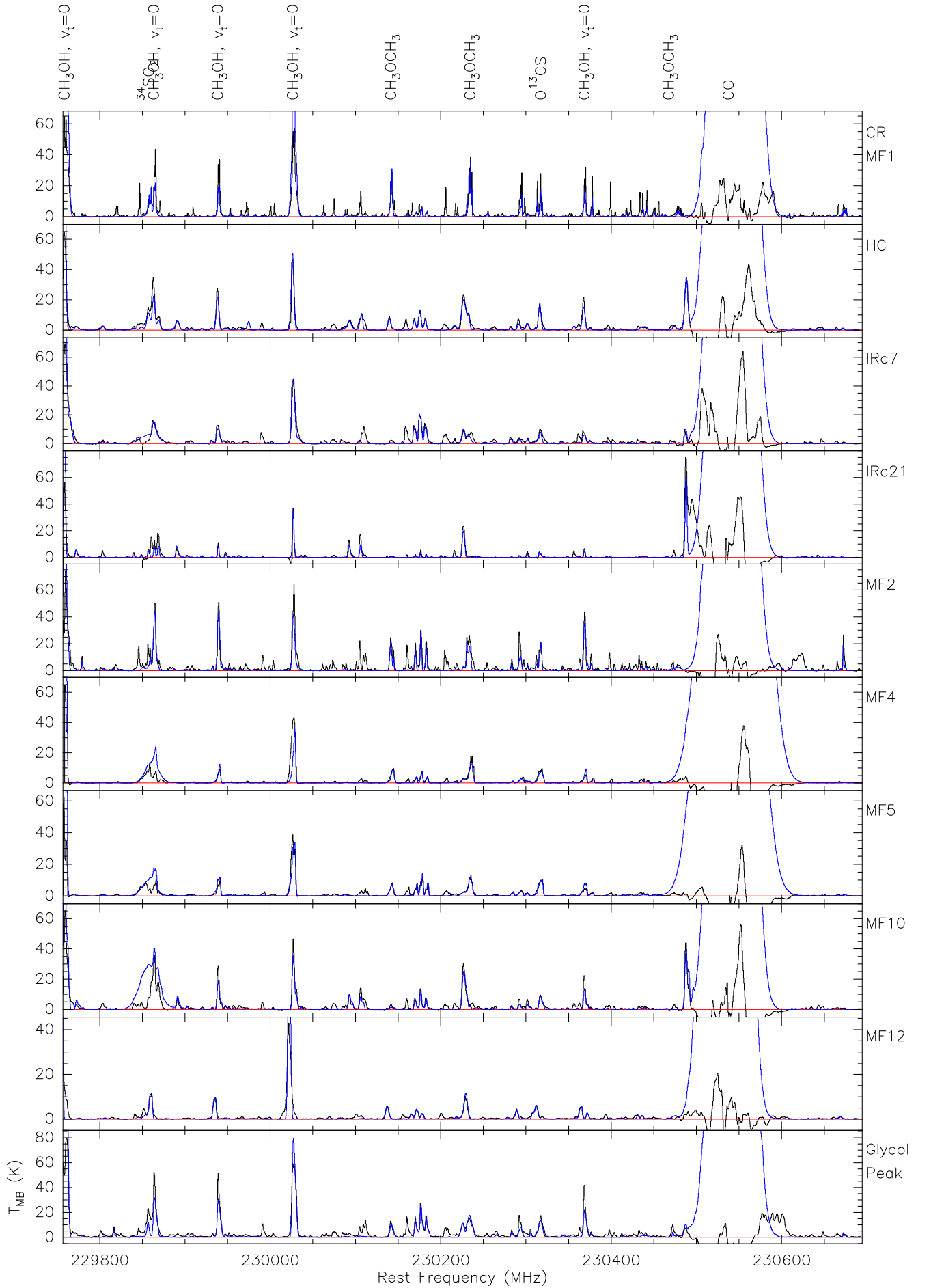


Fig. A.3g. Spectra from the band 7 setup for all ten sources.

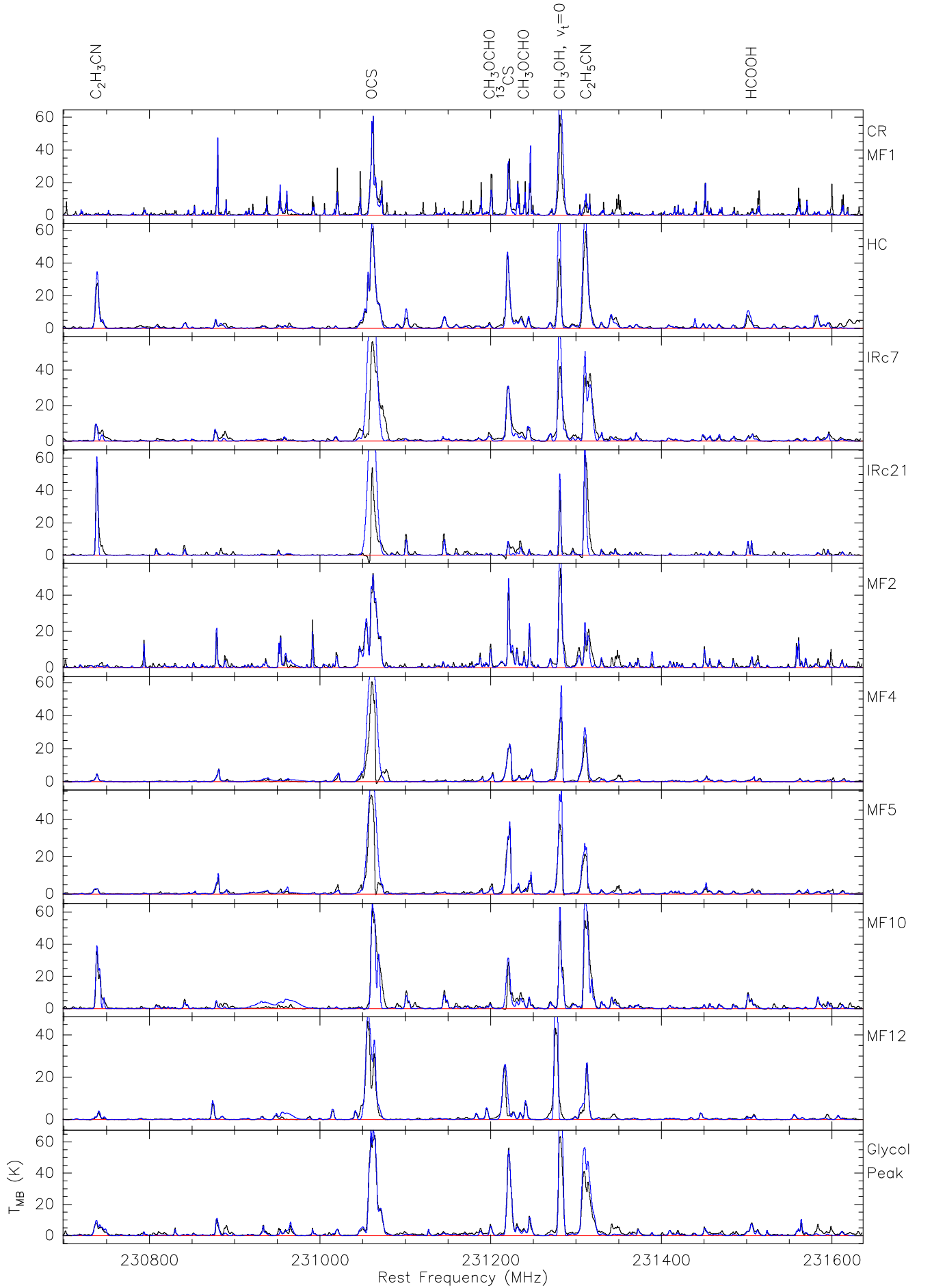


Fig. A.3h. Spectra from the band 8 setup for all ten sources with the summation of fits to individual species in blue.

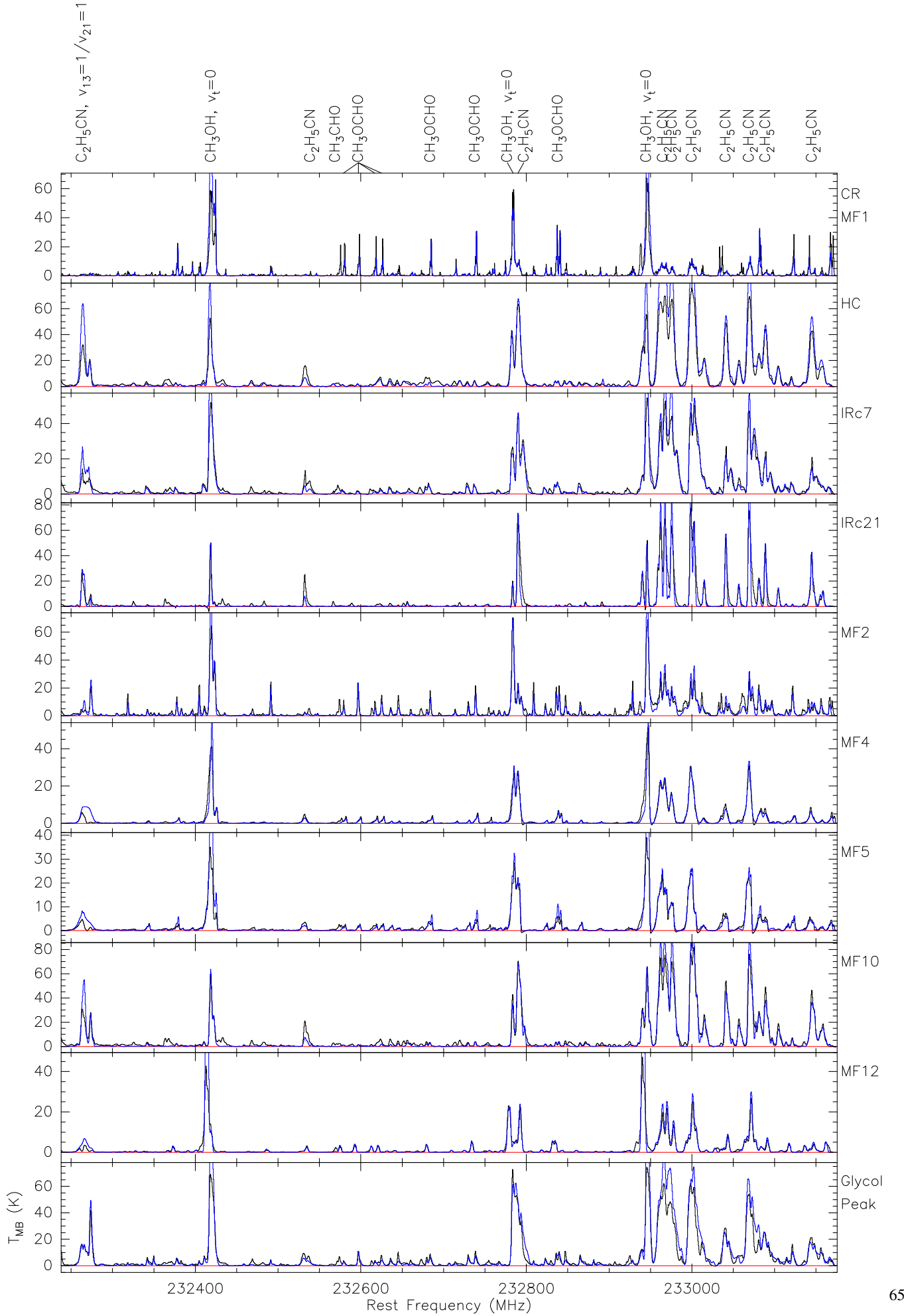


Fig. A.3i. Spectra from the band 9 setup for all ten sources with the summation of fits to individual species in blue.

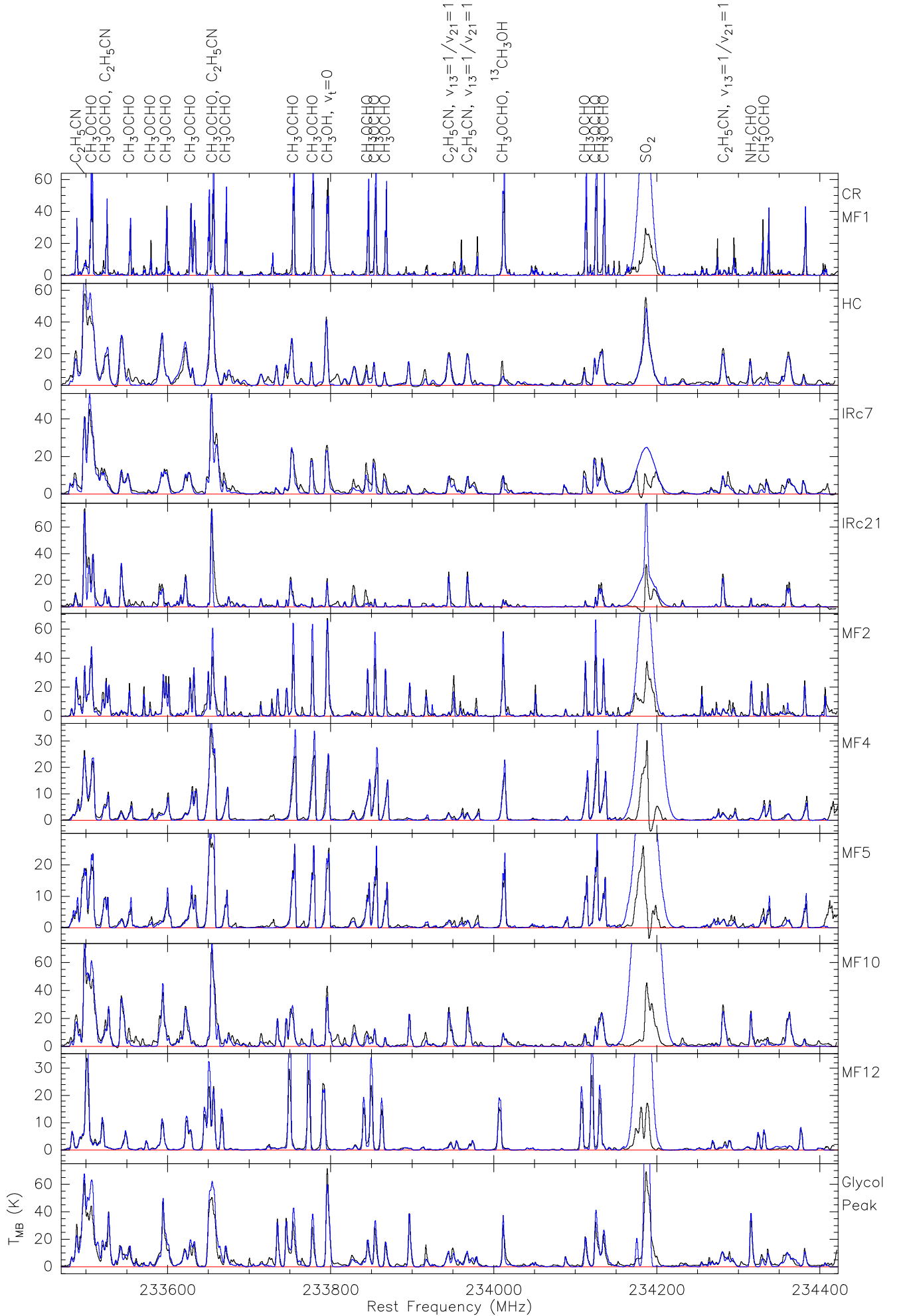


Fig. A.3j. Spectra from the band 10 setup for all ten sources with the summation of fits to individual species in blue.

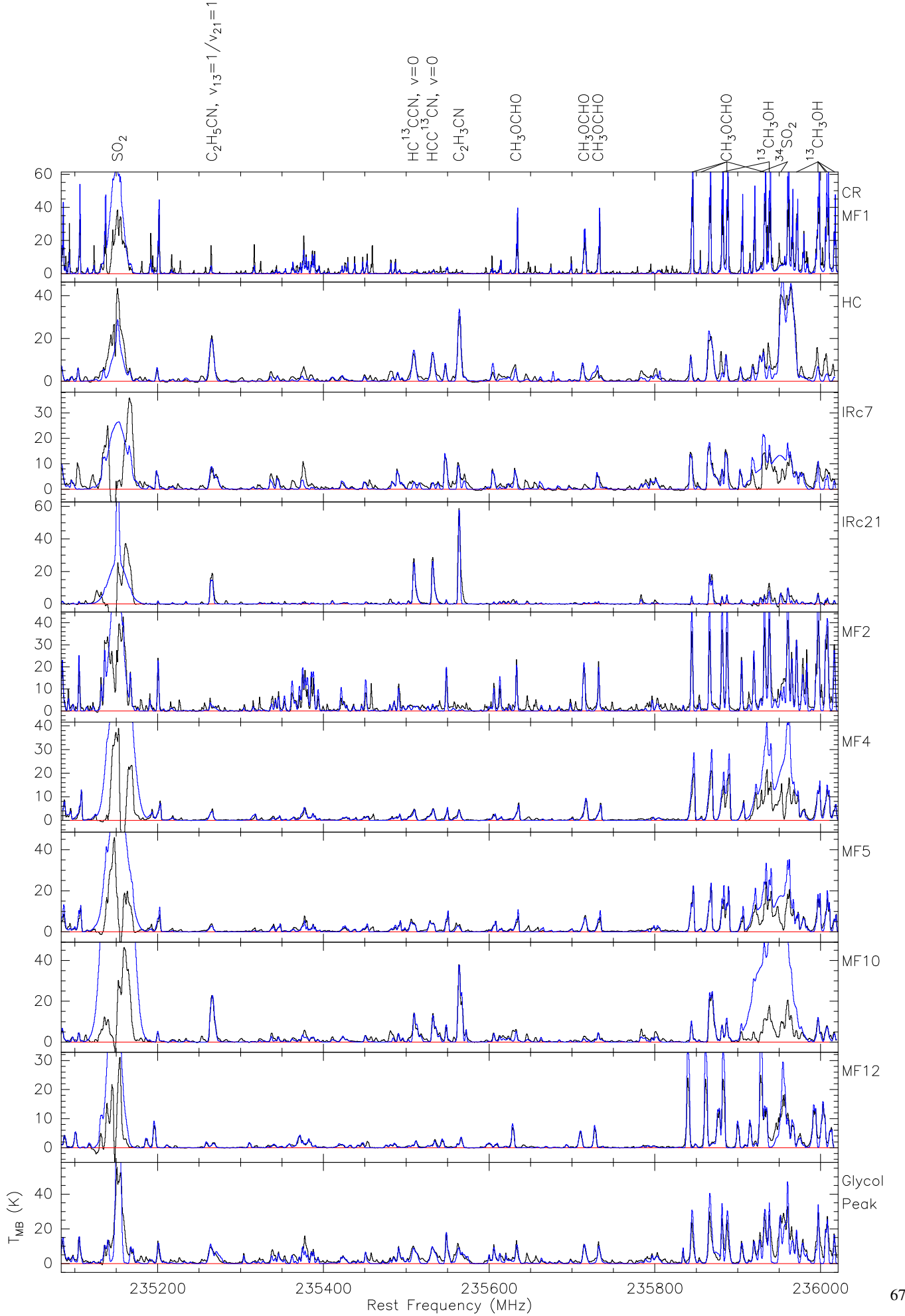


Fig. A.3k. Spectra from the band 11 setup for all ten sources with the summation of fits to individual species in blue.

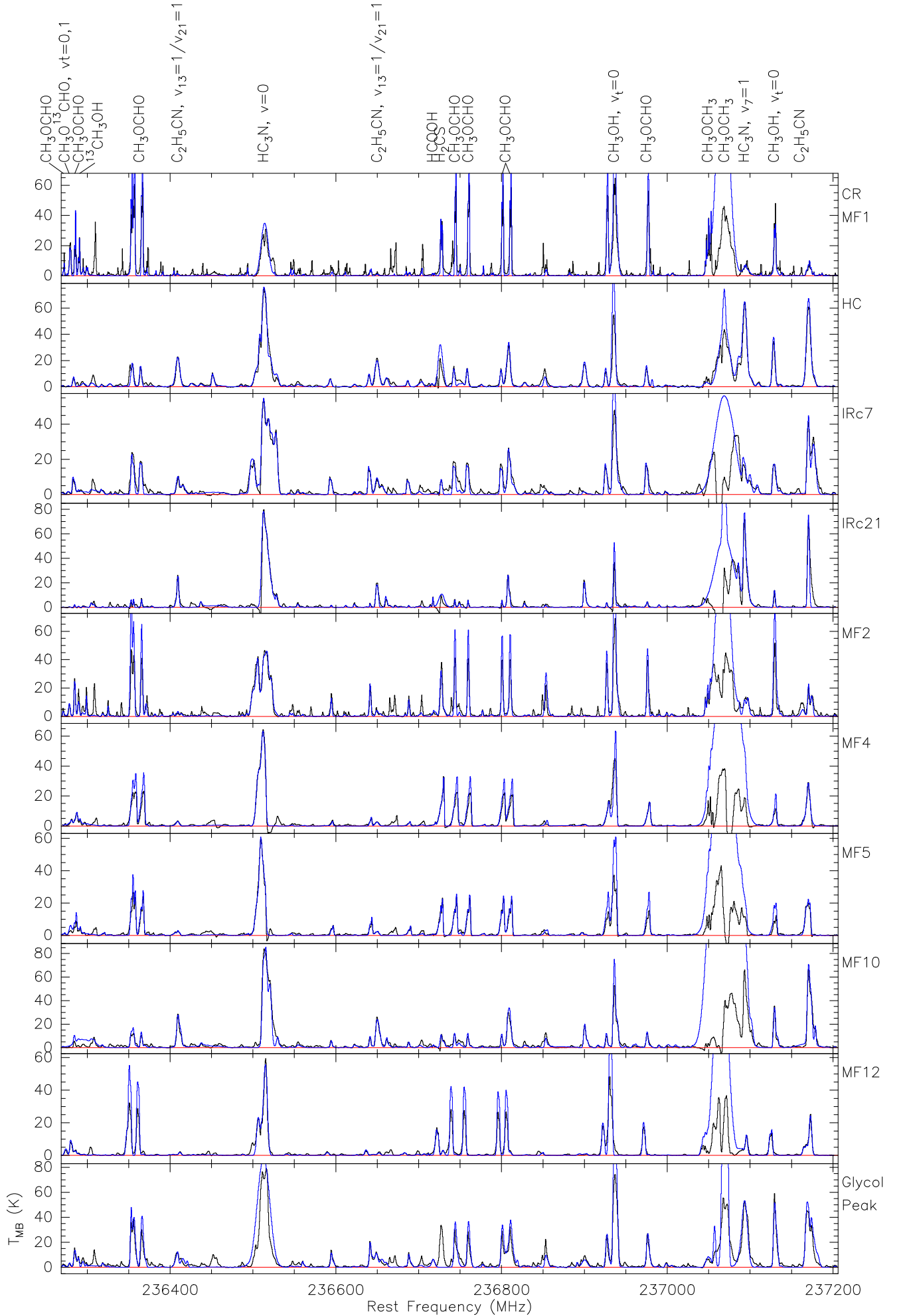


Fig. A.31. Spectra from the band 12 setup for all ten sources with the summation of fits to individual species in blue.

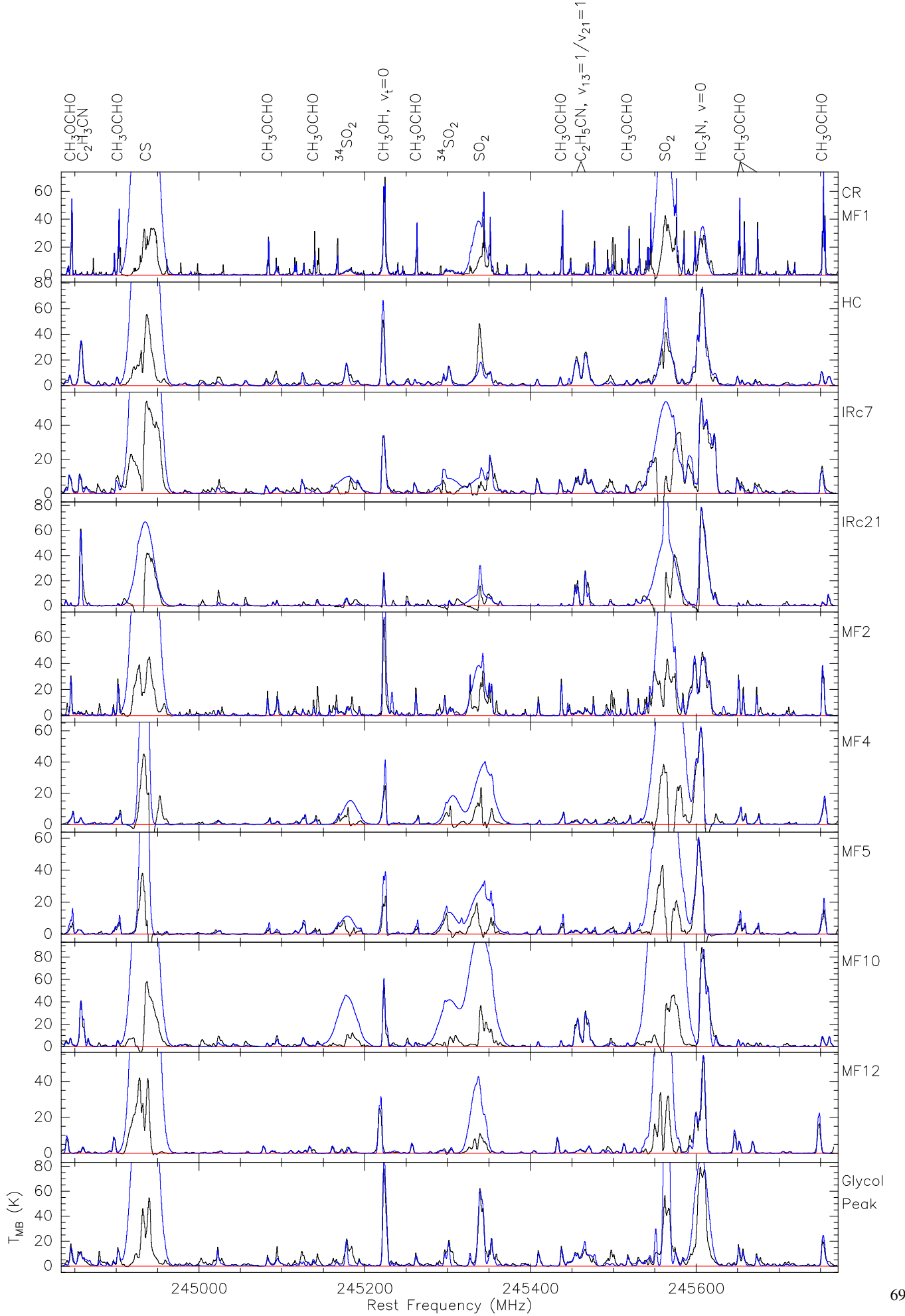


Fig. A.3m. Spectra from the band 13 setup for all ten sources with the summation of fits to individual species in blue.

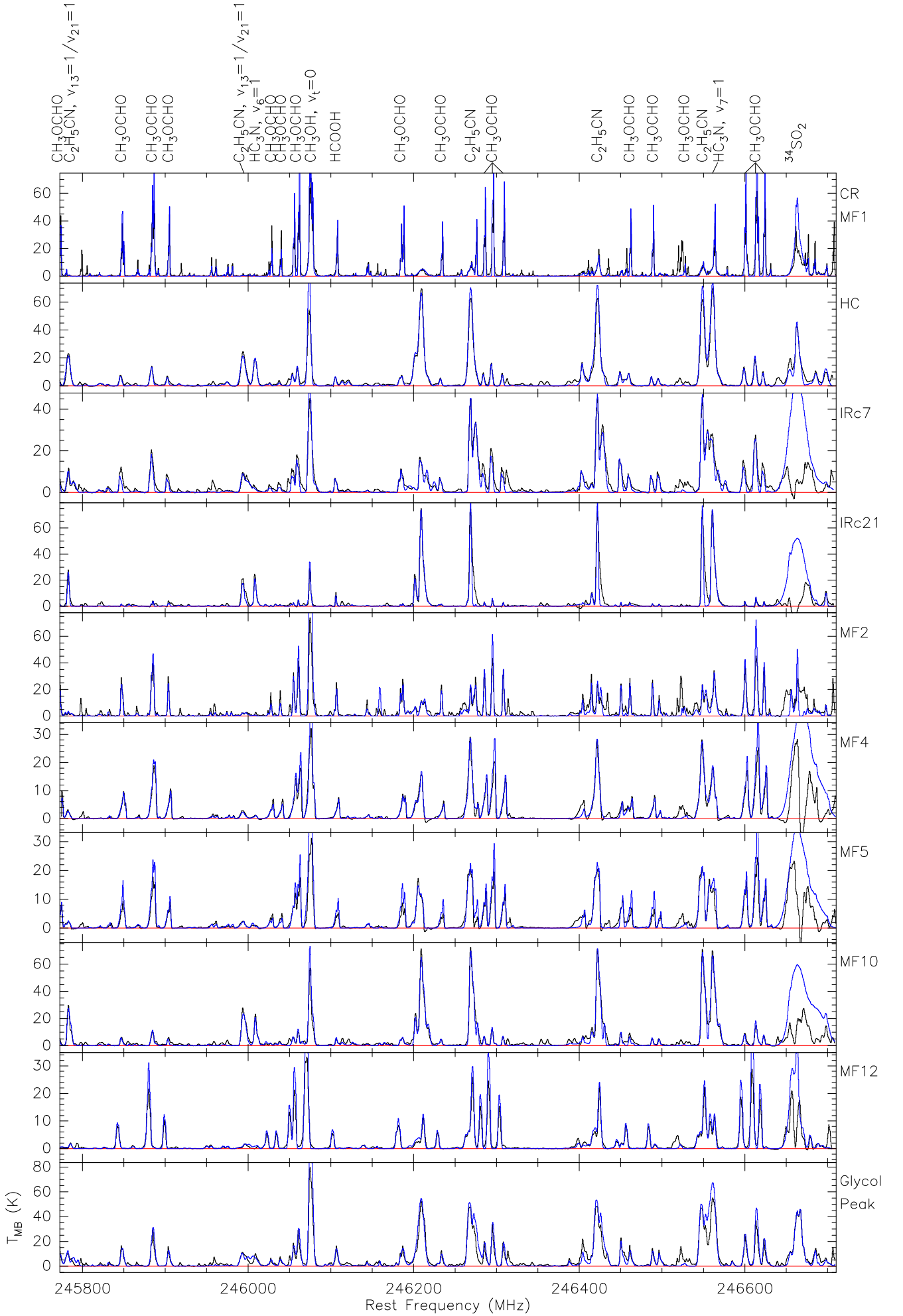


Fig. A.3n. Spectra from the band 14 setup for all ten sources with the summation of fits to individual species in blue.

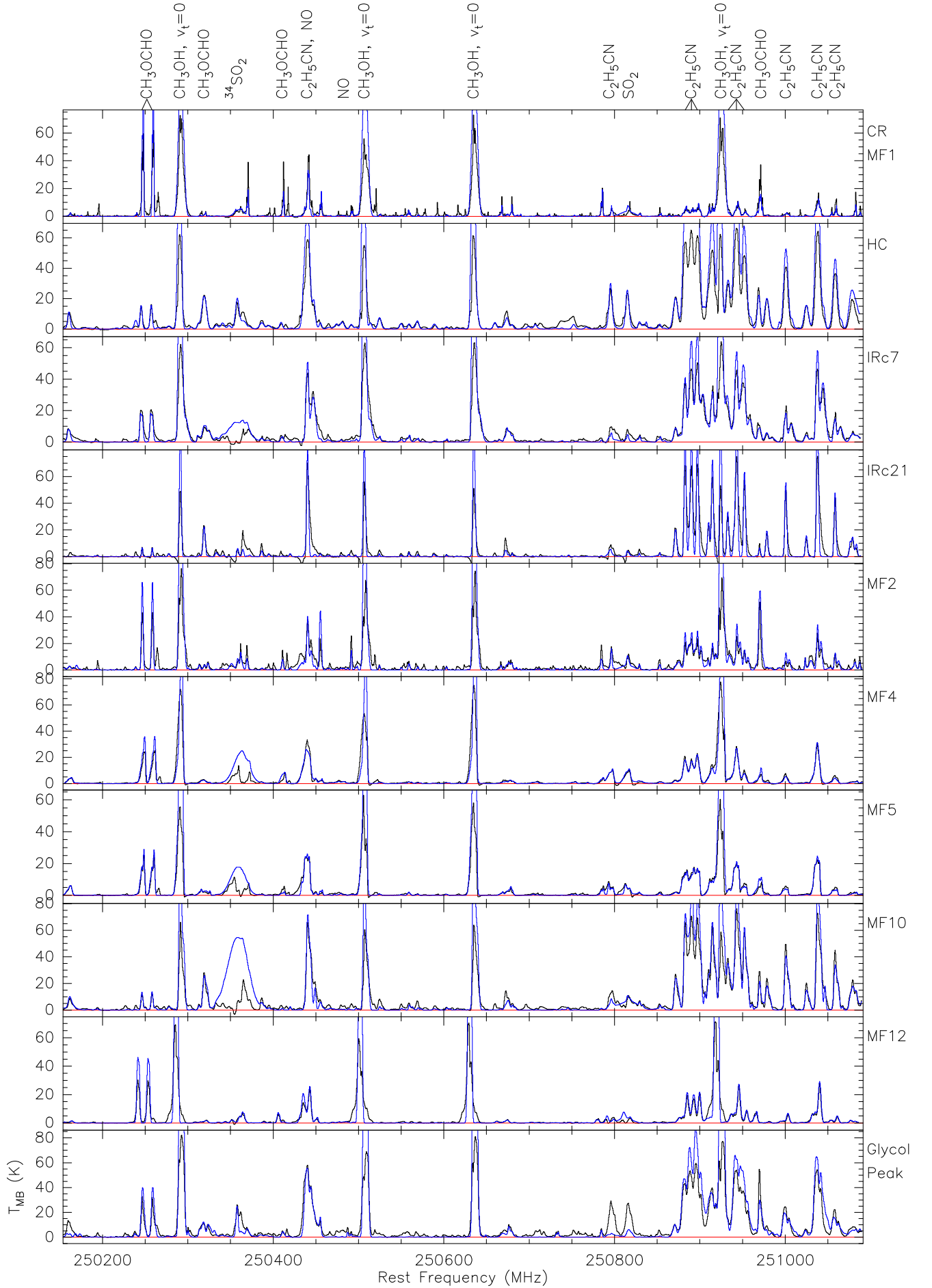


Fig. A.30. Spectra from the band 15 setup for all ten sources with the summation of fits to individual species in blue.

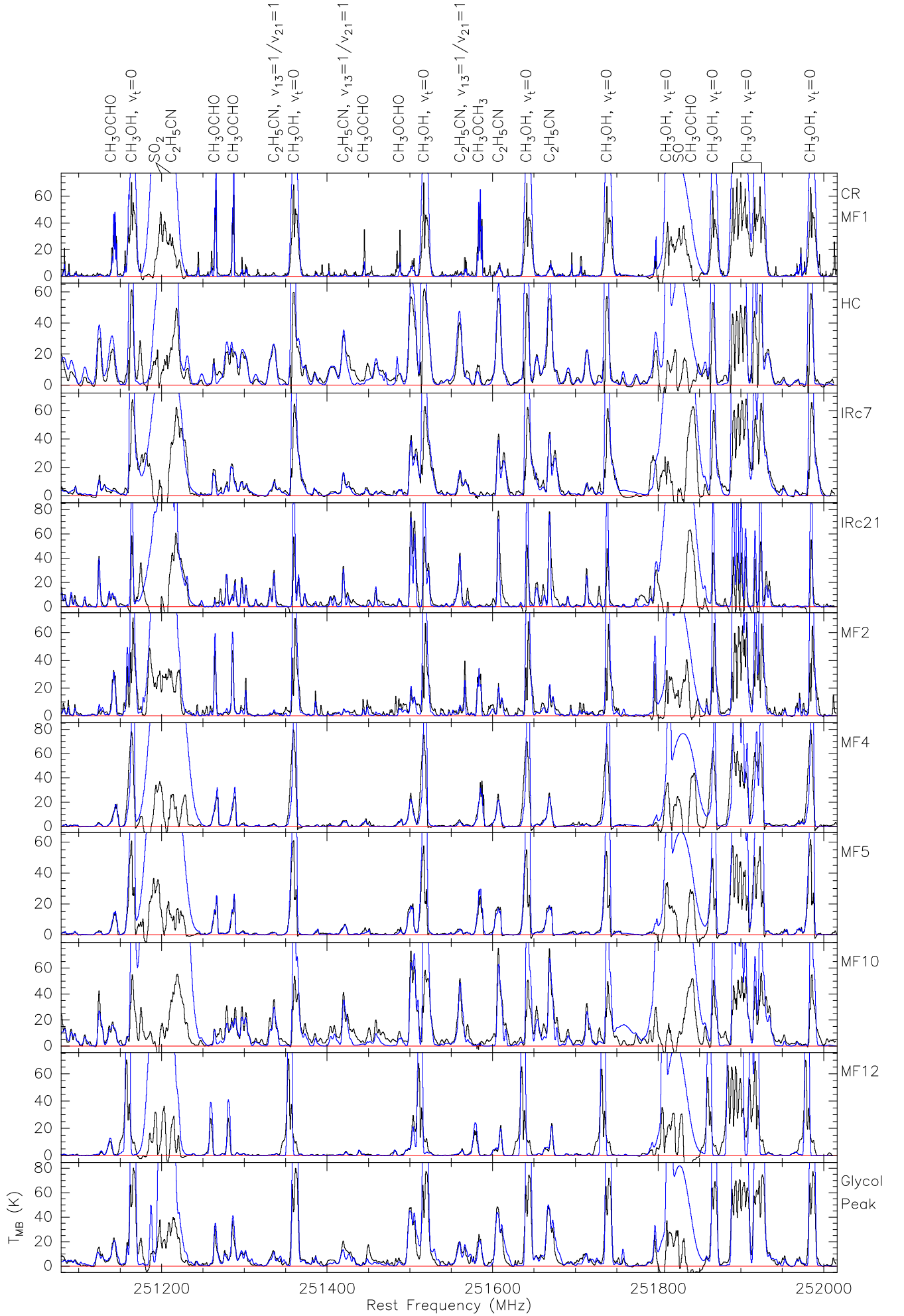


Fig. A.3p. Spectra from the band 16 setup for all ten sources with the summation of fits to individual species in blue.

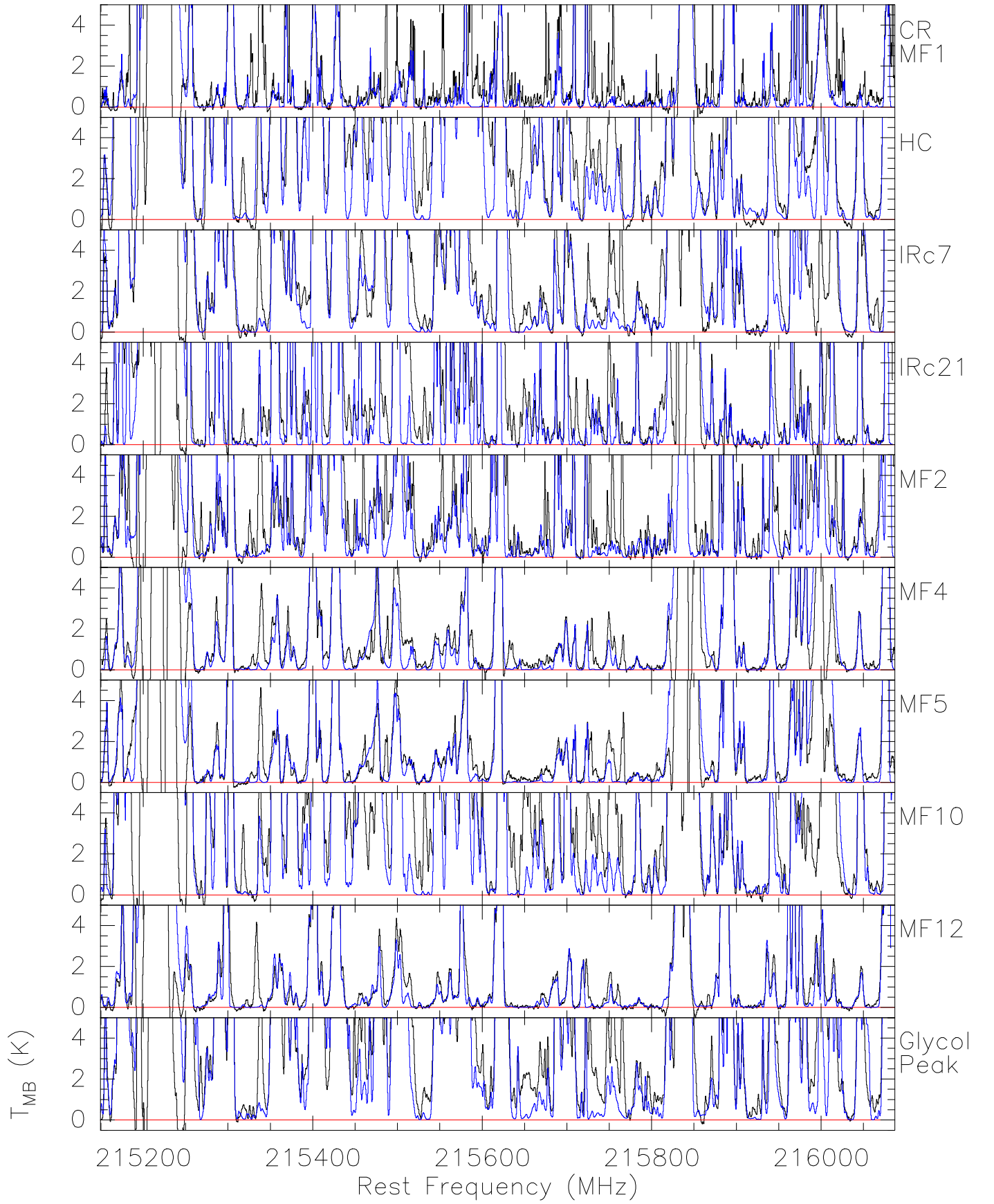


Fig. A.4a. Spectra from the band 1 setup for all ten sources with the summation of fits to individual species in blue and with a fixed maximum temperature scale of 5 K to highlight the weaker lines. The red line indicates the 0 K (continuum-removed) level.

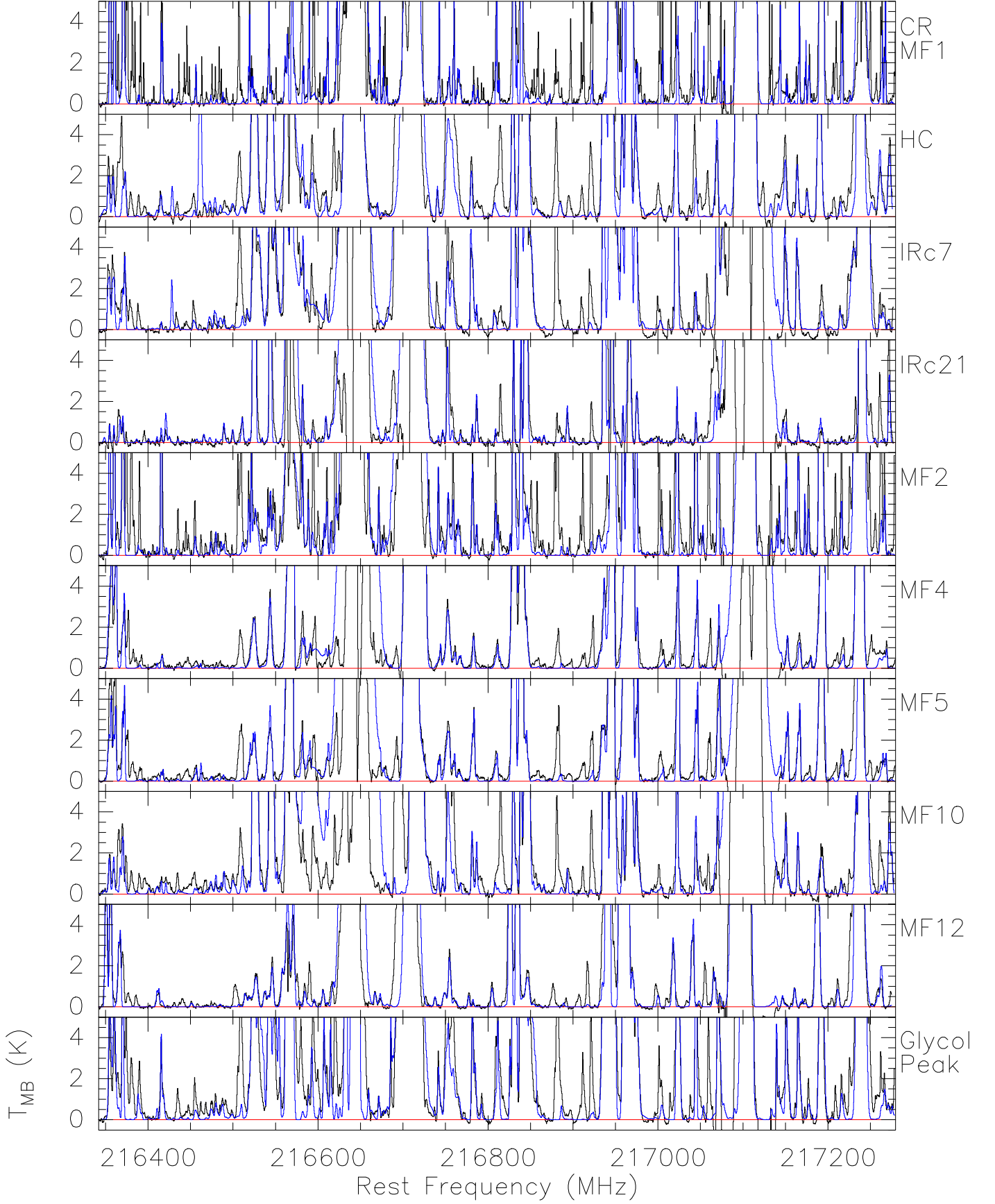


Fig. A.4b. Spectra from the band 2 setup for all ten sources with the summation of fits to individual species in blue and with a fixed maximum temperature scale of 5 K to highlight the weaker lines. The red line indicates the 0 K (continuum-removed) level.

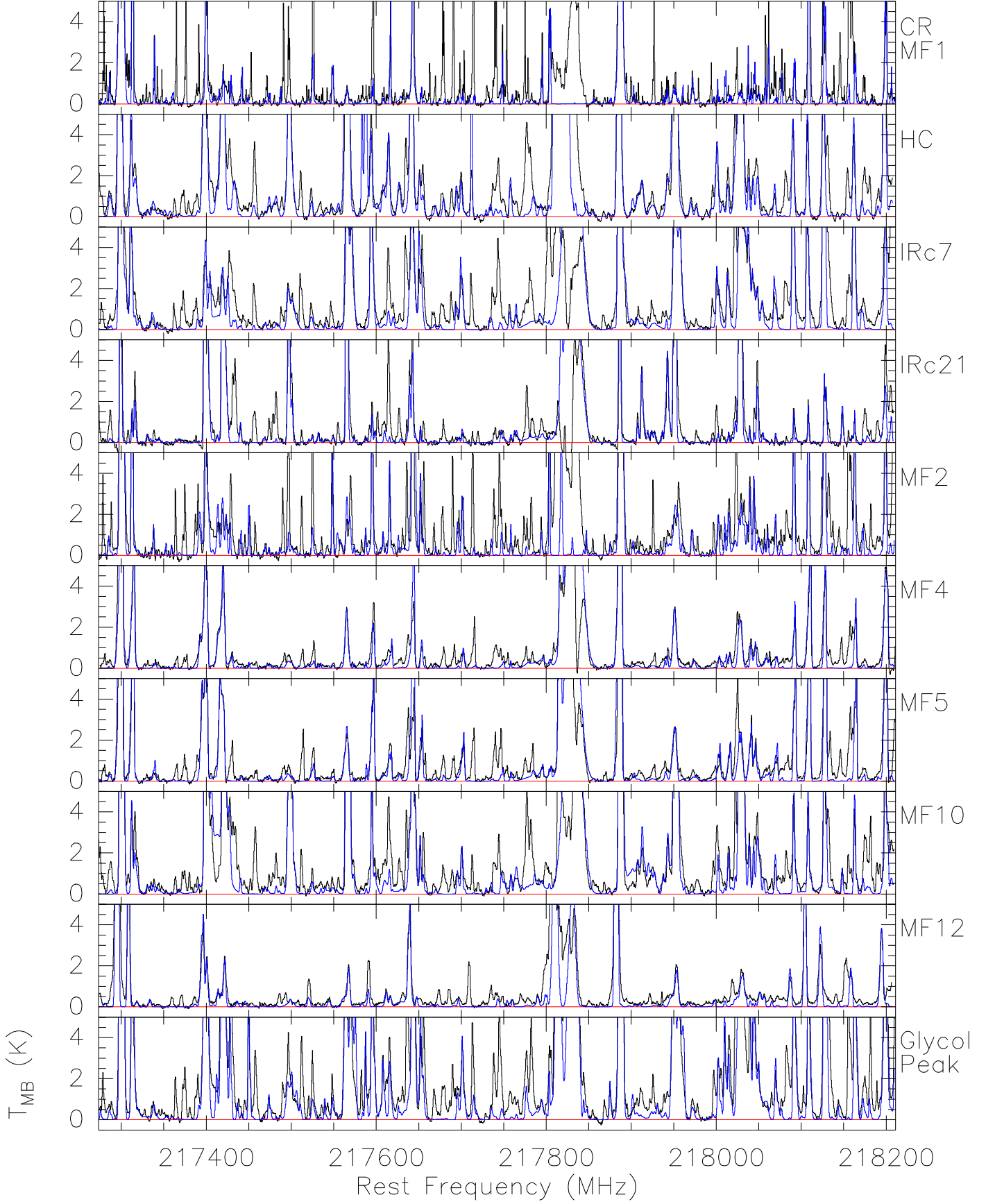


Fig. A.4c. Spectra from the band 3 setup for all ten sources with the summation of fits to individual species in blue and with a fixed maximum temperature scale of 5 K to highlight the weaker lines. The red line indicates the 0 K (continuum-removed) level.

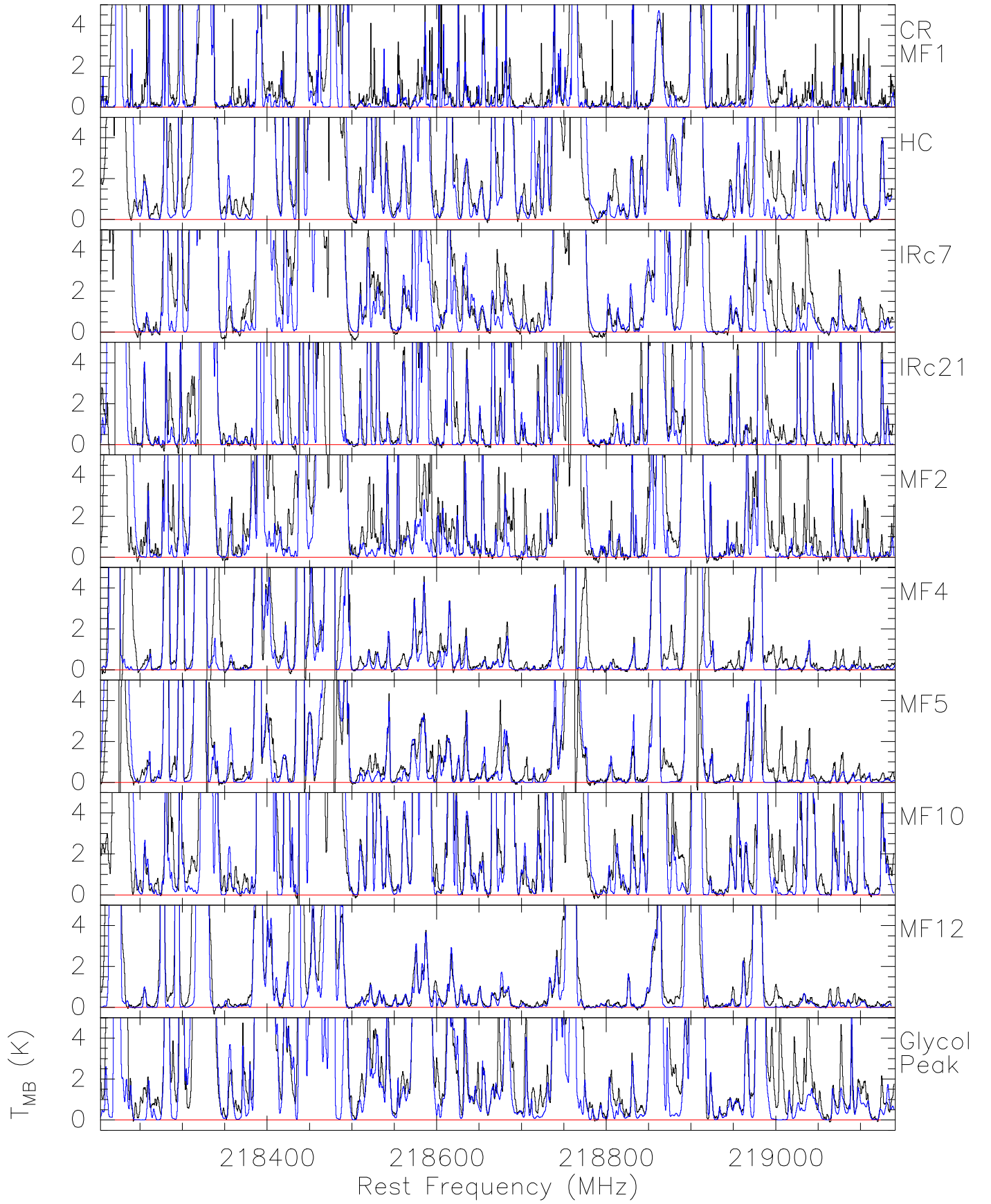


Fig. A.4d. Spectra from the band 4 setup for all ten sources with the summation of fits to individual species in blue and with a fixed maximum temperature scale of 5 K to highlight the weaker lines. The red line indicates the 0 K (continuum-removed) level.

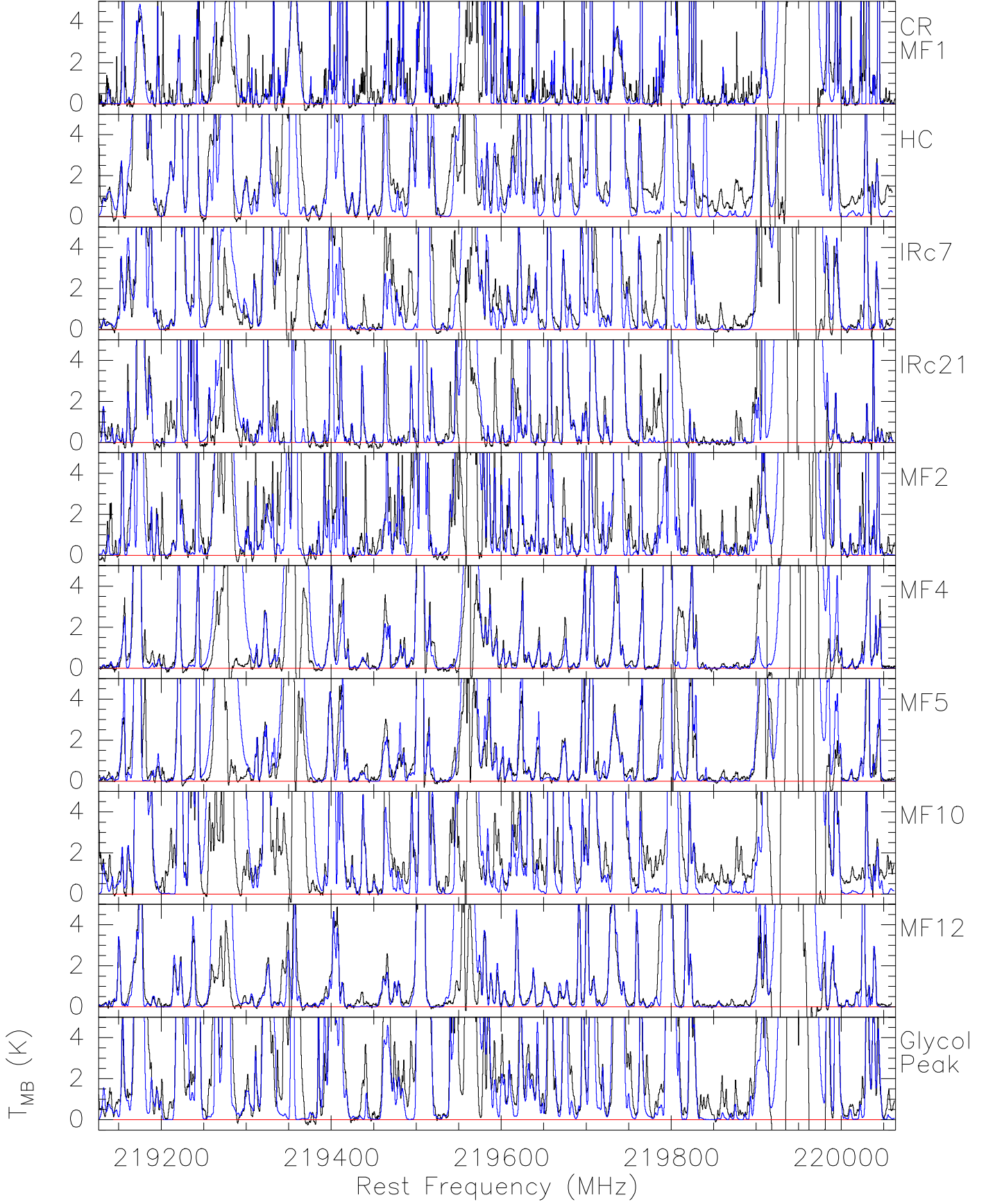


Fig. A.4e. Spectra from the band 5 setup for all ten sources with the summation of fits to individual species in blue and with a fixed maximum temperature scale of 5 K to highlight the weaker lines. CH_3CN is not included because it must be fitted with a non-LTE model and is therefore not added here (see Sect.4.3). A ~ 250 MHz overlap with Fig A.4f is present, due to an incorrect setup. The red line indicates the 0 K (continuum-removed) level.

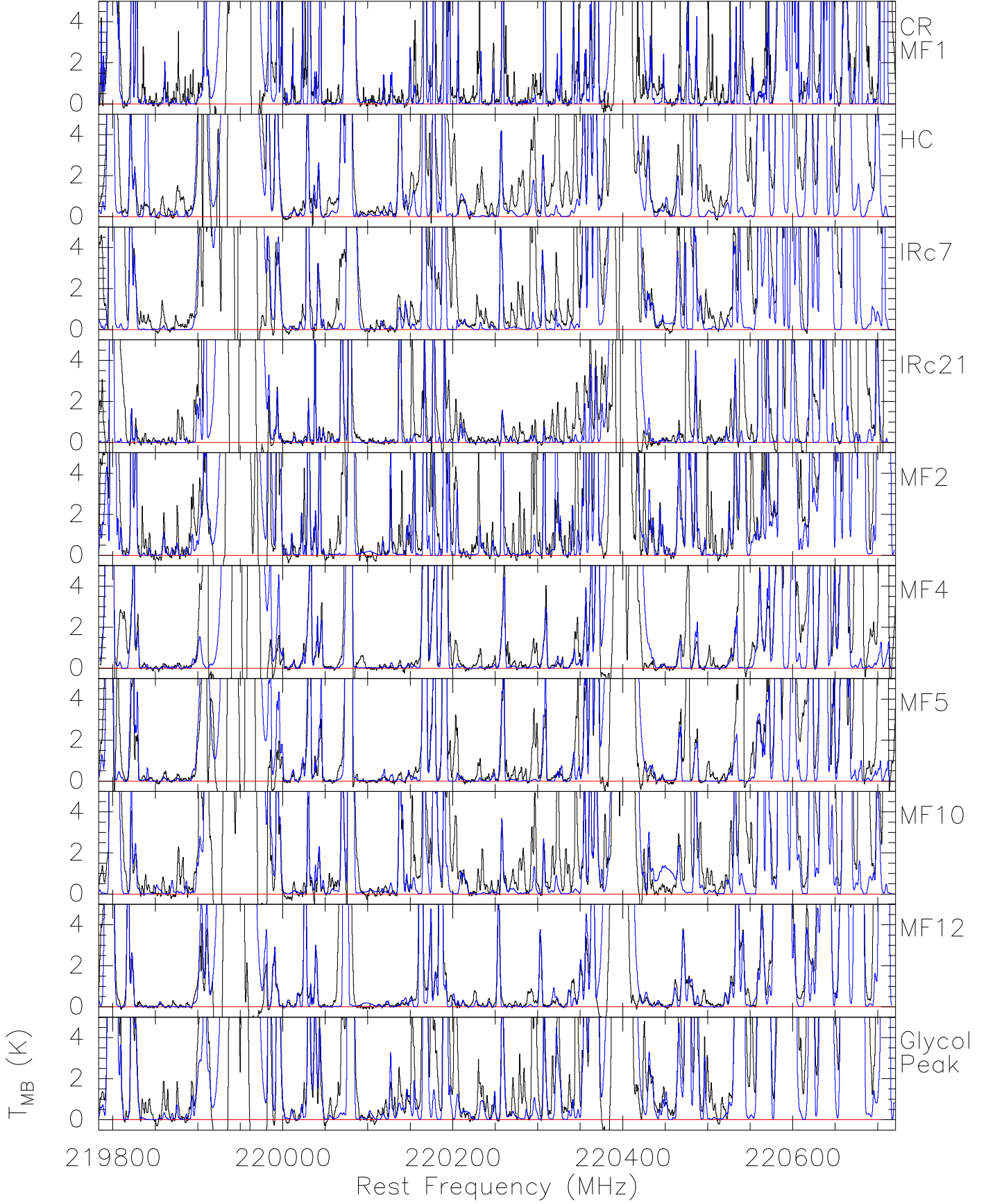


Fig. A.4f. Spectra from the band 6 setup for all ten sources with the summation of fits to individual species in blue and with a fixed maximum temperature scale of 5 K to highlight the weaker lines. The red line indicates the 0 K (continuum-removed) level.

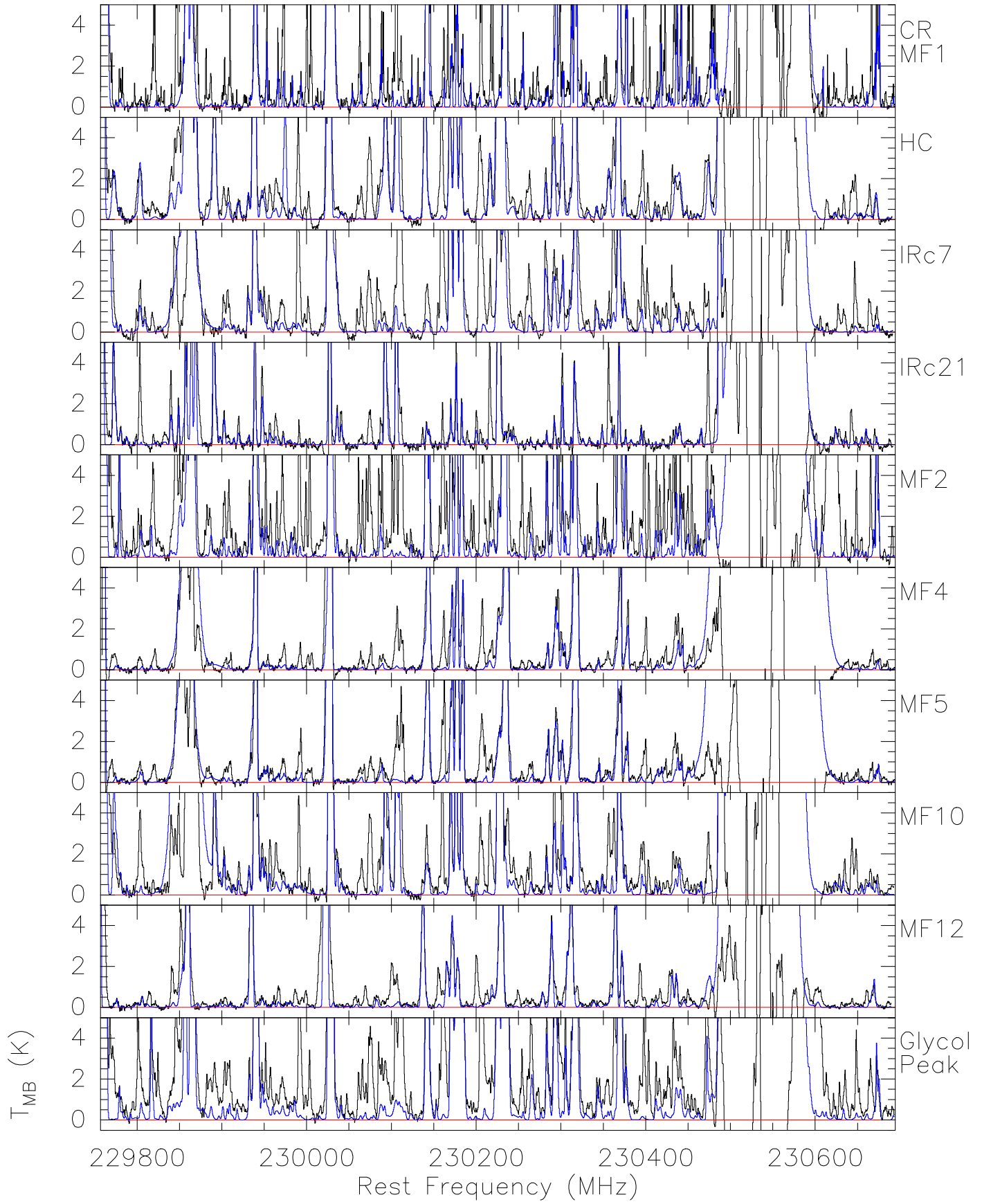


Fig. A.4g. Spectra from the band 7 setup for all ten sources with the summation of fits to individual species in blue and with a fixed maximum temperature scale of 5 K to highlight the weaker lines. The red line indicates the 0 K (continuum-removed) level.

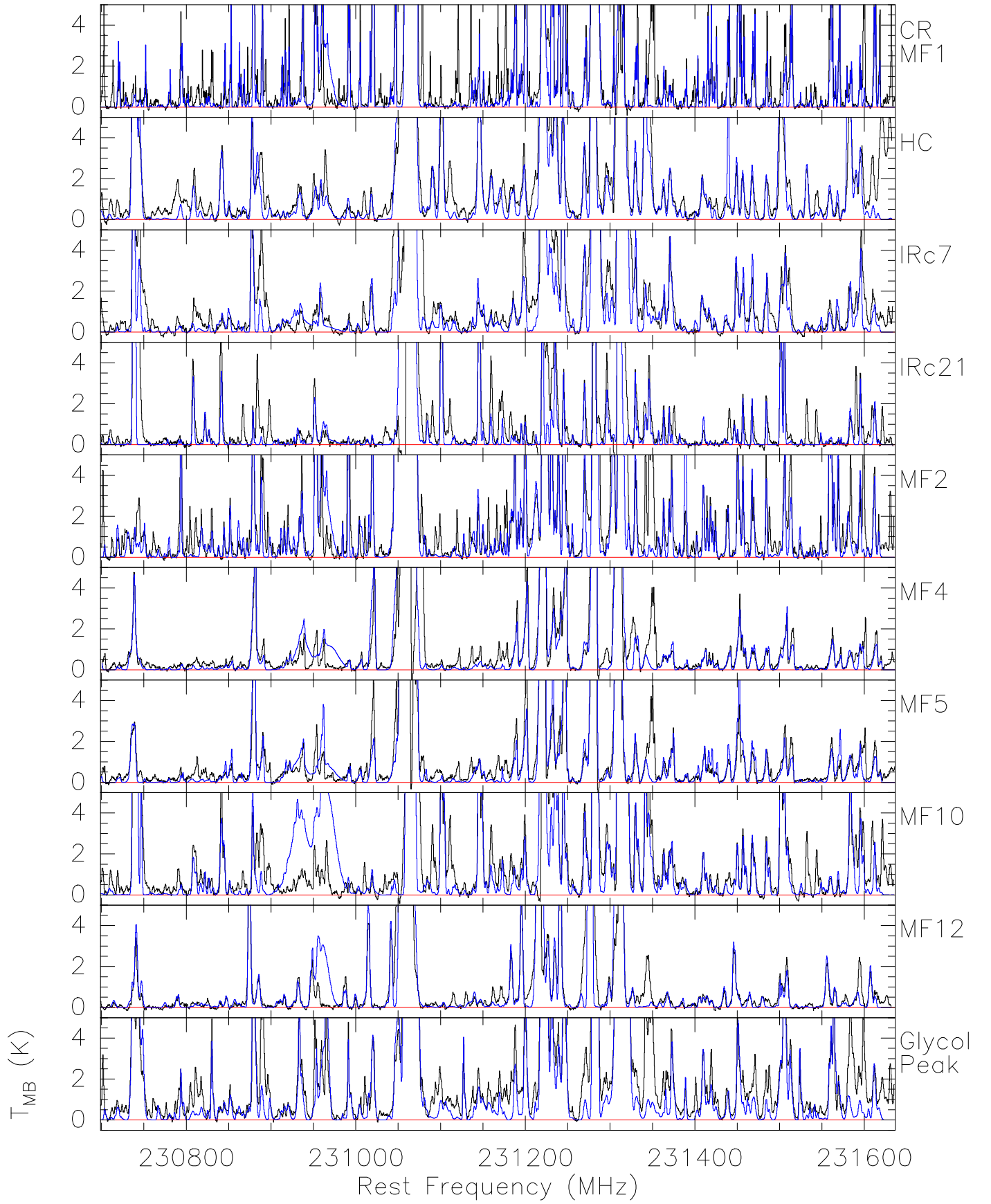


Fig. A.4h. Spectra from the band 8 setup for all ten sources with the summation of fits to individual species in blue and with a fixed maximum temperature scale of 5 K to highlight the weaker lines. The red line indicates the 0 K (continuum-removed) level.

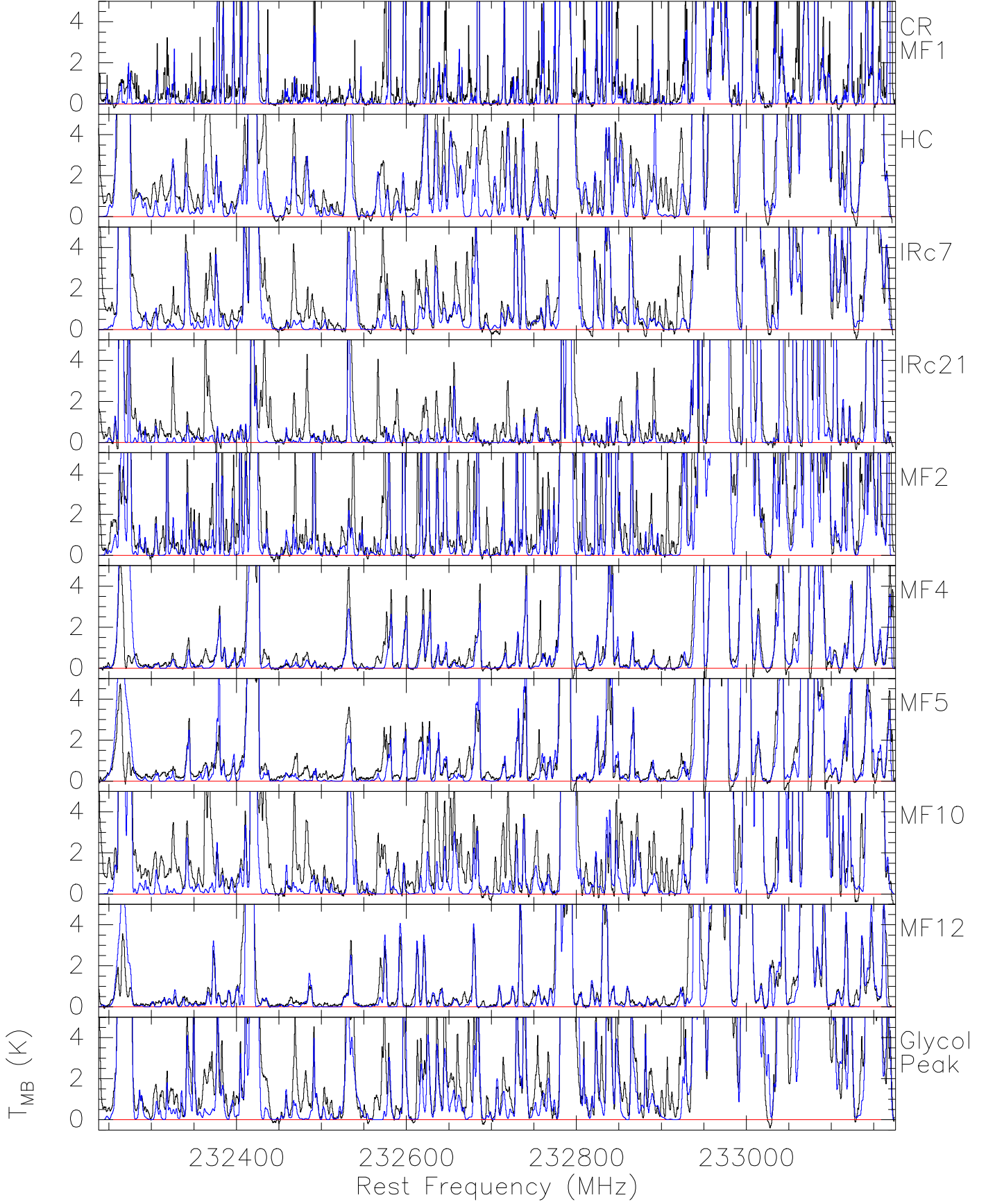


Fig. A.4i. Spectra from the band 9 setup for all ten sources with the summation of fits to individual species in blue and with a fixed maximum temperature scale of 5 K to highlight the weaker lines. The red line indicates the 0 K (continuum-removed) level.

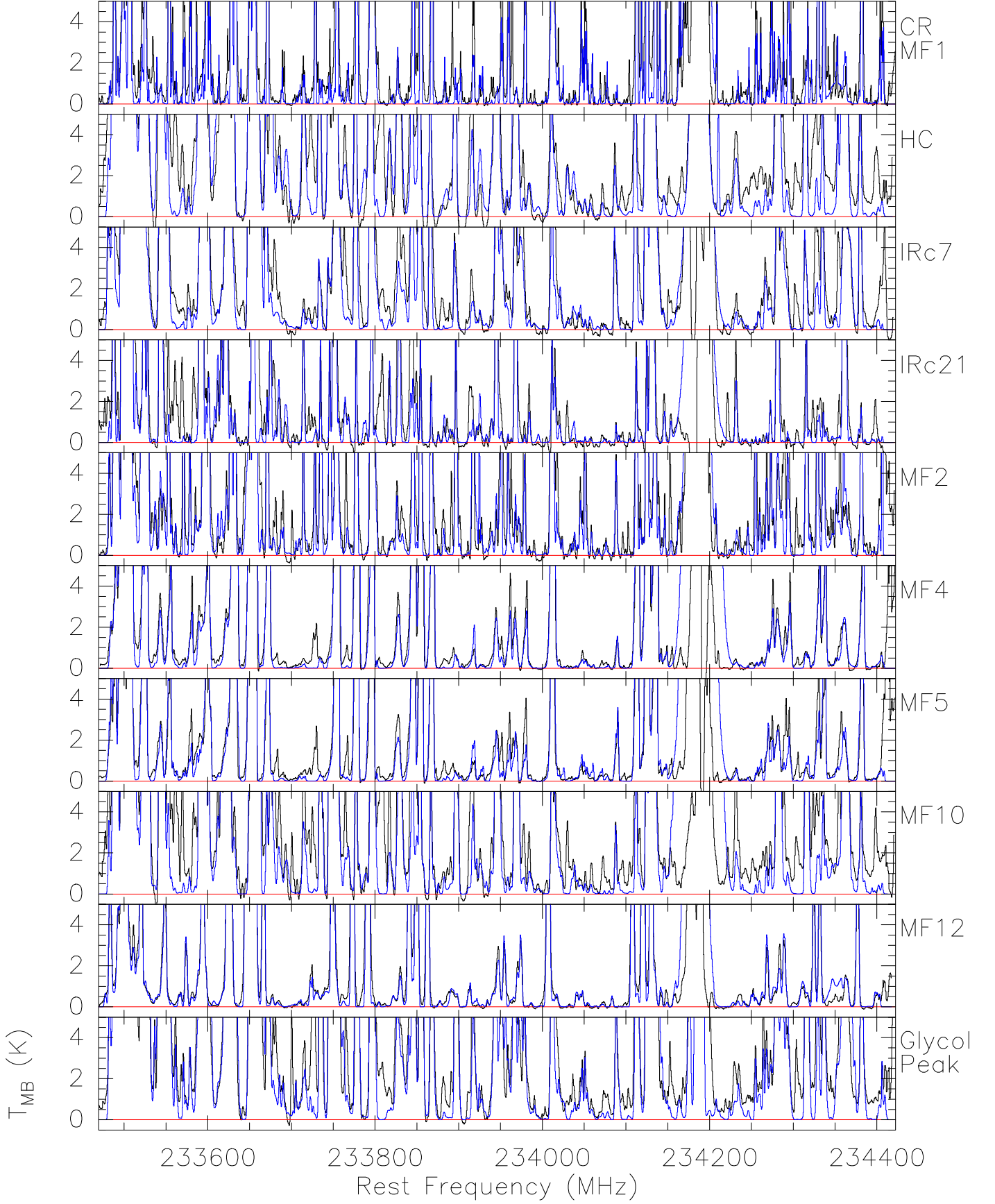


Fig. A.4j. Spectra from the band 10 setup for all ten sources with the summation of fits to individual species in blue and with a fixed maximum temperature scale of 5 K to highlight the weaker lines. The red line indicates the 0 K (continuum-removed) level.

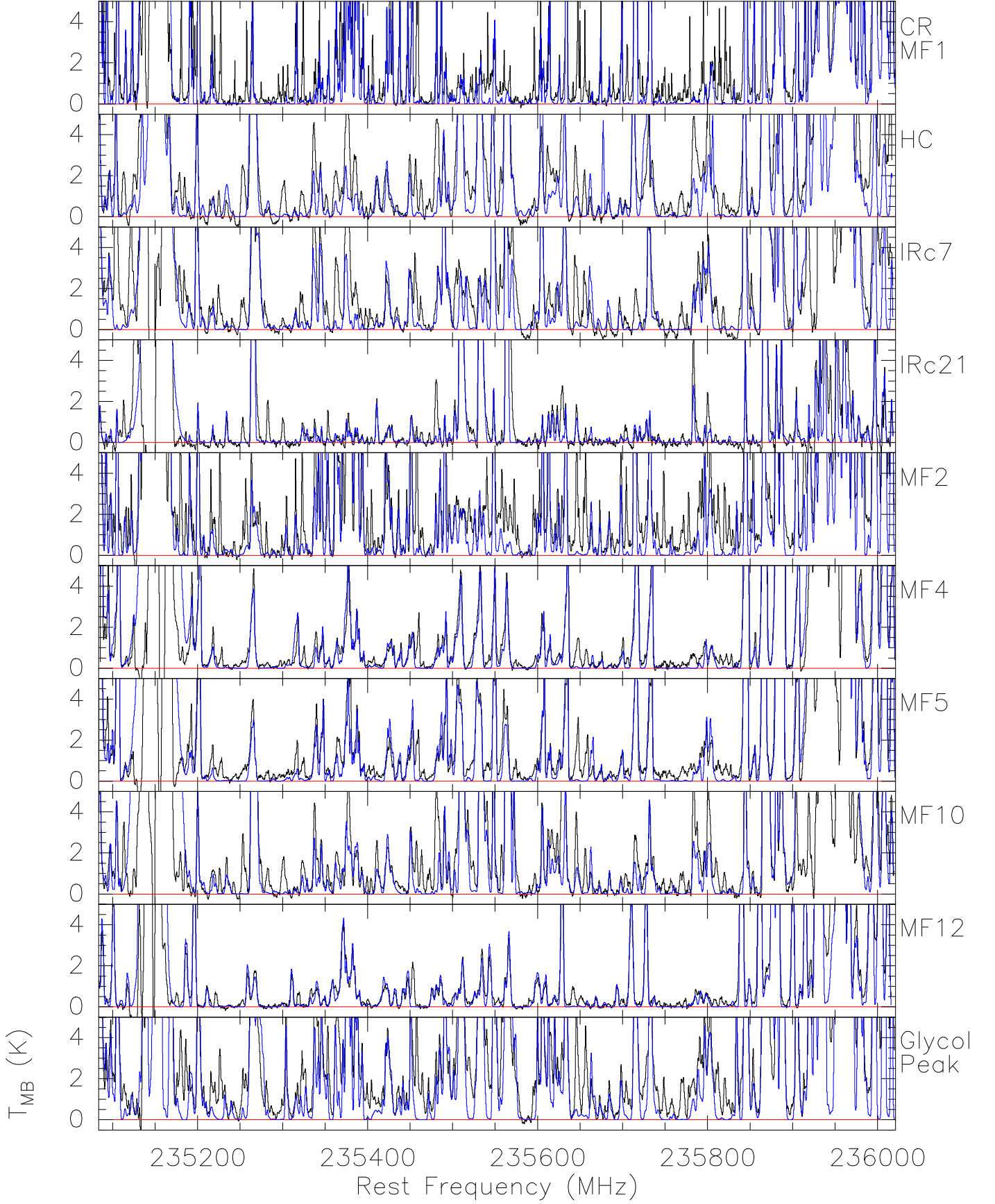


Fig. A.4k. Spectra from the band11 setup for all ten sources with a fixed maximum temperature scale of 5 K to highlight the weaker lines. The red line indicates the 0 K (continuum-removed) level.

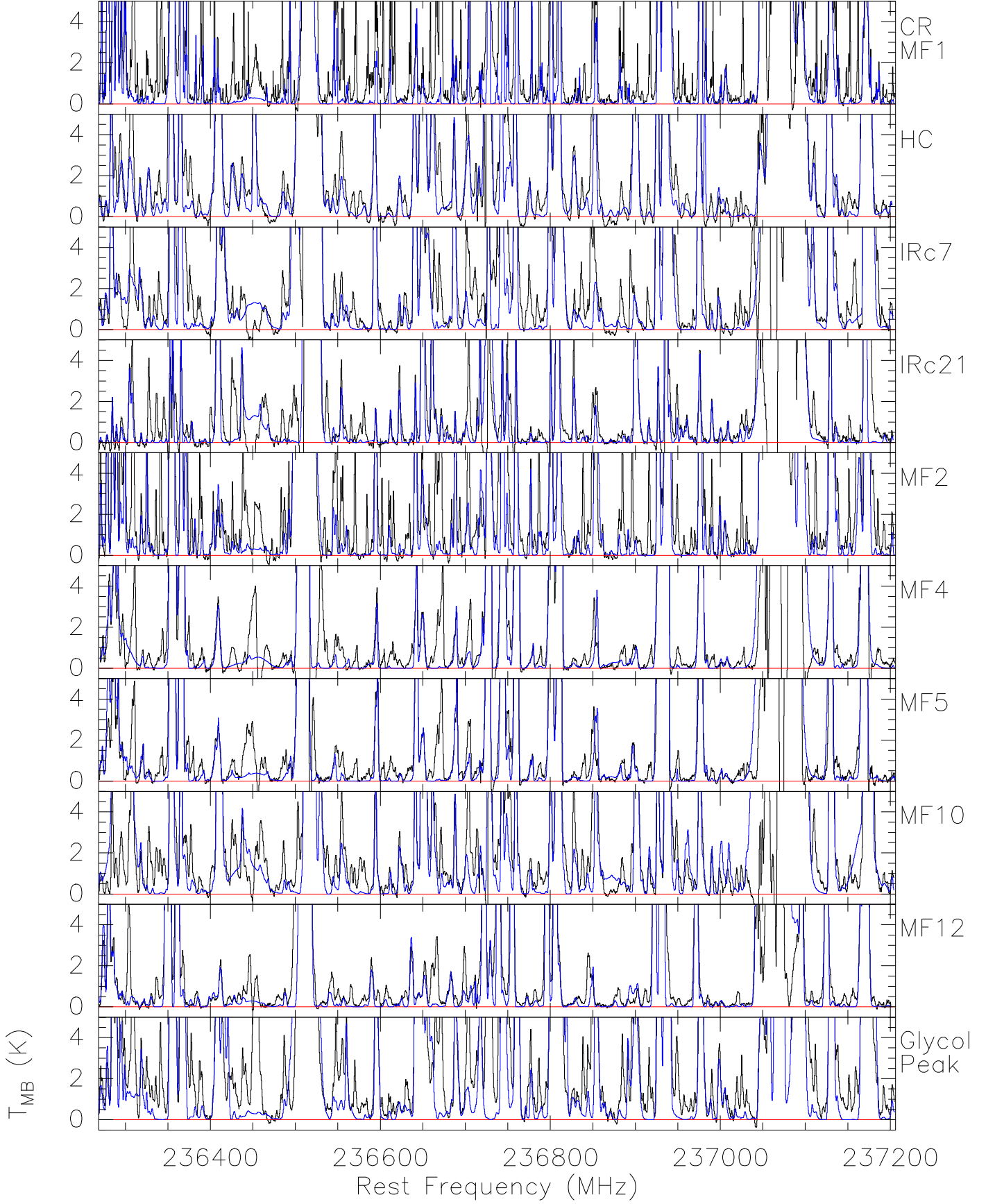


Fig. A.4I. Spectra from the band 12 setup for all ten sources with the summation of fits to individual species in blue and with a fixed maximum temperature scale of 5 K to highlight the weaker lines. The red line indicates the 0 K (continuum-removed) level.

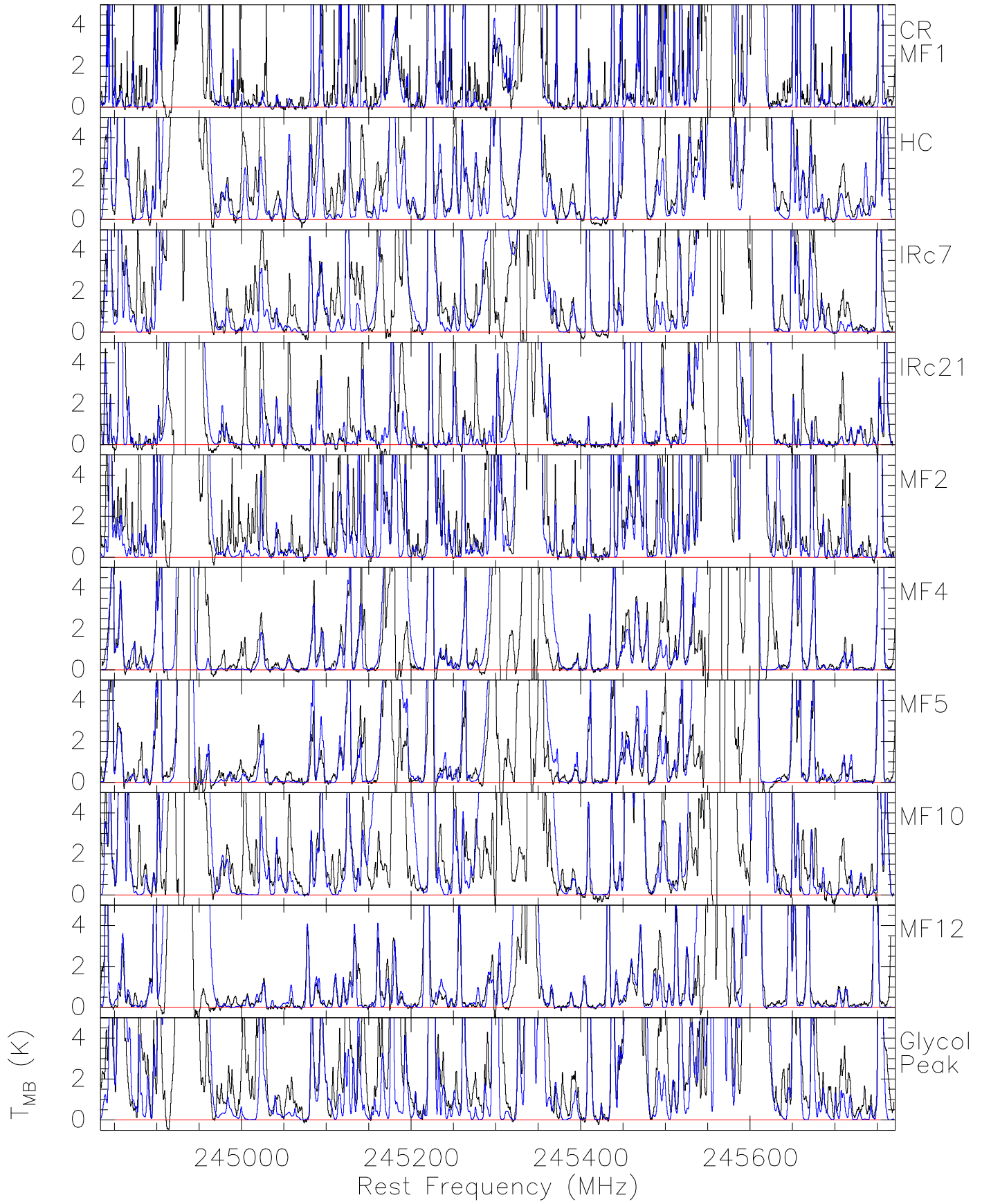


Fig. A.4m. Spectra from the band 13 setup for all ten sources with the summation of fits to individual species in blue and with a fixed maximum temperature scale of 5 K to highlight the weaker lines. The red line indicates the 0 K (continuum-removed) level.

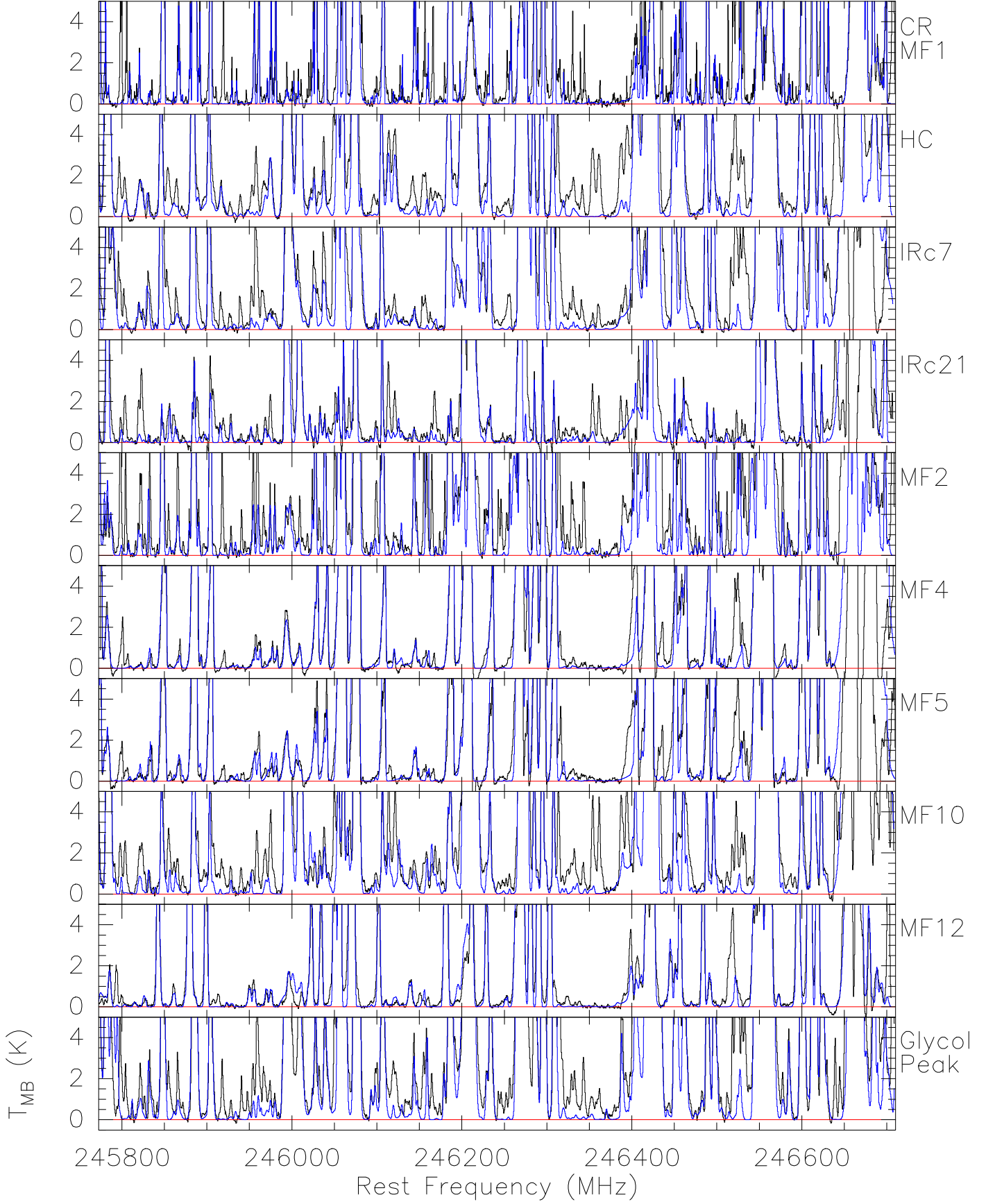


Fig. A.4n. Spectra from the band 14 setup for all ten sources with the summation of fits to individual species in blue and with a fixed maximum temperature scale of 5 K to highlight the weaker lines. The red line indicates the 0 K (continuum-removed) level.

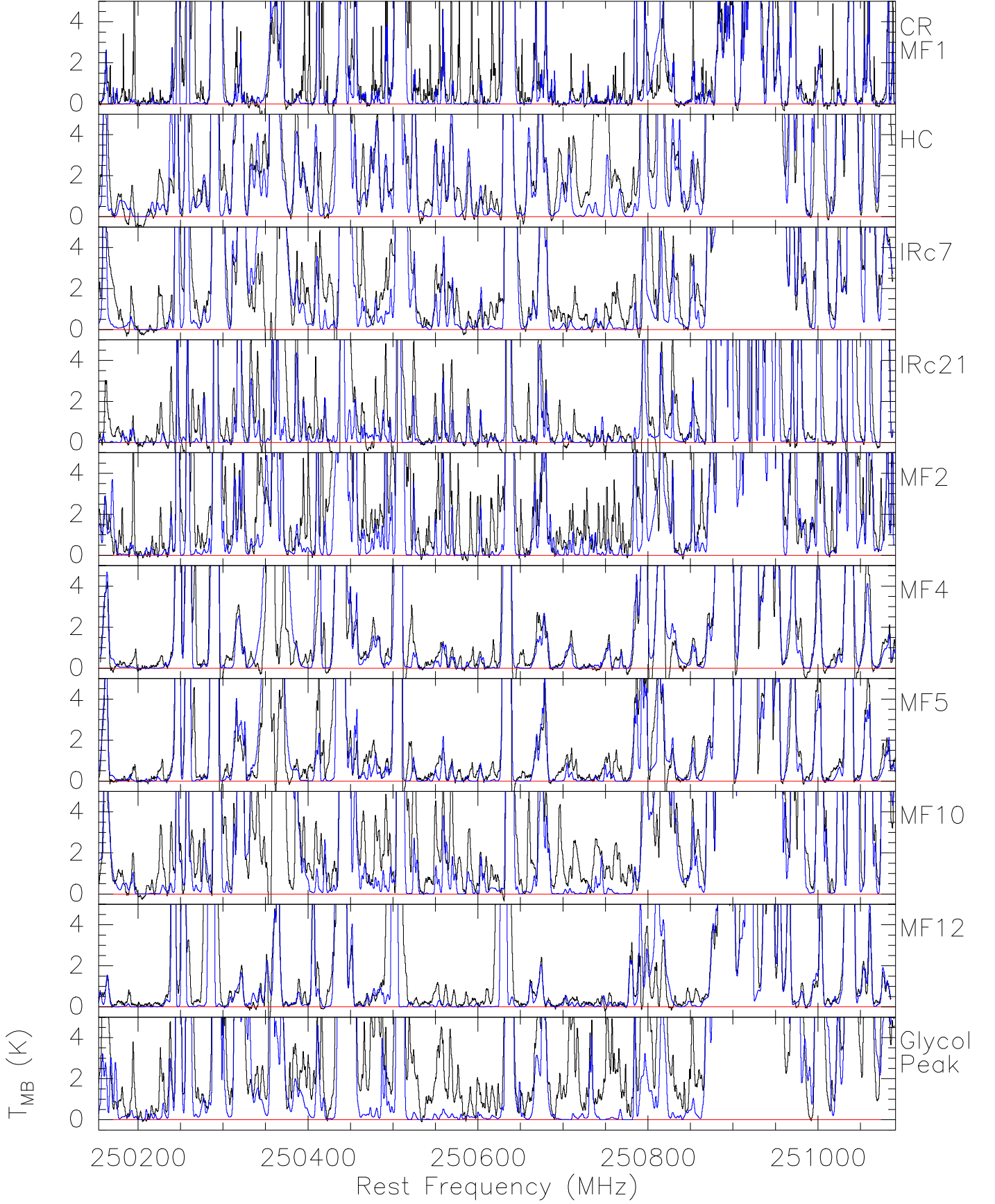


Fig. A.40. Spectra from the band 15 setup for all ten sources with the summation of fits to individual species in blue and with a fixed maximum temperature scale of 5 K to highlight the weaker lines. The red line indicates the 0 K (continuum-removed) level.

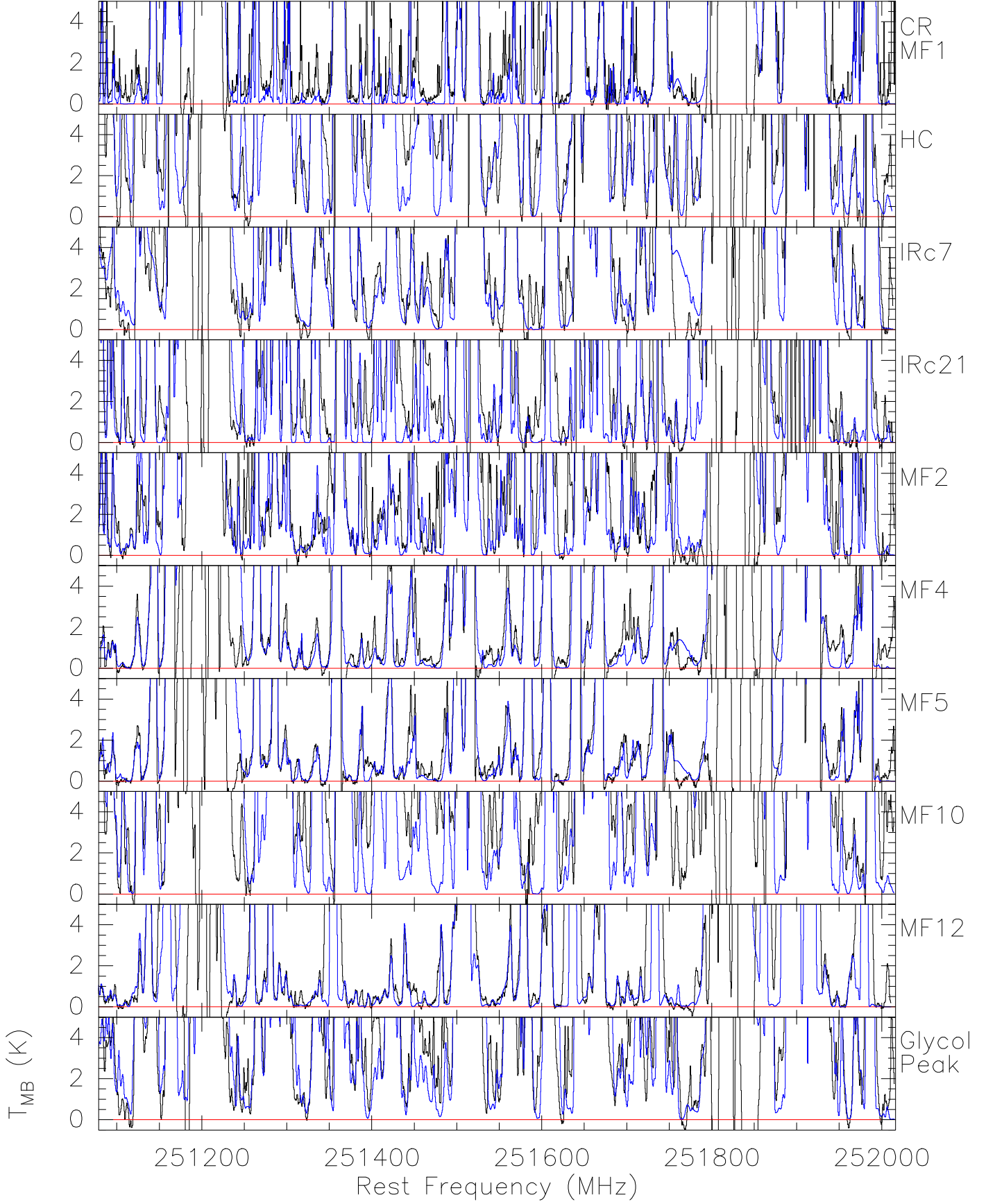


Fig. A.4p. Spectra from the band 16 setup for all ten sources with the summation of fits to individual species in blue and with a fixed maximum temperature scale of 5 K to highlight the weaker lines. The red line indicates the 0 K (continuum-removed) level.

Appendix B: List of species included in this study

Table B.1. Molecules studied in this paper, grouped by number of atoms^a

2	3	4	5	6	7	8	9
detected							
CO	DCN	H ₂ CO	t-HCOOH	CH ₃ CN	C ₂ H ₃ CN $\nu=0$	CH ₂ CHCHO	C ₂ H ₅ CN $\nu=0$
¹³ CO	H ₂ S	H ₂ ¹³ CO	H ₂ CCO	CH ₃ ¹³ CN	C ₂ H ₃ CN $\nu_{11}=1$	CH₃COOH	C ₂ H ₅ CN $\nu_{13}=1/\nu_{21}=1$
C ¹⁸ O	H ₂ ³³ S	H ₂ CS	H ₂ ¹³ CCO	CH ₃ OH $\nu_t=0$	C ₂ H ₃ CN $\nu_{15}=1$	CH ₃ OCHO	C ₂ H ₅ CN $\nu_{20}=1$
CS	OCS $\nu=0$	D ₂ CO	H ₂ C ¹³ CO	CH ₃ OH $\nu_t=1$	¹³ CH ₂ CHCN	CH ₃ O ¹³ CHO	C ₂ H ₅ CN $\nu_{12}=1$
¹³ CS	OCS $\nu_2=1$	HNCO	H ₂ CNH	¹³ CH ₃ OH $\nu_t=0$	CH ₂ ¹³ CHCN		¹³ CH ₃ CH ₂ CN
NO	¹⁸ OCS	NH ₂ D	HC ₃ N $\nu=0$	¹³ CH ₃ OH $\nu_t=1$	C ₂ H ₃ ¹³ CN		CH ₃ ¹³ CH ₂ CN
SO	O ¹³ CS		HC ₃ N $\nu_7=1$	CH ₃ ¹⁸ OH	CH ₃ CHO		C ₂ H ₅ ¹³ CN
S ¹⁷ O	SO ₂		HC ₃ N $\nu_7=2$	CH ₃ DOH	CH ₃ NCO $\nu_b=0$		C ₂ H ₅ C ¹⁵ N
S ¹⁸ O	³⁴ SO ₂		HC ₃ N $\nu_6=1$	NH ₂ CHO	c-C ₂ H ₄ O		C ₂ H ₅ OH
³³ SO	SO ¹⁸ O		HC₃N $\nu_6=2$		CH ₃ OOH		CH ₃ OCH ₃
³⁴ SO	H ₂ O $\nu_2=1$		HC₃N $\nu_6=\nu_7=1$				
SiO $\nu=0$			HC₃N $\nu_5=1/\nu_7=3$				
SiO $\nu=1$			HC₃N $\nu_7=4/\nu_5=\nu_7=1$				
SiS			H ¹³ CCCN $\nu=0$				
Si ³³ S			HC ¹³ CCN $\nu=0$				
Si ³⁴ S			HCC ¹³ CN $\nu=0$				
			H¹³CCCN $\nu_7=1$				
			HC¹³CCN $\nu_7=1$				
			HCC¹³CN $\nu_7=1$				
			H¹³CCCN $\nu_7=2$				
			HC¹³CCN $\nu_7=2$				
			HCC¹³CN $\nu_7=2$				
tentatively detected							
Si ¹⁷ O		H¹³CNH⁺	HC¹³CCN $\nu_6=1$ HCC¹³CN $\nu_6=1$ H¹³C¹³CCN $\nu=0$ H¹³CC¹³CN $\nu=0$ HC¹³C¹³CN $\nu=0$ NH₂CN	CHCCHO	CH₃NH₂	CH₂(OH)CHO	
not detected or totally blended							
O ¹⁸ O	CCD	c-C ₃ H	c-C ₃ H ₂	HC ₃ NH ⁺	C ₂ H ₃ C ¹⁵ N	NH ₂ CH ₂ CN	HC ₇ N
	CCS	l-C ₃ H	l-C ₃ H ₂	c-C ₃ H ₂ O	HC ₅ N		
	H ¹³ CS ⁺	C ₃ S	H ₂ NCO ⁺				
	N ₂ D ⁺	H ₂ CN	HC ₃ N $\nu_7=3$				
	¹⁷ OCS	H ₂ C ¹⁸ O	HC ₃ N $\nu_4=1$				
	³³ SO ₂	HCCN	HC ₃ N $\nu_5=1$				
		HOCN	NCCNH ⁺				
		HONC	NH ₂ CN				
		HOCO ⁺	NH ₂ OH				
		HSCN	HCCNC				
		HNCS	HCOCN				
out of band							
²⁹ SiO $\nu=0$	CCH	HCNO	H ¹³ CCCN $\nu_6=1$	¹³ CH ₃ CN			
³⁰ SiO $\nu=0$	¹³ CCH	HCNH ⁺					
Si ¹⁸ O $\nu=0$	C ¹³ CH						
	OC ³³ S						
	OC ³⁴ S						

Notes. ^(a) New species in Orion are in bold face. Atoms without numbers mean the main isotope.

10	11	12
detected		
CH ₃ COCH ₃	C ₂ H ₅ OCHO	n-C₃H₇CN
C ₂ H ₅ CHO	(CH₂OH)₂	i-C₃H₇CN